

UNIVERSITY OF CALGARY

Passive Catheter Tracking into the Carotid Artery  
using Accelerated Magnetic Resonance Imaging

by

Matthew Ethan MacDonald

A THESIS

SUBMITTED TO THE FACULTY OF GRADUATE STUDIES  
IN PARTIAL FULFILMENT OF THE REQUIREMENTS FOR THE  
DEGREE OF  
MASTER OF SCIENCE IN BIOMEDICAL ENGINEERING

DEPARTMENT OF ELECTRICAL AND COMPUTER ENGINEERING

CALGARY, ALBERTA

AUGUST, 2010

© Matthew Ethan MacDonald 2010

## Abstract

Endovascular therapy is performed clinically with x-ray fluoroscopy imaging. Catheters are visualized moving through the vascular system as they travel to areas or locations of disease. Magnetic resonance (MR) imaging has been explored for catheter tracking, however its use is hindered by lower temporal and spatial resolution. The imaging rates used to passively visualize contrast-enhanced devices are low ( $<1.0$  Hz), and this results in poor visualization, especially near areas of motion (*e.g.*, near the heart).

A real-time MR imaging platform was developed to track catheters and display them after fusion onto roadmap images. MR acquisition acceleration methods were then compared, both *in vitro* and *in vivo*, to assess which method would accelerate device tracking while maintaining good conspicuity of the catheter. Imaging rates are increased to  $>5$  Hz. Finally, demonstration of passive catheter tracking was performed *in vivo*. The catheter was successfully guided from the femoral artery to target vessels, such as the ascending aorta and the brachiocephalic trunk, mimicking the complexity of navigating to the carotid artery in humans.

## Acknowledgements

Many individuals have helped with the work described in this thesis. Dr Richard Frayne provided guidance and supervision during the course of this project. It is inspiring to observe such dedication to scientific understanding. I would like to thank him for all the hours he has put in on trying not only to improve this research project but also myself as a human being. Dr Frayne has created an environment of collaboration among many researchers. I worked very closely with Randall Stafford on the experiments performed in Chapter Three. Randall had a wealth of experience working with the laboratory infrastructure and shared this understanding with me. He also helped throughout the course of this project with editing, commenting on scientific design, and performing experiments. I would like to thank Dr Louis Lauzon and Randall Stafford (again) for teaching me about MR pulse programming, providing the tools required to complete the experiments. I would like to thank Cheryl Meek, Dr Cheryl McCreary and Dr Linda Anderson for their help and insight into the *in vivo* portions of the project, and for the pre-experimental dinners that set the tone for success.

I received financial support from several organizations to support this research; this funding allowed me to continue working and pushing forward with the project. I received support from the Canadian Institute for Health Research and Natural Sciences and Engineering Research Council (NSERC) grants of Dr Frayne. These grants also purchased necessary research supplies and funded other operating expenses. I also received graduate scholarships from NSERC, the Informatics Circle of Research Excellence (iCore), and the Alberta Government (Queen Elizabeth II Scholarship).

I would also like to thank my father William Bruce MacDonald for providing the moments of encouragement throughout my life that have allowed me to get to here. I would like to thank Julia Stanley for putting up with me. : D

## **Dedication**

I would like to dedicate this thesis to my father's father. He passed away midway through my Master's thesis and I was not able to make it home for his funeral. It is rather suiting as he suffered from carotid plaque build up in the later years of his life and this particular project has strong application to treatment of such a disease.

## Table of Contents

Abstract.....	ii
Acknowledgements.....	iii
Dedication.....	v
Table of Contents.....	vi
List of Figures and Illustrations.....	ix
List of Symbols, Abbreviations and Nomenclature.....	xv
Epigraph.....	xvii
CHAPTER ONE: INTRODUCTION.....	1
1.1 Overall Motivation.....	6
1.2 Overall Hypothesis.....	6
1.3 Specific Objectives.....	7
1.4 Project Scope.....	8
1.5 Organization of Thesis.....	9
CHAPTER TWO: BACKGROUND AND LITERATURE REVIEW.....	11
2.1 Clinical Endovascular Therapy.....	11
2.1.1 The Circulatory System: The Highway of Endovascular Procedures.....	12
2.1.2 Diseases Targeted by Endovascular Therapy.....	18
2.2 X-ray Imaging.....	22
2.2.1 X-ray Physics.....	22
2.2.2 Intervention X-ray Imaging Technologies.....	26
2.2.3 Safety of X-ray Imaging in Endovascular Therapy.....	28
2.3 Magnetic Resonance Imaging.....	30
2.3.1 MR Physics.....	30
2.3.2 MR Image Acquisition.....	34
2.3.3 MR Image Reconstruction.....	36
2.3.4 Image Artefacts and Distortion.....	39
2.4 MR-Guided Catheter Tracking.....	42
2.4.1 Active Tracking.....	43
2.4.2 Passive Tracking.....	49
2.4.3 Clinical Applications.....	54
2.5 Acceleration Methods for MR Imaging.....	55
2.5.1 Time-Resolved Methods.....	56
2.5.2 Parallel Imaging.....	57
2.5.3 Compressed Sensing.....	61
CHAPTER THREE: A REAL-TIME MR IMAGING SYSTEM.....	64
3.1 Introduction.....	64
3.2 Methods.....	67
3.2.1 Real-Time Imaging - Hardware and Software.....	67
3.2.2 Imaging Pulse Sequence.....	69
3.2.3 Algorithm Prototyping.....	70
3.2.4 Reconstruction Pipeline.....	72
3.2.5 Image Analysis.....	73

3.3 Results.....	73
3.4 Discussion.....	77
<b>CHAPTER FOUR: COMPARISON OF ACCELERATION METHODS FOR</b>	
<b>PASSIVE CATHETER TRACKING.....</b>	
4.1 Introduction.....	79
4.2 Methods .....	82
4.2.1 In Vitro Model.....	82
4.2.2 In Vivo Model .....	82
4.2.3 Imaging.....	83
4.2.4 Assessment of Acceleration Methods .....	85
4.2.5 Simulation of Computational Requirements .....	86
4.3 Results.....	87
4.3.1 Imaging.....	87
4.3.2 Assessment of Acceleration Methods .....	91
4.3.3 Simulation of Computational Requirements .....	93
4.4 Discussion.....	95
<b>CHAPTER FIVE: PASSIVE MR CATHETER TRACKING FROM THE</b>	
<b>FEMORAL TO THE CAROTID ARTERY IN CANINES.....</b>	
5.1 Introduction.....	97
5.2 Methods .....	100
5.2.1 In Vitro Model.....	100
5.2.2 In Vivo Model .....	100
5.2.3 Endovascular Devices .....	101
5.2.4 Magnetic Resonance Catheter Tracking.....	101
5.2.5 Catheter Navigation.....	103
5.2.6 Confirmation of Catheter Placement .....	103
5.3 Results.....	103
5.3.1 In Vitro Imaging .....	103
5.3.2 In Vivo Imaging .....	104
5.4 Discussion.....	107
<b>CHAPTER SIX: SUMMARY .....</b>	
<b>110</b>	
6.1 Conclusions and Discussion .....	110
6.1.1 Specific Objective 1: Real Time MR Imaging.....	111
6.1.2 Specific Objective 2: Fast Imaging methods.....	114
6.1.3 Specific Objective 3: MR Catheter Tracking.....	115
6.2 Suggestions for Future MR-Based Endovascular Investigations .....	117
6.2.1 Scanner Hardware Infrastructure.....	117
6.2.2 Motion Phantoms.....	119
6.2.3 Animal Experiments.....	119
6.2.4 Composite Braided Endovascular Devices .....	120
<b>REFERENCES .....</b>	<b>121</b>

## List of Tables

Table 3.1 Timing results on algorithms used in real-time image reconstruction pipeline. Image matrix size of $256 \times 128$ .....	76
Table 4.1 Scoring of the qualitative factors of each acceleration method. The preferred method based on this assessment is the CS technique with $2\times$ undersampling.....	92
Table 4.2 Catheter enhancement ratio for different regions of the image. Each of the methods show similar background suppression across the images, but CS has the best ratio.....	94

## List of Figures and Illustrations

Figure 2.1: Whole body contrast enhanced angiography. Adapted from (47,48).....	13
Figure 2.2: Non-contrast-enhanced time-of-flight angiographic image of the circle of Willis. At the front of the circle, the middle cerebral arteries connect and at the rear the basilar artery. The anterior artery connects the two hemispheres and the middle cerebral artery branches into the brain.....	15
Figure 2.3: Visualization of collateral flow. These images represent a time-series of coronal x-ray digital subtraction angiography of the head (a technique described in §2.2.2). Iodine contrast agent is injected into the left carotid artery, it passes through the anterior communicating artery into the opposite hemisphere of the brain supplying it with blood because there is reduced flow in the right carotid artery. ....	16
Figure 2.4: Branching vessels of the aortic arch in a canine.(52).....	17
Figure 2.5: Balloon Angioplasty. Catheter is guided into the blocked vessel and the balloon is expanded to open the artery (61).....	20
Figure 2.6: Aneurysm coil deployment. A catheter is guided to the aneurysm. A coil is wound into the aneurysm from the end of the catheter and then the catheter is removed (62). ....	21
Figure 2.7: Schematic diagram of an x-ray tube. In conventional x-ray tubes, electrons are passed through a vacuum from the cathode to the anode where there is a target. This excitation causes the generation of x-rays that pass out of the tube towards an object that is being imaged (in this case a hand). X-rays that pass through the hand are absorbed by the plate.(64).....	23
Figure 2.8: Compton scattering. Compton scatter occurs when an x-ray photon interacts with an electron in the outer orbital and changes direction.(64) .....	24
Figure 2.9: The photoelectric effect occurs when an x-ray photon collides with a lower orbital electron, ejecting it. A cascade of electrons drop in energy emitting lower energy photons. Photoelectric effect results in x-ray beam attenuation.(64)..	25
Figure 2.10: Fluoroscopy suite. This suite has the typical equipment for endovascular procedures including: a bed for the patient to lay on, an x-ray fluoroscopy C-arm that can rotate around the bed, and screens/monitors for displaying images to the interventional radiologist. Advanced systems have two complete C-arm systems and are capable of acquiring two, typically orthogonal, images. Photograph taken from the University of California, San Diego Campus Medical Centre.....	27
Figure 2.11: Alignment of hydrogen-1 nuclei in the presence of a strong magnetic field. At equilibrium-state slightly more electrons align with the applied magnetic field.(78).....	31

Figure 2.12: Classical model of the spin of a hydrogen-1 nuclei in an externally applied magnetic field ( $\mathbf{B}_0$ ). The magnetic moment ( $\boldsymbol{\mu}$ ) precesses about the applied field at the Larmor frequency ( $\boldsymbol{\omega}_0$ ). The speed of precession is linearly related to the applied magnetic field via the gyromagnetic constant,  $\gamma$ :  $\boldsymbol{\omega}_0 = \gamma \mathbf{B}_0$ . For hydrogen-1,  $\gamma = 42.57 \text{ MHz T}^{-1}$ . Figure was modified from Ref (79). ..... 31

Figure 2.13: Free induction decay. The red arrow represents the net magnetization. The spiral path represents the free induction decay of the net magnetization. Image was modified from ref (80). ..... 32

Figure 2.14: Decay of magnetization by  $T_1$  and  $T_2$ .  $T_1$  decay shows decay of the magnetization to the steady state.  $T_2$  decay shows the decay of the signal to an isochromat state. .... 33

Figure 2.15: Signal generated from an FID. The measured signal decays with respect to the  $T_2^*$  decay curve..... 34

Figure 2.16: Timing diagram for k-space positions. The timing diagram (left) represents the radiofrequency (RF) and gradients (G) used to acquire MR data with a spoiled gradient recalled echo sequence (SPGR). The gradient that is on during the RF pulse is called the slice select gradient, and selects the imaging plane orthogonal to the page. A phase encoding amplitude is selected using the phase encode gradient for each successive pulse. Data sampling is performed while the readout gradient is on, this moves the data across k-space in the readout direction. Each pass the phase encode gradient is changed. The red phase encode gradient represents the red trajectory in k-space and the blue phase encode corresponds to the blue trajectory. Sampling continues until the k-space is filled. .... 36

Figure 2.17: Log magnitude images of k-space and magnitude image space. Left) An image of the magnitude of k-space with the majority of the energy in the middle. Right) Application of a 2D FFT to the matrix on the left and taking the magnitude of the image results in a picture of the brain. .... 37

Figure 2.18: Coil sensitivity profiles. Low resolution images of a water phantom from four different individual coils that combined from a four-channel phased array MR imaging coil. .... 38

Figure 2.19: Gradient warping artefact. Image of a grid phantom at 48 cm FOV. Left) no gradient warp correction. Right) with gradient warp correction..... 40

Figure 2.20: Aliasing artefact. In the image above, the anterior portion of the subject's face was selected outside of the local FOV in the phase-encode direction. As a result, this portion of the subject's face appears wrapped around in the image. .... 41

Figure 2.21: Motion artefact. This image was collected over the course of half a heartbeat. During the collection of the image the heart moved and caused a horizontal rippling artefact in the image..... 42

Figure 2.22: Images of post mortem isolated human aorta. The catheter is located towards the middle (signal void) of the images. TR/TE were 1500/17 (left) and 1500/80 ms (right). The voxel size is 0.27 mm by 0.27 mm by 3 mm. ....	44
Figure 2.23: Single loop antenna coil (Left) and cross-section profile (Right). MR signal intensity is high near the device and gradually tapers off within 5 mm in either direction. Figure is modified from (89). ....	44
Figure 2.24: Active catheter tracking in the aortic arch. Still frame images are shown, and were collected at 3 fps using MR imaging. Figure modified from (21).....	46
Figure 2.25: Tracking images using a guidewire to the coronary artery. a-c) coronal images used to guide the catheter into the ascending aorta. d-g) sagittal images to show the catheter going into the coronary artery. f) Contrast agent is injected to verify the position of the catheter tip. This figure was modified from Ref (85).....	47
Figure 2.26: Active two channel guidewire. Top left shows solenoid tip configuration and loop antenna. Bottom left two configurations depict the device in an aortic arch phantom. Image on the right shows the device being guided into the brachiocephalic trunk of a swine. Figure taken from Ref (23). ....	48
Figure 2.27: Chemical processes for creating gadolinium coating. NH <sub>2</sub> chains are attached to polyethylene using plasma reaction. Chelates are then attached to the anime chains. Gadolinium can be released from gadolinium chloride by passing an electric current through it, the gadolinium ions are then readily encapsulated when combined in solution. Figure modified from (91).....	51
Figure 2.28: Catheter visualization using multi-cycle projection dephasing. Left depicts catheter in the vessel of a canine with no dephasing. Right depicts image obtained with optimised dephasing, and the catheter is very conspicuous. Figure modified from (26).....	53
Figure 2.29: Trajectory of the VARK sampling method. The k-space is divided into 4 different regions and grouped according to the frequency location (left). The regions are then sampled as to acquire the centre regions more frequently than the outside edges. Images can then be reconstructed (updated) at twice the initial rate.....	56
Figure 2.30: Turbo spin echo images of the brain as an example of SENSE. Left) aliased (folded) image of a single coil. Middle) SENSE reconstructed image from the folded coil images. Acceleration factor of 2. Right) Fully sampled image, which is comparable to the middle SENSE reconstructed image. ....	57
Figure 2.31: Images collected with 2.5 times undersampling and reconstructed with the PILS method. The left eight images show the aliased images from each of the coils. On the right are the PILS combined images. Image modified from (33).....	59

Figure 2.32: How lines of k-space are solved for with the SMASH (left) and GRAPPA (right) methods. The SMASH method uses the coil image phase encode lines to solve for the missing data line, and with this implementation, a composite k-space can be found. With the GRAPPA implementation, multiple k-spaces are solved for with a larger weighting kernel. Each of these k-spaces is converted to image space and the images are combined via sum of squares. This has shown improvements in SNR over the originally proposed SMASH method. Figure modified from (32). .....	60
Figure 2.33: Geometry factor artefact. Image on the left is fully sampled. Image on the right is overly accelerated, resulting in distortion in the centre of the image. Image modified from (34). .....	60
Figure 2.34: Flow chart depicting the compressed sensing process. For a given signal (a) undersampling of the Fourier domain can be performed either uniformly or randomly (b). The uniformly undersampled signal has coherent aliasing, and the location of the undersampled signal is not apparent (c). With random sampling the aliasing is incoherent and presents as noise (d). Signal is determined with detection points above a threshold (e&f). The interference from these points can then be determined (g) and subtracted from the initial signal to detect other points in the data. Figure adapted from (35). .....	62
Figure 3.1: Top) Schematic layout of real time imaging system. The user prescribes the scan parameters on the console computer, these variables are then sent to the run time scanner hardware. The run time hardware performs the sequence, as raw data is collected from the receiver coil, it is ported through the run time hardware and to the Mac mini computer. Data is saved, and if the display is turned on, images are displayed in the scanner room. Bottom, from left to right) console computer, magnet with display, real time computer. ....	68
Figure 3.2: Flow diagram of image reconstruction from multiple channels. Raw k-space data is acquired from each of the image coils and placed in separate raw k-space buffers. When enough raw data has been collected to reconstruct an image, the FFT is performed on each of the k-space buffers to create several image buffers. The image buffers are combined with a sum of squares operation, and the image is gradient warp corrected and scaled for display. ....	72
Figure 3.3: Vector field to correct for gradient warping effects. Top left) picture of the grid phantom constructed from multicoloured blocks while it is submerged in water. Top right) Image acquired with no gradient warp correction. Bottom Left) vector field that can be used to correct the image. Bottom Right) geometrically correct image of grid phantom. ....	74
Figure 3.4: Images obtained using a standard (left) and modified (right) FGRE technique. In the standard image the SNR was measured to be 145. the measured SNR was 133 for the modified sequence. ....	75

Figure 3.5: Rapidly acquired MR images of a healthy volunteer speaking. The individual is saying the vowel ‘a’ and then swallowing. Arrow indicates the uvula, which produced m

Figure 4.1: Fully sampled image of the catheter overlaid onto an anatomical roadmap. This image accurately represents the position of the catheter and was used as a benchmark to assess the other images. .... 88

Figure 4.2: In vitro comparison of SENSE, SMASH, GRAPPA and CS for imaging a catheter at 2× and 4× acceleration factors. The SENSE, GRAPPA and CS methods perform better than SMASH for both 2× and 4× acceleration. The GRAPPA and CS methods show the catheter at 4x acceleration. GRAPPA has poor specificity (type II errors) at 4x. The signal varies along the catheter shaft in the CS images. .... 89

Figure 4.3: In vivo comparison of SENSE, SMASH, GRAPPA and CS for imaging a catheter at 2× and 4× multiple acceleration factors. All of the methods visualize the catheter well in the descending aorta, which is an area of less motion. Although signal is present in the aortic arch the signal is significantly corrupted. The CS method performs the best at detecting the catheter..... 90

Figure 4.4: The receiver operator characteristic curves of SENSE, SMASH, GRAPPA, and CS for 2×- and 4×-acceleration. Images from Fig 4.1 and Fig 4.2 were used in calculating the curves. The CS method is most desired based on ROC analysis as it produces the fastest frame rate while maintaining detection of the catheter. .... 92

Figure 4.5: Run-time computational requirements of acceleration factors. CS is an iterative approach, and with the conservative approximations used in the calculations here the method still requires an order of magnitude more processing power (left). SMASH and SENSE require less calculations than full sampling because of a reduction in the size/number of FFT calculations required, while the GRAPPA method requires the same number of FFT calculations plus additional coefficient multiplications (right). .... 95

Figure 5.1: Catheter is being guided into the brachiocephalic trunk. Image frames are acquired at 5.2 Hz. .... 104

Figure 5.2: Axial TOF images used for positioning the 2D catheter tracking slice. The yellow line indicates the position of the tracking slice. .... 105

Figure 5.3: 5 F Catheter is being visualized as it is guided into the ascending aorta. .... 106

Figure 5.4: 6 F catheter being guided to the branching vessels of the aortic arch. The left arrow points to the subclavian artery and the right arrow points to the brachiocephalic trunk artery. From the brachiocephalic trunk, the second branching vessel would be the carotid artery in a human. .... 106

Figure 5.5: Confirmation of the catheter placement in the brachiocephalic trunk. Left) Black blood image of the aortic arch. Arrows indicates that the catheter is in the brachiocephalic trunk. Right) Catheter is filled with iodine contrast agent and is advanced well beyond the position of the aortic arch. ....	107
Figure 6.1: Composite braids that are used in the manufacturing of catheters. These devices were made in a research lab and are not yet commercially available. Figure take from ref (123).....	120

## List of Symbols, Abbreviations and Nomenclature

<b>Symbol</b>	<b>Definition</b>
1D	One Dimensional
2D	Two Dimensional
3D	Three Dimensional
$\gamma$	Gyromagnetic Ratio
$\Phi$	Magnetic Flux
$\omega_0$	Larmor Frequency
$\varepsilon$	Induced Voltage
$\mu$	Attenuation Coefficient
ACA	Anterior Communicating Artery
ADC	Analog to Digital Converter
<b>B</b>	Magnetic Field
<b>B<sub>0</sub></b>	Static Magnetic Field
bpm	Beats Per Minute
bSSFP	Balanced Steady State Free Precession
CS	Compressed Sensing
EMA	European Medicines Agency
EP	Electrophysiology
DSA	Digital Subtraction Angiography
DFT	Discrete Fourier Transform
DWT	Discrete Wavelet Transform
F	French (0.33 mm)
FDA	Food and Drug Administration
FFT	Fast Fourier Transform
FGRE	Fast Gradient Recalled Echo
FLASH	Fast Low Angle Shot
FID	Free Induction Decay
FOV	Field of View
fps	Frames Per Second
G	Gradient
G <sub>x</sub>	x-Gradient
G <sub>y</sub>	y-Gradient
G <sub>z</sub>	z-Gradient
GE	General Electric
GRAPPA	Generalized Autocalibrating Partially Parallel Acquisitions
ID	Identity Penalty
irFLASH	Inversion Recovery FLASH
IVUS	Intra Vascular Ultrasound
<b>M</b>	Magnetization
MCA	Middle Cerebral Artery
mcPD	Multi-Cycle Projection Dephasor
MR	Magnetic Resonance
NASCET	North American Carotid Endarterectomy Trial

NMR	Nuclear Magnetic Resonance
PILS	Parallel Imaging with Localized Sensitivities
RF	Radio Frequency
ROC	Receiver Operator Characteristic
SENSE	Sensitivity Encoding
SMASH	Simultaneous Acquisition of Spatial Harmonics
SNR	Signal to Noise Ratio
SPGR	Spoiled Gradient Recalled Echo
T	Tesla (Unit of Magnetic Field)
TE	Echo Time
TR	Repetition Time
TOF	Time of Flight
TV	Total Variation Penalty
US	Ultrasound
VAR-K	Variable Rate K-space
VD-SMASH	Variable Density SMASH
WT	Wavelet Transform Penalty
ZP	Zero Padding

## **Epigraph**

"Ah, I see, you like to filter your own data."

- Henry S Chen, Member, Catheter Club

## Chapter One: INTRODUCTION

Endovascular therapy has been established over the last 15 years as a technique suitable for treatment of many vascular diseases. This class of techniques requires only a small puncture to access the arterial system, typically via an incision at the groin into the femoral artery. For this reason, these procedures are significantly less invasive compared to other, more traditional, surgical interventions.(1,2) Importantly, endovascular procedures have been shown to have similar clinical outcomes.(2,3) The reduced hospitalization time and faster recovery associated with endovascular management are also highly desirable attributes.

Endovascular-based therapies have opened the door for a range of new therapeutic applications. In the heart, electrophysiological (EP) ablation methods are used to kill (or ablate) small sections of tissue from the interior heart wall using a radio frequency (RF) node on the end of an endovascular catheter, in order to treat atrial fibrillation.(4,5) The key innovation making this technique feasible is the use of image guidance to place the catheter into the heart near the suspected area of irregular electrical conduction. The treatment of cerebral aneurysms by packing them with platinum coils, deployed via a catheter, is another new treatment option made possible by endovascular approaches.(1)

Atherosclerosis is a third disease that can be treated using endovascular therapies. Atherosclerotic plaques can form in many regions of the body (*e.g.*, renal arteries, coronary arteries, the aortic arch and the carotid arteries). While the pathology of atherosclerosis is not fully understood, the disease typically presents as a fatty, and later

fibrous, plaque build up that narrows a blood vessel (known as a vascular stenosis). In cases where the vessel is near the skin, such as the carotid artery, direct surgical intervention can be attempted. This procedure is known as carotid endarterectomy and involves exposing the carotid artery and removal of the plaque. When direct access to the diseased vessel is difficult, for example, if the vessel were located intra-cranially, then endovascular-based therapy offers a potentially better treatment option than surgery. Other common sites of vascular stenosis include the aortic arch, where aortic endarterectomy (6) would require open chest surgery, while endovascular intervention would require only a small vessel puncture, typically at a different location determined by patient and surgeon preference.

Many devices have been proposed for different endovascular treatments. Catheters are the most fundamental instrument and they are essentially a length of a small diameter tube. The centre of the tube is known as the lumen and is used to deliver other devices or agents. All endovascular therapies use some form of a catheter. Guidewires, another commonly employed device, are narrow typically metal wires that can be inserted in the catheter lumen to improve navigation. A variety of other devices have been developed. Many forms of snares, balloons, stents, brushes, cerebral protection, and suction devices have been proposed and used to work with specialized catheters for different applications.(7-11) The selection of which device to use differs depending on the type of intervention, availability, cost, reported performance, and interventionalist preference.(11)

All catheter, guidewire and endovascular device manufactures are required to meet very stringent approval requirements from regulatory bodies like Health Canada, the

US Food and Drug Administration (FDA) or the European Medicines Agency (EMA). Although catheters themselves are relatively simple devices (typically constructed from a structural braid, polyethylene impregnation filling, and a hydrophilic coating), the regulatory approval requirements greatly limit manufacturing to those with experience and substantial capital to get products through pre-clinical and clinical testing stages. Once a device has been approved, company profits can be very large with manufacturing costs of less than ten dollars while the final products can sell for hundreds.

Some form of real-time medical imaging is required to guide catheters, guidewires and devices through the vasculature to the site of vascular disease. Once there, imaging is often also used during treatment to monitor therapy and to ensure that the intervention is successful. Most often x-ray fluoroscopic imaging is preferred. Real-time x-ray imaging has both high temporal and spatial resolutions, making it a suitable choice for endovascular therapy. X-ray fluoroscopy scanning is also compatible with typical instruments used in a surgical suite, and metal devices will show up well on x-ray images. Endovascular catheters, guidewires and devices are engineered to have metallic components that include fine embedded braids or metallic markers to enhance visibility in x-ray tracking images.

X-ray imaging does have drawbacks, particularly, a lack of blood vessel-tissue contrast (*i.e.*, blood and the blood vessels are not easily discernable from other surrounding soft tissues). Commonly, iodine-containing x-ray contrast agents are injected through the catheter lumen in order to make the vessels conspicuous. Some patients have reactions to these agents and care must be taken when administering them to patients with impaired renal function.<sup>(12)</sup> X-ray imaging also exposes both the patient and

interventional staff to ionizing radiation, which has been shown to increase the risk of cancer in the longer term. In-room interventional staff wear lead lined aprons and gloves to attenuate radiation, and newer x-ray systems are designed to minimize exposure. Patients are similarly protected from unnecessary radiation exposure. Several research studies assessed radiation exposure and associated skeletal-muscle damage to staff from heavy protective clothing to understand the extent of this risk.(13,14) Findings in these studies call for a reduction in the hours worked by interventional staff and a safer environment.

Other real-time imaging modalities have been investigated for the purpose of device visualization of therapeutic procedures. Ultrasound (US), for example, is frequently used to guide rigid-needle biopsy procedures and, in theory, could also be used to localize catheter and other endovascular devices from outside of the body. The application of US to endovascular therapy is however limited as reflections from multiple tissue interfaces reduce image quality, and contribute to an overall reduction in image quality with depth into the body. Compared to x-ray, US guidance benefits from the absence of ionizing radiation. Complementary technologies that place US sensors directly onto catheters that allow high-resolution images to be collected of the vessel wall (15-17) are now in routine use. When combined with x-ray catheter guidance to position these sensors, this method (known as intravascular ultrasound, IVUS) provides exquisite images of the atherosclerotic plaque and its components.

Magnetic resonance (MR) imaging has most recently been investigated for endovascular guidance applications. There are two main technical approaches used for visualization: either 1) actively, by attaching antenna coils on the devices,(18-24) or 2)

passively, by using specific material properties.(25,26) In addition to endovascular therapy, MR has been shown as an effective imaging modality for other types of interventional applications, particularly guidance of needle biopsies and brachytherapy procedures.(27-30) The advantages of MR include: 1) that it does not expose patients and staff to ionizing radiation, and 2) it has better soft tissue contrast with respect to x-ray images. MR also has the ability to monitor physiological processes, such as the heart wall tissue necrosis in EP ablation procedures or perfusion-diffusion mismatch in the brain during neurovascular applications for stroke treatment.

A series of recent developments in real-time MR imaging have improved both the temporal and spatial resolutions, as well as increasing the signal to noise ratio, thereby further advancing the potential role for MR as a modality for real time interventional applications.(31-36) To date, there have been a limited number of endovascular therapies attempted, mostly in experimental animal models. In general, the technical and clinical efficacy of MR methods have not yet reached an acceptable level of performance to justify procedures in humans. Nonetheless, MR is arguably the most likely modality, if any, to offer an improvement upon x-ray in endovascular therapies resulting from a combination of superior soft tissue contrast, 3D imaging and the ability to monitor therapy.

Endovascular therapy based procedures have allowed for new avenues of disease treatment and have significantly reduced the invasiveness of some previous treatments. Technical development of both MR compatible devices and real-time MR imaging methods holds additional promises of making these procedures even more effective.

## **1.1 Overall Motivation**

This thesis investigates technical aspects of MR-based endovascular therapies and their application in pre-clinical (animal) experiments. Historically, MR imaging has been plagued by imaging artefacts near areas of motion,(37) metal,(38) and interfaces of changing susceptibility (such as air-tissue interfaces).(39) The temporal resolution of MR imaging has also been a concern, as the frame rates of such procedures have been slower than x-ray systems for similar tracking quality.(40-42)

Recent developments in the field of MR imaging show promise in overcoming these challenges.(43) If the sensitivity to motion, metal and susceptibility can be reduced, and temporal resolution is improved then the advantages of using MR for guiding endovascular therapies, described previously, will help to improve the acceptability of MR-based approaches. Additionally, the advantage of using the same imaging suite for pre- and post- interventional assessment, as well as for the procedure is significant and could reduce critical treatment times for acute procedures. These benefits would be enhanced when more conventional, non-endovascular treatments are not effective and an intervention is required.

## **1.2 Overall Hypothesis**

The overall hypothesis of this work is that a catheter can be guided from the femoral artery to the carotid artery in a large animal model using passive MR catheter tracking. Detrimental image artefacts from the heart and lungs can be reduced by applying accelerated imaging techniques to rapidly acquire catheter tracking images.

### 1.3 Specific Objectives

Passive MR-guided endovascular therapy can be a robust technique as demonstrated in pre-clinical experiments. This overall objective builds on and extends previous work in my group (26,44) and can be broken down into three specific objectives:

1. Development of a new real-time imaging platform that is capable of displaying images in the scanner bore. I expect that displaying images to an interventionalist in the bore will allow better manipulation of devices while observing their location. Real-time reconstruction and fusion of both the road map and tracking images on the same platform will improve the navigation. This platform will also be capable of rapid algorithm prototyping so that new reconstruction and fusion algorithms can be implemented in minimal time.
2. Assessing multiple image acceleration methods to find a method that is desirable for passive catheter tracking by overcoming motion in the thoracic cavity. I believe that the image quality acquired in previous experiments at  $< 1$  Hz (frames per second (fps)), (21,26) can now be acquired at  $> 10$  Hz. However, it is expected that an acquisition of  $> 5$  Hz should be sufficient for tracking. The method that is most desirable will be ported to the real-time platform. It is however likely that, for some proposed approaches, the real-time implementation of such an acquisition will not be feasible due to the computational demand of the image reconstruction.
3. The final specific objective of this project will be to demonstrate tracking to the carotid artery using the products obtained from specific objectives 1 and 2. This

will be done using a canine model in order to simulate key challenges that would be faced in a human subject.

#### **1.4 Project Scope**

To demonstrate proof-of-concept results that support these objectives, the project scope is to sequentially demonstrate each of the outlined tasks. The current scanner console hardware (3 T Signa/VHi, software version 12; General Electric Healthcare, Waukesha, WI) was not designed to support applications for custom image reconstruction in real time. For this reason a stand-alone computer was interfaced with the run-time scanner hardware to allow custom MR image reconstruction in real time. MR pulse sequences, that run on the run-time scanner hardware, were modified so that new acquisitions could be implemented and data could be transferred from the scanner hardware to the real-time platform. This real-time image platform was validated by imaging a series of flow phantoms and healthy human volunteers to assess how the system performed with respect to device tracking and in the presence of motion. Additionally, data were collected and evaluated for multiple catheter tracking reconstruction methods. The different methods were first implemented in an offline setting to evaluate the most appropriate method. Successful tracking was then shown in a set of experimental animals. Approval for all human and animal experiments were obtained from the local Research Ethics Board and Animal Care Committee, respectively.

## 1.5 Organization of Thesis

The thesis is divided into six chapters. Chapter One provides an introduction to the thesis, a brief overview of endovascular therapy, and the motivation and objectives of the project.

Chapter Two summarizes the relevant background material and provides a succinct review of the literature in order to familiarize the reader with terms and methods used in the experiments described in the later chapters. The topics covered in Chapter Two include relevant anatomy, diseases that are targetable by endovascular therapy, the principles of MR imaging, and a review of previous MR catheter tracking efforts.

Chapter Three deals with the development of the real-time imaging platform, and how algorithms can be prototyped for real-time application. It completes the first specific objective (§1.2). This chapter is modified from the combination of two conference abstracts presented at 1) the 55<sup>th</sup> Canadian Organization of Medical Physicists (COMP) Scientific Meeting in Victoria, Canada and 2) from the 11<sup>th</sup> International Society of Magnetic Resonance in Medicine (ISMRM) Scientific Meeting in Stockholm, Sweden.(45,46)

Chapter Four presents a comparison of image acceleration methods suitable for passive MR catheter guiding. This chapter contains both *in vitro* (phantom) and *in vivo* (canine model) data for several image acceleration methods and specifically tackles the second specific objective (§1.2). This chapter will be submitted as a manuscript for publication to the *Journal of Magnetic Resonance Imaging*.

Chapter Five contains the final experiments of the thesis, and addresses the third specific objective. It examines the potential for guidance of a catheter from the femoral

artery into the carotid artery of a canine using passive MR catheter tracking. This chapter will be submitted as a manuscript for publication to *Magnetic Resonance in Medicine*.

Chapter Six summarizes the thesis and discusses the key findings and limitations of the experiments. This chapter suggests future work and directions to build upon these efforts.

## **Chapter Two: BACKGROUND AND LITERATURE REVIEW**

This chapter discusses some of the fundamental principles that will be built upon in later chapters. It reviews clinical endovascular therapy and the anatomical pathways used in later experiments. Also included in this chapter is a review of the principles behind x-ray imaging. The focus then shifts to magnetic resonance (MR) imaging, including principles of MR physics, key previous developments in MR catheter tracking, and acceleration methods applicable to MR imaging. The purpose of this chapter is to explain the relevant terminology, and provide the foundation for the research undertaken.

### **2.1 Clinical Endovascular Therapy**

Endovascular therapy has emerged over the last two decades as a minimally invasive treatment for vascular diseases. Devices, such as catheters and guidewires, are navigated through the vascular system to sites of disease, and once appropriately in place a variety of treatments can be deployed. This type of procedure is considered minimally invasive with respect to more conventional treatments as the entry site for devices are typically in the peripheral vasculature when operating on the heart or brain; traditional procedures would require opening the chest cavity or the cranium. Endovascular therapy has been demonstrated to have comparable patient outcome to the more invasive alternatives and is thus a more desired approach. Clinically, endovascular therapy is performed using medical imaging techniques to visualize devices in the vasculature, and although other modalities have been considered, the current preferred imaging method is x-ray fluoroscopy.

### ***2.1.1 The Circulatory System: The Highway of Endovascular Procedures***

The circulatory system is the pathway for endovascular intervention (Fig 2.1). Certain regions of the body are difficult to reach without resorting to highly invasive surgical methods (*e.g.*, the heart and brain). Endovascular interventions can enter the body at more convenient and less invasive locations. Using techniques such as x-ray imaging, catheters can be tracked to the vascular disease through either the venous or arterial system. In the experiments performed in this thesis, device tracking is performed entirely in the arterial system.

The human heart is a four chambered organ which pumps de-oxygenated blood to the lungs (via the pulmonary circulation) and oxygenated blood into the ascending aorta for distribution to the rest of the body. In a 70 kg male at rest, 5 L/min of blood leaves the heart. A portion of the oxygen-rich blood is pumped through vessels of the heart (*i.e.*, the coronary arteries) but the majority enters the aortic arch. Three vessels branch off of the aortic arch: 1) the brachiocephalic trunk, 2) the left common carotid artery and 3) the left subclavian artery. The aortic arch then curves inferiorly becoming the descending aorta.

The brachiocephalic trunk branches into the right subclavian and the right common carotid artery. The subclavian arteries feed blood to the upper limbs while the common carotid arteries transport blood to the brain. The vertebral arteries, which also supply oxygenated blood to the brain, branch off of the subclavian arteries and run inside the vertebrae of the spine. In a human approximately 20 % of the heart output is sent to the brain *via* the carotid and vertebral arteries.

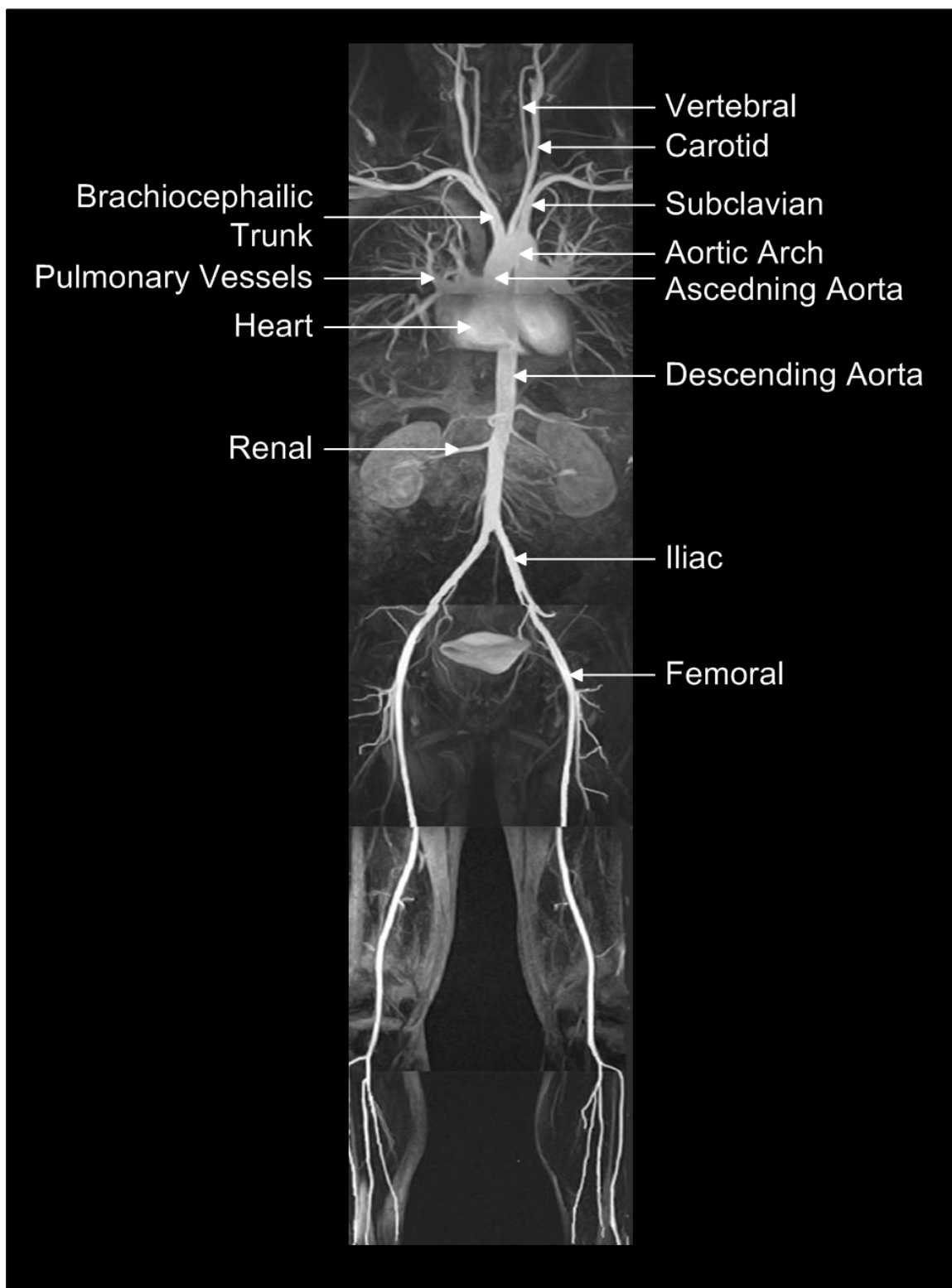
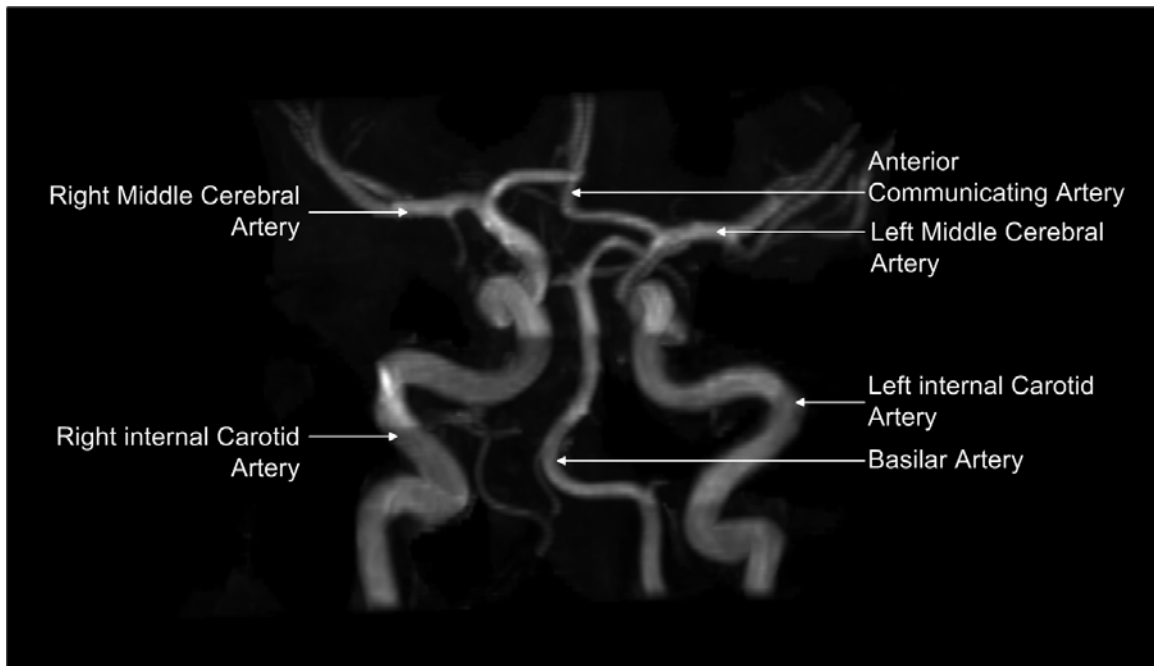


Figure 2.1: Whole body contrast enhanced angiography. Adapted from (47,48).

The descending aorta carries ~ 80% of the heart output inferiorly, supplying the torso and lower limbs. The renal arteries, which provide blood to the kidneys for filtration, branch off the descending aorta at nearly a perpendicular angle. The descending aorta continues further through the abdomen, where it branches into the right and left common iliac arteries. The common iliac arteries branch again, just above the hip, into the internal and external iliac. The internal iliac artery directs blood into the blood vessels in the deeper tissues while the external iliac continues flow down the leg. The external iliac is much shorter than the descending aorta, and branches into the superficial femoral artery and the deep femoral artery. The deep femoral artery feeds blood to the muscle in the upper leg, while the superficial artery propagates blood to the lower leg. The superficial artery is the chosen access site for endovascular experiments in this thesis.

The common carotid arteries supply approximately 70% of the total blood requirements to the brain in healthy individuals.(49) At the level of the jaw, the common carotid arteries branch into internal and external carotid arteries. Near the base of the skull the two vertebral arteries join to form the basilar artery – a unique anatomical structure since it is the only reverse bifurcation in the arterial system. The internal carotid arteries connect to the middle cerebral arteries. The middle cerebral and the basilar arteries then extend toward the centre of the brain and converge at the Circle of Willis (named after the English physician Thomas Willis (50)). The Circle of Willis is a network of vessels that provides a level of redundancy in supplying blood to the brain.

From the Circle of Willis, smaller blood vessels branch out into the brain. One vessel of these branching vessels, the anterior communicating artery, links the left and



*Figure 2.2: Non-contrast-enhanced time-of-flight angiographic image of the circle of Willis. At the front of the circle, the middle cerebral arteries connect and at the rear the basilar artery. The anterior artery connects the two hemispheres and the middle cerebral artery branches into the brain.*

right circulatory territories in the front (anterior) portion of the brain. At the back (posterior) of the Circle of Willis connects the basilar artery and at the front are the interior carotid arteries (Fig 2.2).

The redundancy of the Circle of Willis is a key evolutionary development in that, if the blood supply from one of the major feeding vessels to the brain is disrupted, the remaining vessels can compensate for that disruption. Without this redundancy, any disruption of blood from either the carotid or vertebral arteries would result in catastrophic brain damage, such as severe stroke or death. An example of the effect of this redundancy and the resulting collateral flow is shown in Fig 2.3. It is also important to note that the human intra-cranial vasculature has many variations, and that only a minority of individuals have a complete and redundant vasculature at Circle of Willis.

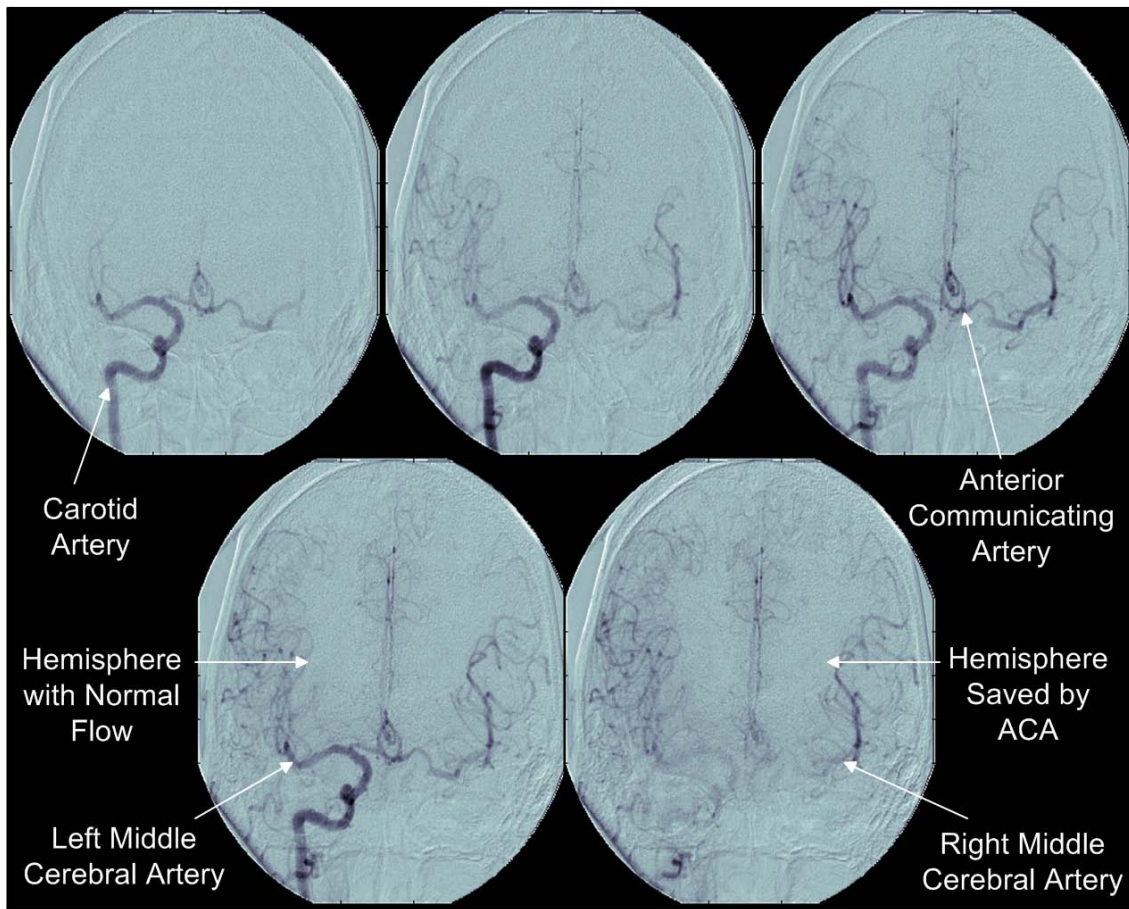


*Figure 2.3: Visualization of collateral flow. These images represent a time-series of coronal x-ray digital subtraction angiography of the head (a technique described in §2.2.2). Iodine contrast agent is injected into the left carotid artery, it passes through the anterior communicating artery into the opposite hemisphere of the brain supplying it with blood because there is reduced flow in the right carotid artery.*

The canine circulatory system is similar to that of the human, although there are some differences. Canines are used for the *in vivo* portion of this thesis as they act as a robust and appropriately scaled model for evaluating endovascular interventions.<sup>(51)</sup> Key anatomical and physiological differences include: the canine heart beats faster than the human heart (100 to 120 beats per minute vs. 60 to 80 beats per minute), and the branching vessels off the aortic arch are different in canines. In canines, there are only 2 branching vessels off of the aortic arch. One branch is the left subclavian artery and,

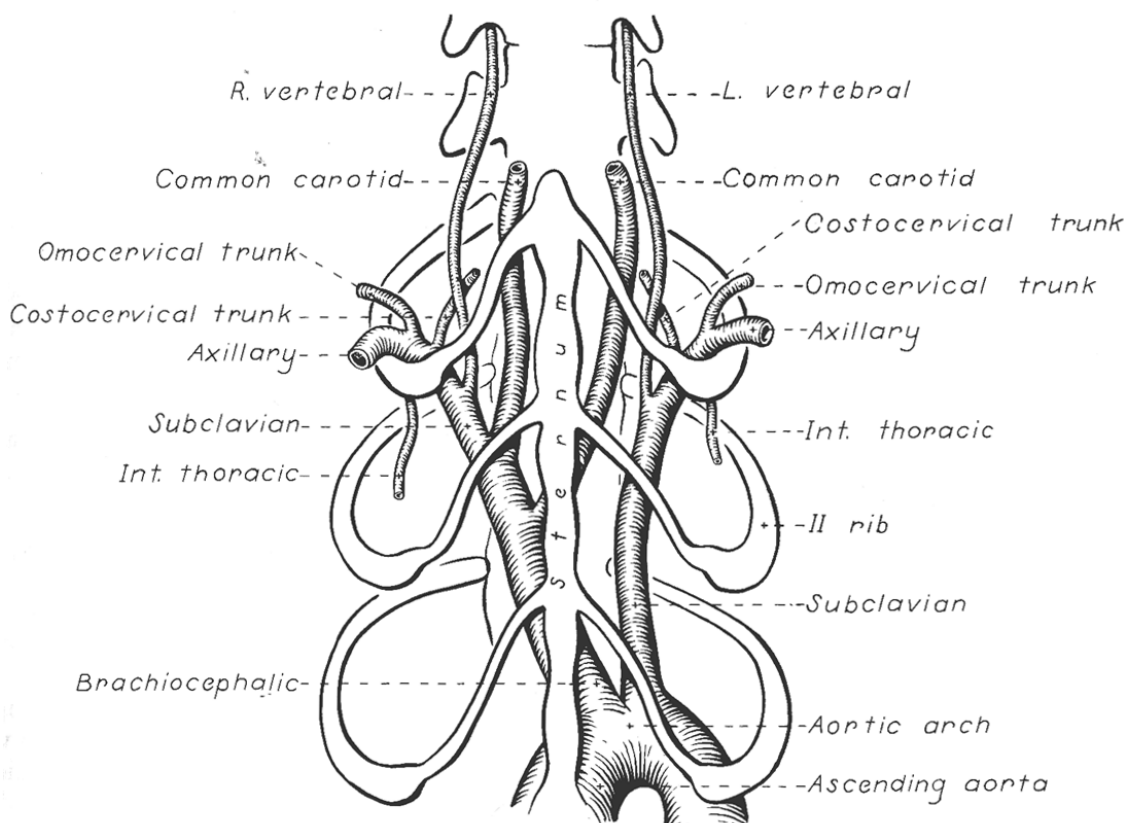


*Figure 2.4: Branching vessels of the aortic arch in a canine.(52)*

the other is the brachiocephalic trunk. In canines, both of the carotid arteries branch off of the brachiocephalic trunk (Fig 2.4)

The canine vasculature is also smaller than the human vasculature; although canine blood vessel diameters are slightly smaller than that of humans, the canine vessels are large enough for demonstration of endovascular guidance.

Major arteries serve as endovascular pathways described in later chapters. In general in humans and specifically in the canines used in these experiments, catheters are introduced into the femoral artery, travel up the external iliac artery into the descending aorta, then to the aortic arch. Then, the catheter is selectively placed into one of the

branching vessels of the aortic arch. Guiding a catheter into the brachiocephalic and carotid arteries in canines with MR imaging is a key achievement that has yet to be demonstrated in literature. It is a necessary step prior to attempting or even contemplating procedures in humans.

### ***2.1.2 Diseases Targeted by Endovascular Therapy***

There are a number of vascular diseases that can be treated with endovascular therapy. Many of these conditions are the result of occlusive vessel disease (*i.e.*, vascular stenosis) and the primary treatment objective is to restore normal blood flow by removing or reducing the blockage. A variety of other conditions, including atrial fibrillation, aneurysms, and thrombus can be treated with endovascular therapy. These methods use a range of specialized approaches and devices for treatment, including balloon angioplasty, vascular stents, radio-frequency ablation probes, suction, coiling, and pharmaceuticals.

Vascular stenosis, by definition, is a reduction of the diameter of a blood vessel, which can lead to a reduction in flow. Stenoses affect many arteries including the aortic arch, carotid arteries, as well as the coronary, iliac, and renal arteries. Stenoses can form at many sites in the vasculature system, but are most prevalent at regions that develop disturbed flow patterns, such as near bifurcations and vessel curvature. Disturbed flow, particularly the resulting regions of low fluid shear rate near the vessel wall,(53) is thought to contribute to thrombus and plaque.(54-56) There are three key types of stenosis: 1) atherosclerosis, where plaques form under the vessel endothelial cell layer narrowing the artery, 2) thrombosis, where a sticky loose plaque forms on the inner vessel walls, and 3) arteriolosclerosis, more particular in small vessels where they become hard and rigid.(57) Severe stenosis can occlude the vessel completely. The presence of a

stenosis can also increase the likelihood of a distal blockage due to emboli (*i.e.*, small particles that are ejected from atherosclerotic lesions into the blood and become caught in smaller calibre vessels).

Interventional treatment such as angioplasty and endarterectomy, or treatment with pharmaceutical agents have been shown to improve outcome in patients with vascular stenosis;(58) though it should be noted that these treatments are not exceptionally effective, rather it is the patient outcome without treatment that is so poor. Endarterectomy is a vascular surgical intervention that became widely used in the 1990's for treatment of carotid artery stenosis.(59,60) The North American Symptomatic Carotid Endarterectomy Trial (NASCET) demonstrated that carotid endarterectomy was effective in patients with confirmed high grade stenosis (70 - 99 % occluded).

Towards the late 1990's, angioplasty, a less invasive endovascular technique was shown to also have positive outcomes for treating a vascular stenosis. (2,60) Angioplasty involves inflating a balloon to the affected area, causing mechanical widening of vessels from within the vessel lumen (Fig 2.5). Stenting can also be combined with balloon angioplasty to hold the vessel open after inflation, and to reduce the risk of stenotic emboli. In addition, devices have been developed for removal of thrombus. Suction-based approaches or snares have been shown to be effective for the removal of thrombus (congealed blood clot).

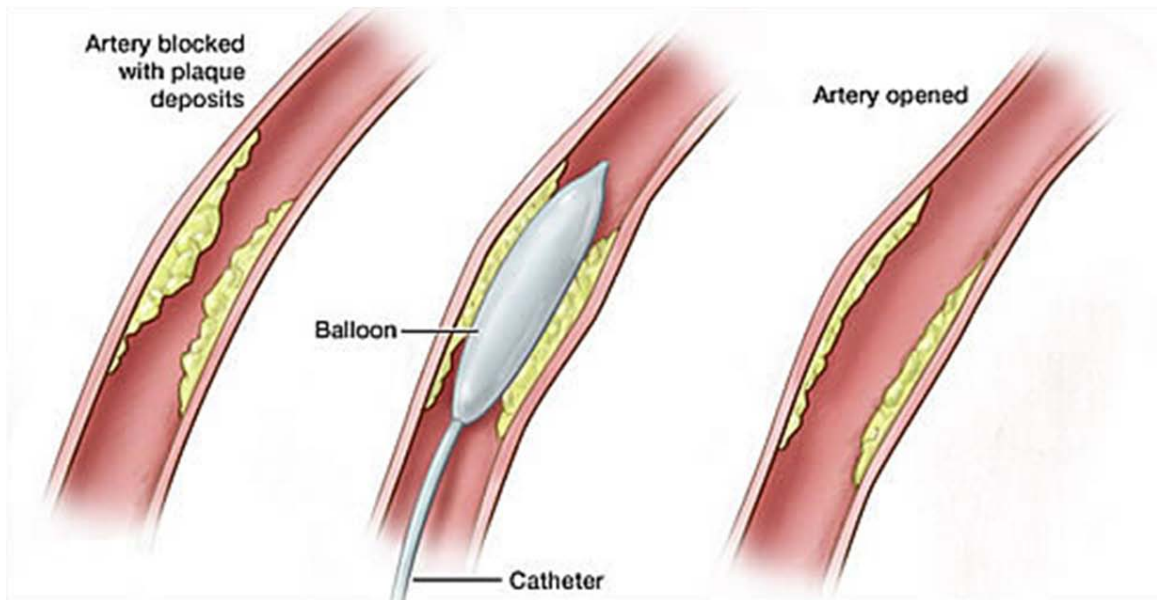


*Figure 2.5: Balloon Angioplasty. Catheter is guided into the blocked vessel and the balloon is expanded to open the artery (61).*

Aneurysms form when the vessel wall weakens and expands forming a blood-filled volume adjacent to the true vessel lumen. This condition is particularly dangerous as aneurysms can rupture and hemorrhage into the surrounding tissue. Aneurysms that form in the aorta, if ruptured, can cause significant internal bleeding and rapid death. A cerebral aneurysm that ruptures and bleeds into brain tissue results in a hemorrhagic stroke, which typically also results in death.

When aneurysms are detected, interventional treatments can be used to reduce the risk of hemorrhage. Stents or covered stents can be used to reduce the risk of aneurysms by reducing the blood pressure on the vessel wall. Endovascular therapy is also effective for treating cerebral aneurysms, where coils of platinum wire are inserted to fill the aneurysm (Fig 2.6).

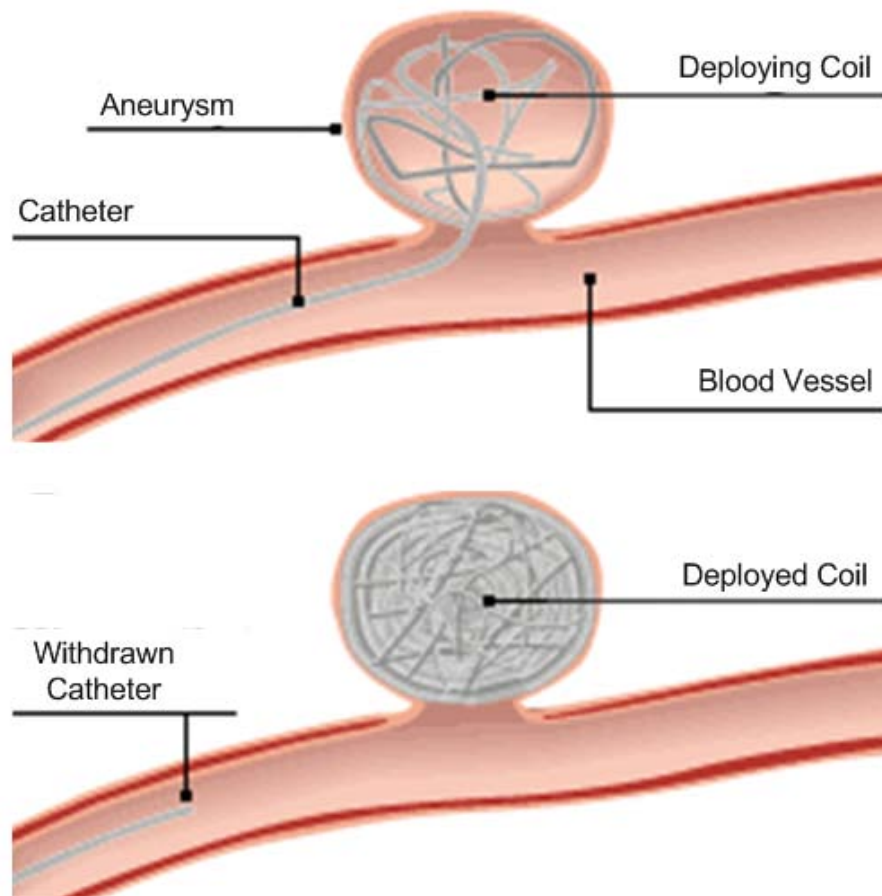


*Figure 2.6: Aneurysm coil deployment. A catheter is guided to the aneurysm. A coil is wound into the aneurysm from the end of the catheter and then the catheter is removed (62).*

Atrial fibrillation is a cardiac disorder characterized by an irregular heart rhythm. The cells of the heart wall conduct an electrical signal that is precisely timed to cause the heart muscle to contract. If some of the heart wall cells do not transmit this electrical pulse correctly, atrial fibrillation (or an irregular rhythm) can result. Atrial fibrillation has been shown to increase the likelihood of stroke. An accepted treatment is to ablate (or kill) the heart cells that are not functioning correctly. By using a radiofrequency transmitter on the end of a catheter to ablate the malfunctioning cells, normal heart rhythm can be restored, thus reducing the risks associated with atrial fibrillation. In a

review of studies between 1990 and 1997 there were 48 clinical studies involving ablation that enrolled a total of 1383 patients.(63) Complications were only observed in 46 patients (3.3%), demonstrating that the procedure is relatively safe.

This section describes some common conditions that are treatable with appropriate types of endovascular therapy. While a range of conditions are described, it is important to note that despite the wide variety of local treatments, all of these endovascular therapy techniques require guiding devices through the circulation system. All of the procedures described in this section would require imaging in order to guide the devices to the site of a stenosis, conduction block or aneurysm. The next sections describe the physical operation of some common techniques such as x-ray and MR imaging.

## **2.2 X-ray Imaging**

X-rays are a form of electromagnetic energy, and can be described as a photon. Using x-rays to form images was first demonstrated in 1895 by Wilhelm Röntgen, and is still used for medical applications worldwide. X-ray imaging is currently the most popular and widely used form of medical imaging.(64)

### **2.2.1 X-ray Physics**

The schematic of a vacuum tube, a typical apparatus for generation of x-ray beams, is shown in Fig 2.7. In a vacuum tube, electrons are passed from a cathode to an anode. The electric potential between the cathode and anode causes the electrons to accelerate. When the electrons collide in the target they lose this kinetic energy and produce *Bremsstrahlung* (German for braking radiation). This target can be made out of several

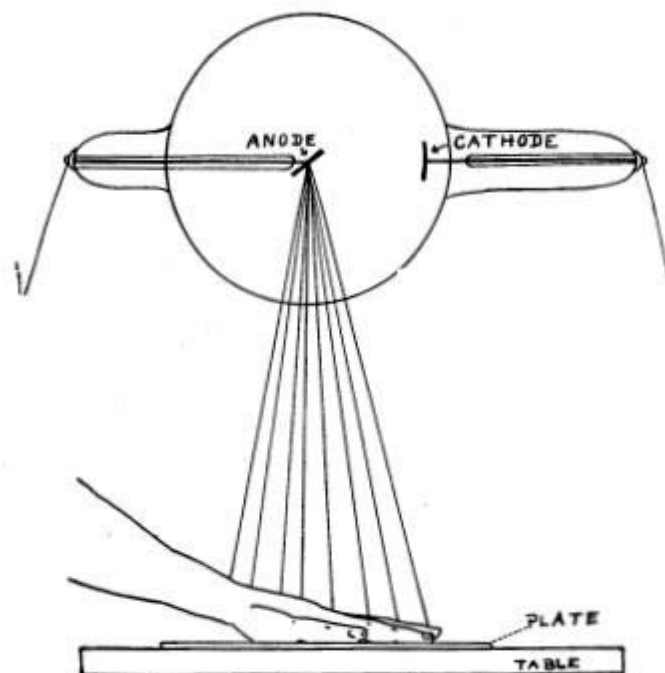


*Figure 2.7: Schematic diagram of an x-ray tube. In conventional x-ray tubes, electrons are passed through a vacuum from the cathode to the anode where there is a target. This excitation causes the generation of x-rays that pass out of the tube towards an object that is being imaged (in this case a hand). X-rays that pass through the hand are absorbed by the plate.(64)*

types of metals with high atomic number and high specific heat, generally tungsten or molybdenum. The x-ray beam that is generated from the target then exits the tube. The x-ray beam can be focused with a collimator (a perforated lead plate). Key parameters in the generation of x-ray photons are the voltage potential (Vp) and the beam current (mA).

Prior to digital computing, a photographic plate could be used to generate images.(Fig 2.7) Modern systems use devices known as scintillators that convert x-rays to visible light, which can be measured with semiconductors. X-rays can also be amplified with the use of an x-ray intensifier, which can improve image quality.

At the energies used in diagnostic imaging (30 kVp to 150 kVp), x-rays can interact with matter in three different ways: 1) Rayleigh scattering, 2) photoelectric

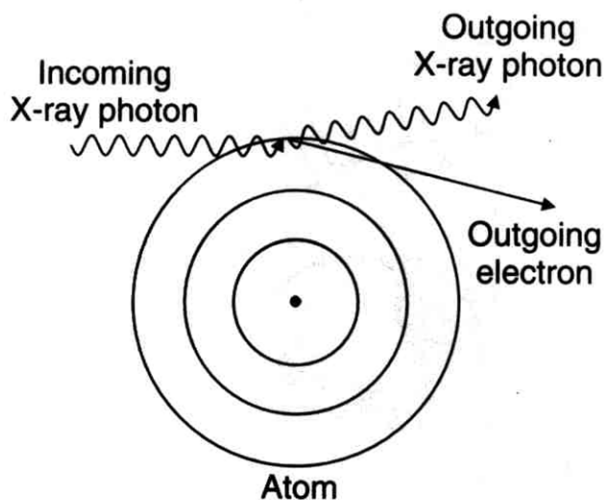


*Figure 2.8: Compton scattering. Compton scatter occurs when an x-ray photon interacts with an electron in the outer orbital and changes direction.(64)*

effect, and 3) Compton scattering. The chance of each type of interaction is a function of energy and material properties. However, 90 kVp x-rays in soft tissue result in mainly Compton scattering interaction (Fig 2.8). Compton scattering occurs when an x-ray collides with an electron in the outer orbital of an atom, the electron is knocked free of the orbital and the x-ray photon changes trajectory. The angle at which the x-ray photon is scattered can be expressed by a probabilistic function and changes for different energy levels and matter. Compton scattering leads to noise in x-ray images.

Rayleigh scattering has the lowest likelihood of the three interactions at the energy levels used in x-ray imaging. This type of interaction does not assist in generating image contrast in x-ray images.

Although the energy associated with the photoelectric effect is not the predominating energy used with x-ray imaging, it is the dominate effect creating image contrast. The energies of incoming photons are high, while the energies of outgoing

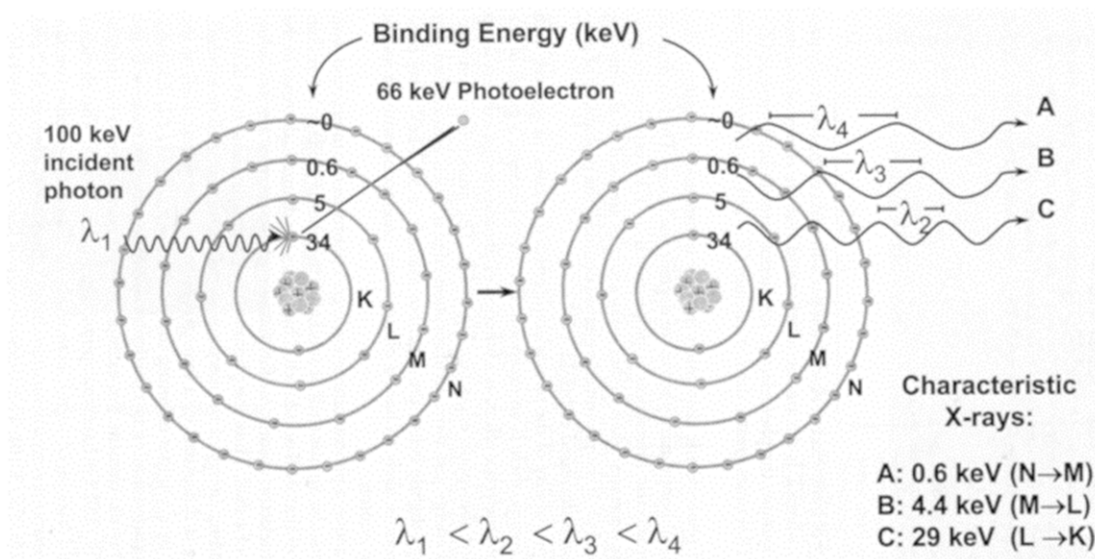


Figure 2.9: The photoelectric effect occurs when an x-ray photon collides with a lower orbital electron, ejecting it. A cascade of electrons drop in energy emitting lower energy photons. Photoelectric effect results in x-ray beam attenuation.(64)

electrons are low (Fig 2.9). As the x-ray beam comes into contact with materials, it is attenuated based on the nucleus size of the material. Materials that have higher attenuation coefficients will show up darker on x-ray images.

In medical imaging, different tissues will attenuate the x-ray beam at different rates. An expression relating the initial beam ( $N_0$ ) to the attenuated beam ( $N$ ) is:

$N = N_0 e^{-\mu \Delta x}$  where  $\mu$  is the linear attenuation coefficient and  $\Delta x$  is the thickness of the material.

X-ray fluoroscopy imaging maps the attenuation coefficients of tissues in a single plane through the body. Image contrast between hard dense tissues and soft tissues is good, but contrast between different types of soft tissues is very poor (e.g., the image contrast between bones and muscle is good, but between blood vessels and the heart is poor).

### ***2.2.2 Intervention X-ray Imaging Technologies***

Modern hospitals and clinics are equipped with x-ray fluoroscopy imaging systems that are capable of acquiring and displaying images in real time (Fig 2.10). Fluoroscopy can be helpful in an assortment of routine clinical tasks, such as confirming that a knee replacement is working correctly, positioning a biopsy needle precisely into a region of suspected tissue pathology, or guiding a catheter through the vascular system. To aid these and other therapeutic applications, x-ray fluoroscopy units have also been incorporated into surgical suites. X-ray fluoroscopy units are capable of image refresh rates of up to 60 Hz (60 frames per second (fps)).(65)

Many surgical devices such as needles, guidewires and catheters are largely composed of metal with high attenuation coefficients making them conspicuous in x-ray images. X-ray fluoroscopy has high spatial resolution and is able to resolve objects as small as 0.33 mm. Digital subtraction angiography (DSA) displays the difference image with and without iodinated contrast agent in the blood and is used to visualise the vasculature. DSA images are particularly important in catheter guiding applications as vessel pathways are otherwise not conspicuous. X-ray imaging does have some limitations. For example, it has historically been used for imaging dense tissues such as bone and does not perform well in softer tissues. The inability of x-ray based imaging to discern between different types of soft tissues is a major limitation. MR imaging has the ability to image soft tissues with superior image contrast compared to x-ray.

Methods such as bi-planar fluoroscopy have been demonstrated. In these experiments, x-ray tubes and detectors are used simultaneously acquiring two separate image feeds.(66) By rotating the x-ray tube and detector around the patient, volumetric



*Figure 2.10: Fluoroscopy suite. This suite has the typical equipment for endovascular procedures including: a bed for the patient to lay on, an x-ray fluoroscopy C-arm that can rotate around the bed, and screens/monitors for displaying images to the interventional radiologist. Advanced systems have two complete C-arm systems and are capable of acquiring two, typically orthogonal, images. Photograph taken from the University of California, San Diego Campus Medical Centre.*

estimates can be made.(67) This method is similar to computed tomography, however it is much slower and not effective for imaging during device navigation. MR imaging has the potential for 3D imaging, which is another advantage to using this modality.

This section has discussed some of the modern x-ray imaging methods used in real-time clinical endovascular procedures. The next section discusses the safety concerns associated with using x-ray imaging during endovascular interventions.

### ***2.2.3 Safety of X-ray Imaging in Endovascular Therapy***

Although x-ray fluoroscopy is a robust technique for imaging during endovascular interventions, there are some safety concerns: the iodinated contrast agents used to generate DSA images can have toxic effects, and ionizing radiation exposure.

Iodine-based contrast agents can have toxic effects when injected into the vasculature, such as damaging the thyroid.(68) Iodine-based agents continue to be used due to their ability to provide diagnostic information about blood flow and vascular roadmaps for device navigation. Iodine contrast agents have a median lethal dose (half of the subjects die) of 4.5 g to 14.0 g per kg of body weight in mice.(69)

X-rays are a form of ionizing radiation, which can cause changes in the molecular structure of self replicating molecules in the body, such as DNA. This can result in mutated biological processes that have been well correlated with the development of cancer.(70) The absorbed dose from being exposed to x-ray radiation can lead to tissue damage, induced cancers, or genetic abnormalities in offspring.(71) During x-ray fluoroscopy procedures both patients and in-room staff are exposed to ionizing radiation.(72) In the case of patients, the outcome from treatment is weighed against the exposure risk; the procedure is only performed if likely benefit outweighs risk. Staff do not benefit from the procedure and thus have a significantly lower limit on absorbed dose. The annual cumulative absorbed dose during interventional fluoroscopy procedures varies depending on a number of factors, including the total imaging time, type of equipment, and the safety precautions taken. Current guidelines limit absorbed dose to <11 Gy for patients and <0.1 Gy/year for interventional staff.(73,74)

In the case of interventional staff, the exposure is minimized by 1) maximizing the distance from the x-ray beam (as exposure falls with distance squared), 2) using fixed and portable shielding when possible, 3) wearing safety clothing, such as lead-lined aprons and gloves, and standing behind lead-containing glasses, and 4) reducing the total time of in-room imaging. In spite of these precautions, in many cases annual radiation dosage for interventional staff exceeds the maximum allowable threshold before the end of each year and thus limits the total number of procedures that can be performed by a clinician.<sup>(75)</sup> Protective clothing can be an occupational hazard in itself, as it is heavy, and can lead to skeletal muscle damage.<sup>(13)</sup> Technical advancements such as pulsed x-ray fluoroscopy have shown promise in reducing the absorbed dose to patients and staff during procedures,<sup>(14)</sup> and several groups have looked at strategies for remotely performing (also known as remote navigating) interventions to reduce the total time in-room staff are being exposed.<sup>(76)</sup> Staff are still required to enter the room and still accumulate a net, though significantly reduced, radiation dose.

X-ray fluoroscopy remains the gold standard for imaging in a variety of procedures, including catheter tracking, despite several well understood and clinically significant drawbacks, such as radiation exposure and poor soft tissue contrast. Its continued use is due to the overwhelming success that x-ray fluoroscopy procedures have had in recent years. These drawbacks, however, suggest that other approaches, particularly using MR imaging, might improve clinical procedures.

## 2.3 Magnetic Resonance Imaging

MR imaging is the topic of much scientific study. It is a newer and, arguably, the most advanced form of medical imaging and can measure anatomical and physiological processes. Due to the scientific and engineering challenges involved with performing interventional applications under MR, it has lagged behind x-ray, however, over the last ten years the modality has shown significant promise for such applications.

### 2.3.1 MR Physics

MR imaging is based on the principles of nuclear magnetic resonance (NMR). MR imaging, generally, only targets the hydrogen-1 nuclei species. Other nuclei (*e.g.*, carbon-13, sodium-23, phosphorous-31) exhibit NMR signal, however, they are generally not imaged in the clinical setting. Hydrogen-1 nuclei are the most abundant atomic nucleus in the human body. The number of hydrogen-1 nuclei in the human body is over ten thousand times the next largest nucleus.(77)

In the presence of a strong magnetic field ( $\mathbf{B}_0$ ) the hydrogen-1 nuclei will precess about the direction of the field. The hydrogen spin is a discrete system, with the precessional direction in either a spin-up or a spin-down state (Fig 2.11).

The spins precess at the Larmour frequency, a rate proportional to the applied magnetic field (64.3 MHz for 1.5 T and 128.6 MHz for 3 T). The classical spin system for a spin-up proton is shown in Fig 2.12.

When there are many nuclei in the same sample volume slightly more will align in the spin-up state. At equilibrium-state the differential in the number of spin-up and spin-down states results in net magnetization ( $\mathbf{M}$ ) in direction of  $\mathbf{B}_0$ .

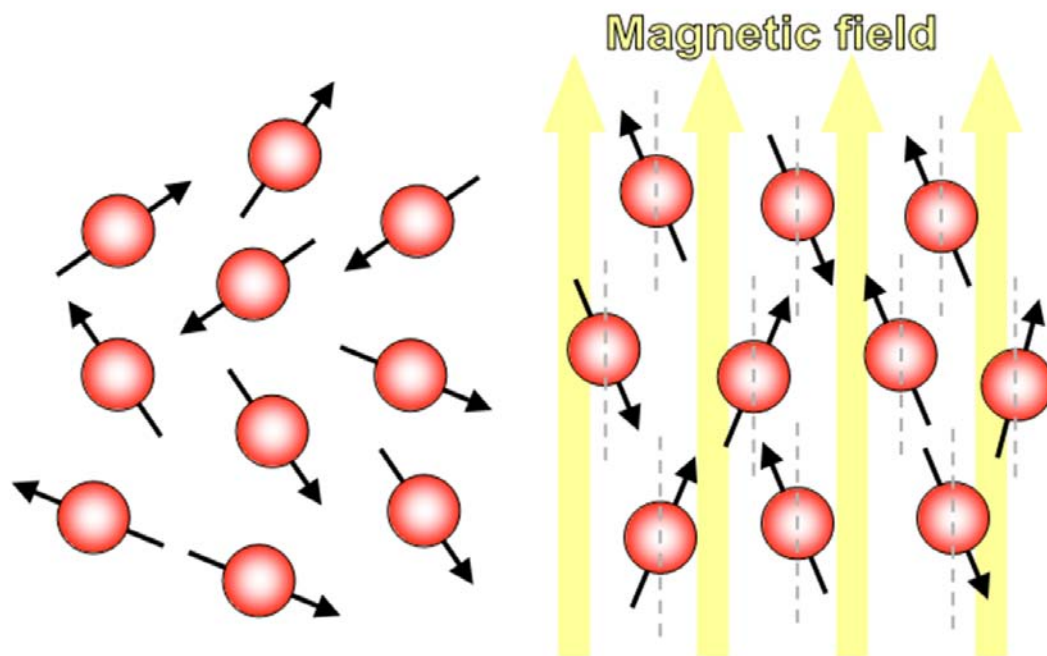


Figure 2.11: Alignment of hydrogen-1 nuclei in the presence of a strong magnetic field. At equilibrium-state slightly more electrons align with the applied magnetic field.(78)

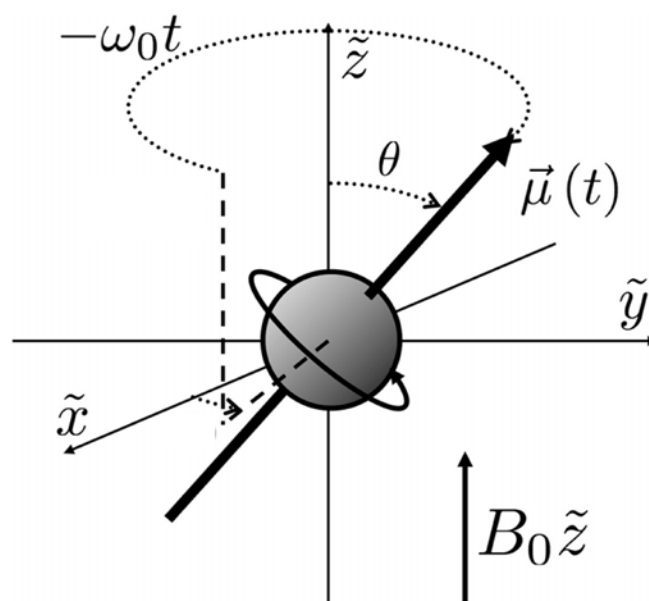
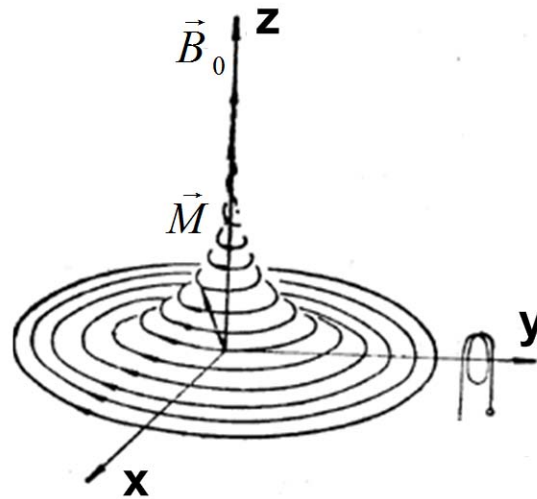


Figure 2.12: Classical model of the spin of a hydrogen-1 nuclei in an externally applied magnetic field ( $\mathbf{B}_0$ ). The magnetic moment ( $\boldsymbol{\mu}$ ) precesses about the applied field at the Larmor frequency ( $\omega_0$ ). The speed of precession is linearly related to the applied magnetic field via the gyromagnetic constant,  $\gamma$ :  $\omega_0 = \gamma \mathbf{B}_0$ . For hydrogen-1,  $\gamma = 42.57 \text{ MHz T}^{-1}$ . Figure was modified from Ref (79).



*Figure 2.13: Free induction decay. The red arrow represents the net magnetization. The spiral path represents the free induction decay of the net magnetization. Image was modified from ref (80).*

Radio-frequency (RF) band energy can be applied to excite the precessing spins. This RF energy, also called an RF pulse, is tuned to the Larmor frequency to match the transition energy between the spin-up and spin-down states. There is no ionizing radiation for MR imaging; only RF energy is applied to generate images. The application of an RF pulse tips the net magnetization into the transverse ( $x - y$  plane). Once RF energy has been applied, the system of spins will release this added energy as it decays back to the equilibrium state; this is known as free induction decay (FID) (Fig 2.13)

The FID is often expressed with two relaxation times, the longitudinal relaxation time,  $T_1$ , and the transverse relaxation time,  $T_2$ .  $T_1$  is the exponential constant characterizing the regrowth of the net magnetization in  $z$  direction.  $T_2$  is the exponential decay constant characterizing the dispersion of aligned spins in the  $x-y$  plane. The phenomenological Bloch equation

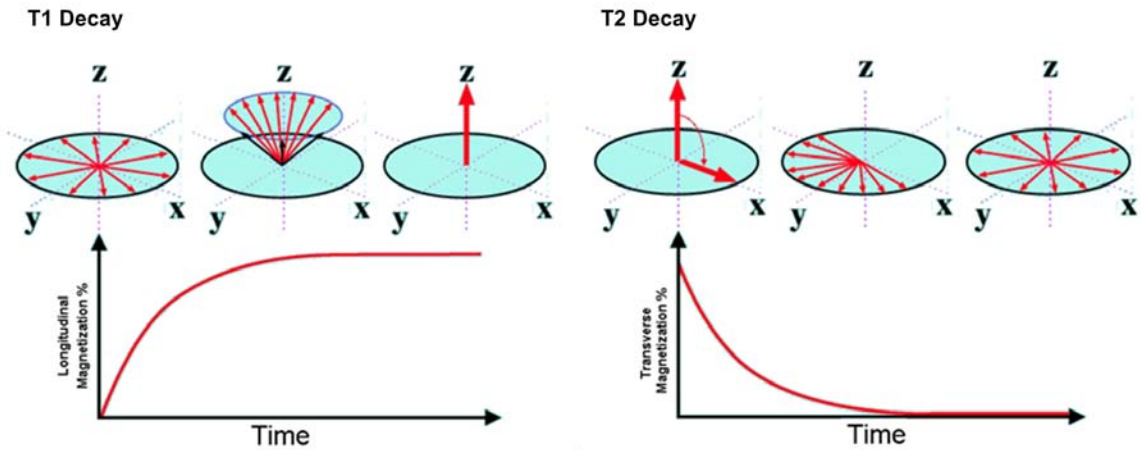


Figure 2.14: Decay of magnetization by  $T_1$  and  $T_2$ .  $T_1$  decay shows decay of the magnetization to the steady state.  $T_2$  decay shows the decay of the signal to an isochromat state.

describes the temporal evolution of the three-dimensional magnetization, and how that evolution is related to  $T_1$  and  $T_2$ ,

$$\frac{d\vec{M}(t)}{dt} = \gamma \vec{M}(t) \times \vec{B}_0(t) - \frac{M_x + M_y}{T_2} - \frac{M_z - M_0}{T_1} \quad [2.1]$$

Solving this differential equation for  $M(t)$  results in the exponential decays of  $T_1$  and  $T_2$  (Fig 2.14). For most tissues in the human body  $T_1 \sim 10 T_2$ . It should be noted that MR contrast agents can be used to shorten  $T_1$  and  $T_2$ .

When the net magnetization is tipped into the transverse plane the flux from the rotating nuclei can be measured by appropriately oriented near-field antennas (also known as MR imaging coils). A time-varying change in the magnetic flux ( $\Phi$ ) through the coil induces a voltage via Faraday's Law,

$$\varepsilon = -\frac{d\Phi}{dt}, \quad [2.2]$$

where the magnetic flux is defined by the surface integral of the dot product of the magnetic field ( $\mathbf{B}$ ) and antenna loop surface,

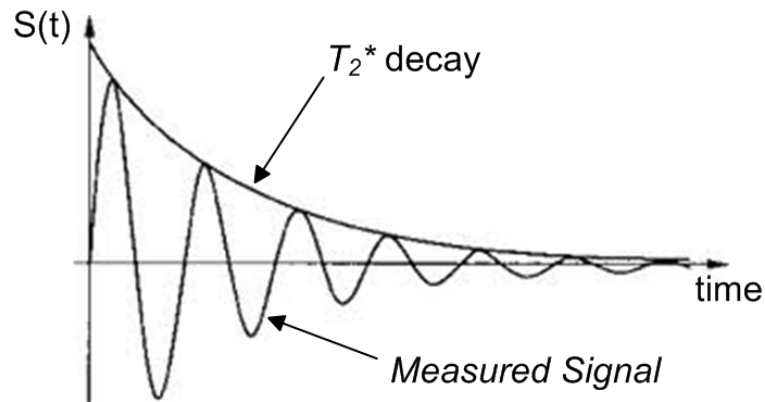


Figure 2.15: Signal generated from an FID. The measured signal decays with respect to the  $T_2^*$  decay curve.

$$\Phi = \int_S \vec{B}(x, y, z, t) \cdot d\vec{A} \quad [2.3]$$

MR imaging uses receiver coils to measure the voltage induced by the magnetization in the image volume. Experimentally, pure observation of  $T_2$  signal decay is difficult to achieve from a single excitation pulse. Often what is observed in the FID is  $T_2^*$ , which is the  $T_2$  decay, but affected by interactions in the sample that cause it to decay faster (e.g.,  $T_2^* < T_2$ ). In many fast imaging applications  $T_2^*$  is the signal contrast mechanism and is observed in the FID of Fig 2.15.

### 2.3.2 MR Image Acquisition

Gradient coils inside MR scanners are used to generate additional magnetic gradients in three orthogonal directions (x,y,z). Application of localized gradients change the z-component of the magnetic field locally and thus spatially change the precessional frequency of hydrogen-1 spins. Gradient fields are essential to MR imaging. The spatial frequencies can be made to vary in three orthogonal directions; this domain is referred to

as  $k$ -space (note that  $k$  is a vector quantity and not bolded). The gradient fields are related to  $k$ -space by the integral,

$$\vec{k}(x, y, z) = \gamma \int \vec{G}(x, y, z) dt \quad [2.4]$$

The  $k$ -space is the domain in which MR image data are acquired and, as will be seen in §2.3.3, represents the Fourier transform of image space.

MR pulse sequence diagrams are timing diagrams that are typically used to visualize behaviour of the RF pulses and 3D gradient fields as separate functions of time. These pulse sequence diagrams are a key aspect to help describe the temporal relationship between gradient fields,  $k$ -space, and RF excitation.

Rectilinear sampling trajectories (known as “spin-warp” imaging) have become the standard in MR imaging applications because of the robustness against hardware imperfections and ease of implementation. There are many specific types of MR pulse sequences; spin echo, balanced steady-state free precession, gradient-recalled echo, *etc.* A sample pulse sequence diagram for a gradient-recalled echo sequence is shown in Fig 2.16. This example represents the acquisition of a single data readout line (*i.e.*, one line of data collected in  $k$ -space). The data is collected while the readout gradient is on. This relation means (via Eq [2.4]) that the positional-encoding into the frequency for each data readout point is changing during the readout. Data readout time can be decreased by increasing the sampling rate and the gradient amplitude. Eq [2.4] indicates that the integral of the gradient represents the  $k$ -space position, so in theory, trajectories could traverse faster through  $k$ -space by increasing the gradient amplitude. However, there are

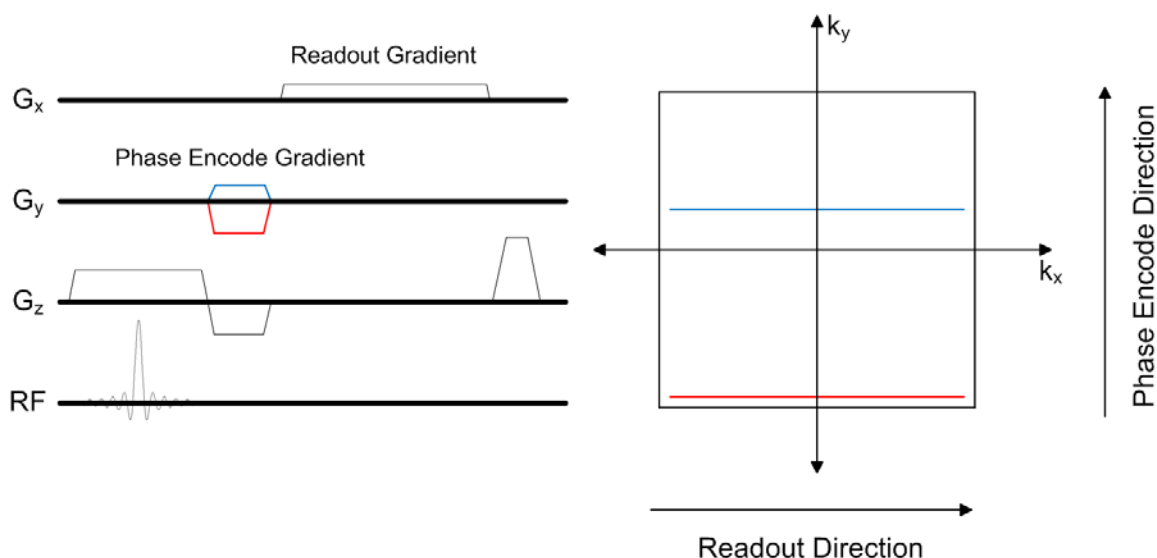


*Figure 2.16: Timing diagram for  $k$ -space positions. The timing diagram (left) represents the radiofrequency (RF) and gradients ( $G$ ) used to acquire MR data with a spoiled gradient recalled echo sequence (SPGR). The gradient that is on during the RF pulse is called the slice select gradient, and selects the imaging plane orthogonal to the page. A phase encoding amplitude is selected using the phase encode gradient for each successive pulse. Data sampling is performed while the readout gradient is on, this moves the data across  $k$ -space in the readout direction. Each pass the phase encode gradient is changed. The red phase encode gradient represents the red trajectory in  $k$ -space and the blue phase encode corresponds to the blue trajectory. Sampling continues until the  $k$ -space is filled.*

restrictions set by the medical device regulatory agencies that limit gradient field amplitudes and slew rates due to peripheral nerve stimulation concerns.

MR pulse sequences can be manipulated to image faster, but often at the price of the signal to noise ratio (SNR), geometric fidelity, contrast, or  $T_1$ ,  $T_2$ ,  $T_2^*$  weightings. The next section discusses how MR images are produced from  $k$ -space data.

### **2.3.3 MR Image Reconstruction**

MR image reconstruction relies on the Fourier transform to convert frequency information from  $k$ -space into an image. A complex discrete Fourier transform (DFT)

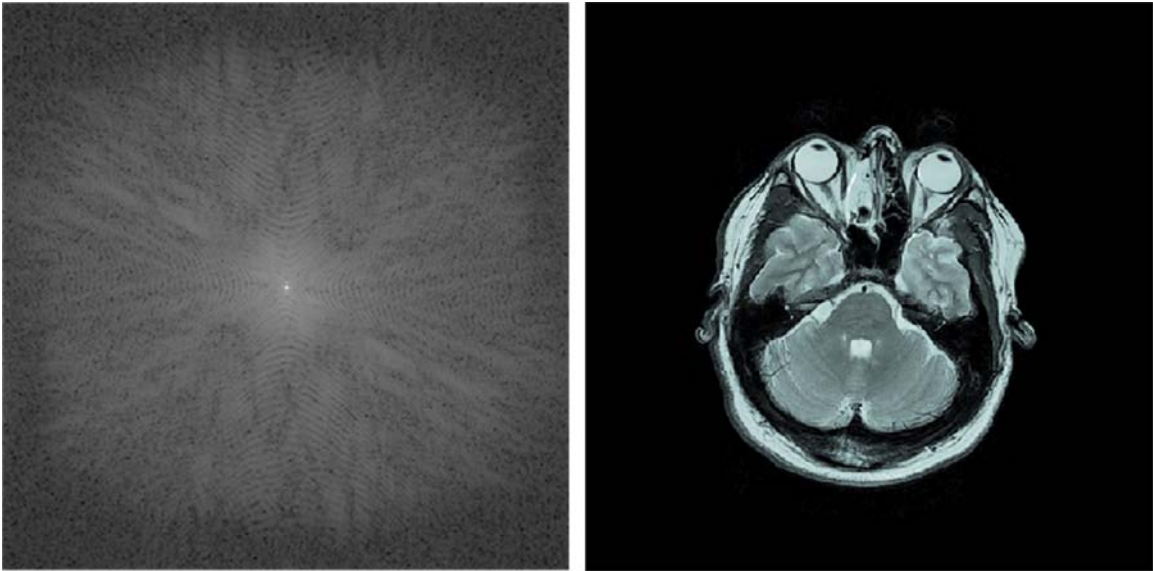


*Figure 2.17: Log magnitude images of  $k$ -space and magnitude image space. Left) An image of the magnitude of  $k$ -space with the majority of the energy in the middle. Right) Application of a 2D FFT to the matrix on the left and taking the magnitude of the image results in a picture of the brain.*

operation is applied to the fully sampled  $k$ -space grid to produce image-domain data.

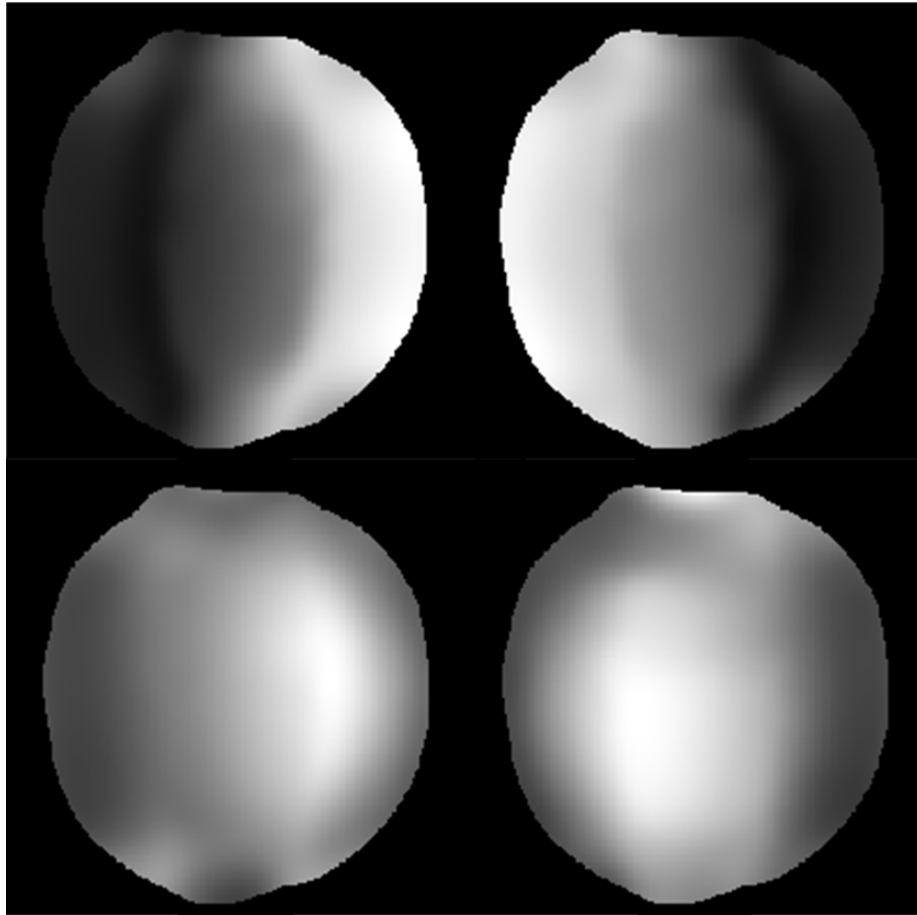
Following the DFT, the image data values are still complex numbers. It has been shown effective to use the magnitude of the complex image data as the gray scale MR

image.(Fig 2.17)

Filtering is an effective way to improve MR image quality. Several multiple dimensional window functions are available for MR imaging applications.(81)

Windowing removes high frequency noise in images, however, it can also remove the high-frequency image details that are desired for some applications. Selection of the window function should be considered carefully and tailored to the specific application.

Zero-padding (ZP) can improve the apparent resolution of images. Fourier interpolation is an effective strategy since MR image data is collected in the Fourier domain. Higher frequencies that were not collected are assumed to be zero in value



*Figure 2.18: Coil sensitivity profiles. Low resolution images of a water phantom from four different individual coils that combined from a four-channel phased array MR imaging coil.*

increasing the image matrix size. It should be noted that improving the image matrix size does not improve the information content in the resulting image.

Modern MR scanning uses multiple antennas placed close to the image volume to increase SNR. With this approach, each of the antennas independently samples the data simultaneously. Multiple  $k$ -space buffers are acquired, each of which can be used to reconstruct an image. These coils are spatially sensitive and the image data is brighter closer to the coil. Thus, the images that are reconstructed from multiple coils are often

combined from the individual coil images using the sum of squares approach. An example of sensitivity maps from a four-channel coil array is shown in Fig 2.18.

The method for creating a single image out of multiple receiver coils with windowing and interpolation has been described. This is the conventional method for reconstructing MR images. Some imaging artefacts that can appear in MR imaging are outlined in the next section.

### ***2.3.4 Image Artefacts and Distortion***

MR, like other medical imaging modalities, can suffer from various artefacts that can reduce or destroy the quality of images. In this section, some typical MR imaging artefacts are described along with methods to compensate for the particular distortions.

Susceptibility artefacts can appear near tissue interfaces where the magnetization changes quickly over a short distance. They present as a signal void. This type of artefact is very dependent on the imaging acquisition type. Fast  $T_2^*$  weighted sequences, such as gradient recalled echo imaging, are generally the most affected by this phenomenon. To avoid these artefacts, one effective strategy is to choose imaging sequences that are not as strongly affected by susceptibility when imaging near these regions. Metal in the imaging plane can also result in signal void due to susceptibility. Ferromagnetic and paramagnetic materials disrupt the local magnetic fields, thus changing the precessional frequency and relaxation properties of the nearby hydrogen-1 protons. For example, metal earrings or other piercings can cause large signal voids in the image. This can also occur with metal surgical instruments and implants as well. Careful patient screening is an effective solution to ensure no metal-based artefacts can occur. This also provides an additional

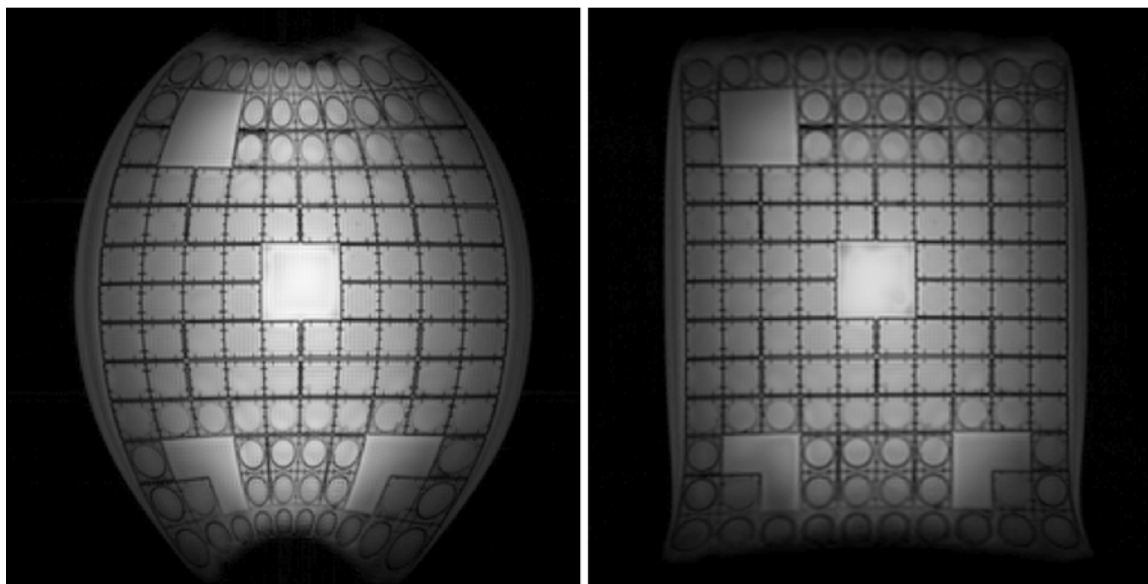


*Figure 2.19: Gradient warping artefact. Image of a grid phantom at 48 cm FOV. Left) no gradient warp correction. Right) with gradient warp correction.*

level of safety for the patient and operator, as metal can be dangerous in or around MR scanners.

Gradient warping artefacts display as a geometric distortion of the image. The phenomenon is produced by gradient non-linearity across the imaging FOV. This type of artefact is generally corrected for with a gradient warp correction algorithm that uses either spherical harmonics or a calibrated vector shift. Most modern scanners have some form of gradient warp correction. An example of gradient warp distortion is shown in Fig 2.19.

Aliasing artefacts can appear in the phase encoding direction which cause objects outside the local FOV to wrap into the image. This type of artefact is caused by failing to meet the Nyquist criterion with a small FOV, and it can easily be corrected for by extending (or more properly choosing) the FOV. An exam with an aliasing artefact is shown in Fig 2.20.

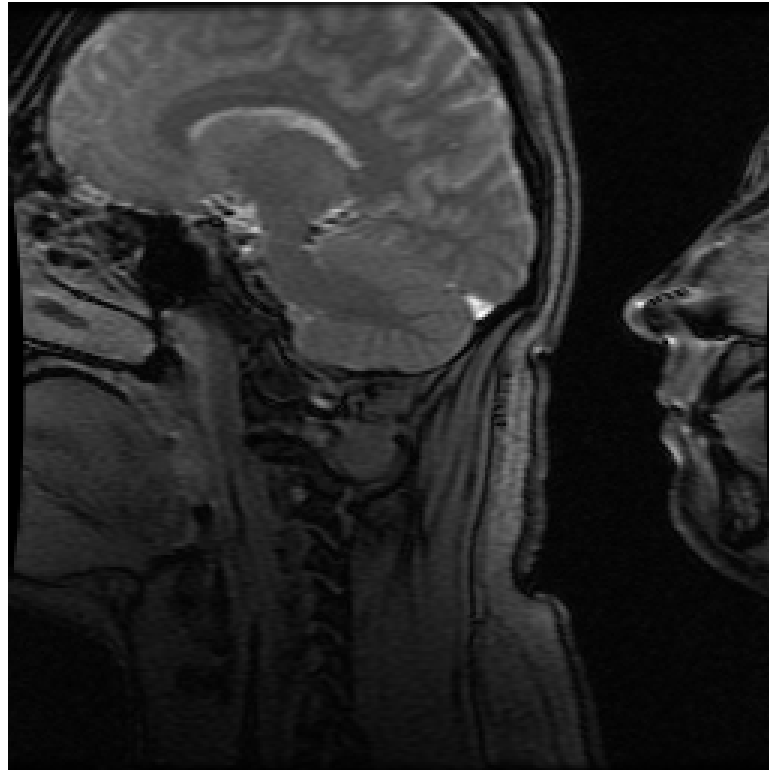


*Figure 2.20: Aliasing artefact. In the image above, the anterior portion of the subject's face was selected outside of the local FOV in the phase-encode direction. As a result, this portion of the subject's face appears wrapped around in the image.*

Motion artefacts are encountered throughout the research presented in this thesis. This type of artefact presents as a dephasing (signal loss) or as a ghosting (rippling) in the phase-encode direction. Some relevant examples of motion are the motion of physical organs (*i.e.*, heart, lungs) and flow of blood through vessels. The artefact results from motion occurring while the image is being collected. Two common methods for reducing motion effects are to trigger the acquisition based on periodic motion (*e.g.*, cardiac or respiratory gating) or to image at a faster rate. An example of motion artefact is shown in Fig 2.21.

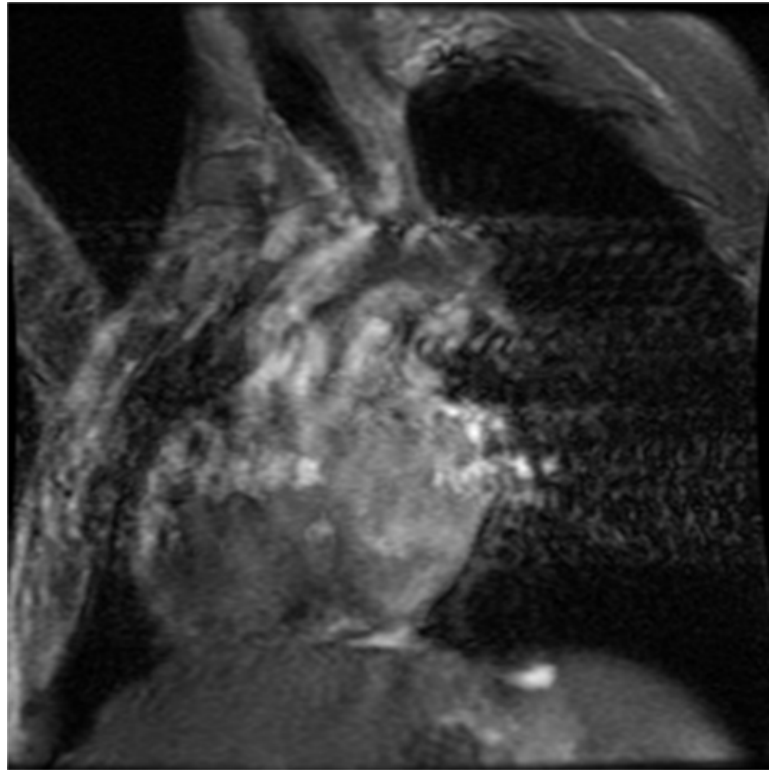


*Figure 2.21: Motion artefact. This image was collected over the course of half a heartbeat. During the collection of the image the heart moved and caused a horizontal rippling artefact in the image.*

There are many types of artefacts that can present themselves in MR images. A few have been mentioned here as they arise throughout the thesis, or efforts are made to avoid them completely. The following sections discuss specific applications of MR imaging, other endovascular catheter tracking with MR and image acceleration methods.

#### **2.4 MR-Guided Catheter Tracking**

Several researchers have looked at using MR imaging for catheter guiding applications (20-22,24,26,40,72,82-87). These demonstrations, for the most part, have been limited to *in vitro* experiments and animal models where the endovascular catheters and devices are localized either passively, by filling the catheter lumen with MR contrast agents (40), or

actively, by attaching small imaging coils onto devices (21). Both passive and active strategies are used to detect the location of devices in MR tracking images. These images are then superimposed over a previously acquired "roadmap" image that contains information about the soft tissue and vascular anatomy, analogous to x-ray fluoroscopy techniques. Active catheter tracking has been more thoroughly investigated by researchers in this field and, therefore, has shown more successful results. Active catheter tracking has been demonstrated in animal models and limited clinical studies. Recently, one group (23) have claimed to be pushing forward with human trials. Strategies for passive visualization have also been studied by research groups,(26,41,88) but have not yet been shown to be clinically viable.

#### ***2.4.1 Active Tracking***

There have been many scientific papers written on the subject of active tracking from the late 1980's until today. This section discusses some of key advancements. In 1996, Atalar *et al.*,(82) demonstrated high-resolution imaging of the descending aortas in cadavers using an active catheter. These experiments did not look at catheter mounted antennas for the purpose of localization within the body, but for imaging at high resolution. This method of vessel wall imaging could be exceptionally useful during endovascular procedures for assessing the severity of disease of the vessel wall. Examples of the images obtained from the intravascular coil are shown in Fig 2.22.

In 1997, Ladd, *et al.*,(89) showed how different antenna coil configurations could be used to generate image signatures. Four basic coil configurations were studied, a single loop (Fig 2.23), crossed loop, return centre, and a solenoid having a return through the centre. Simulations were performed to assess the image profile when the antenna

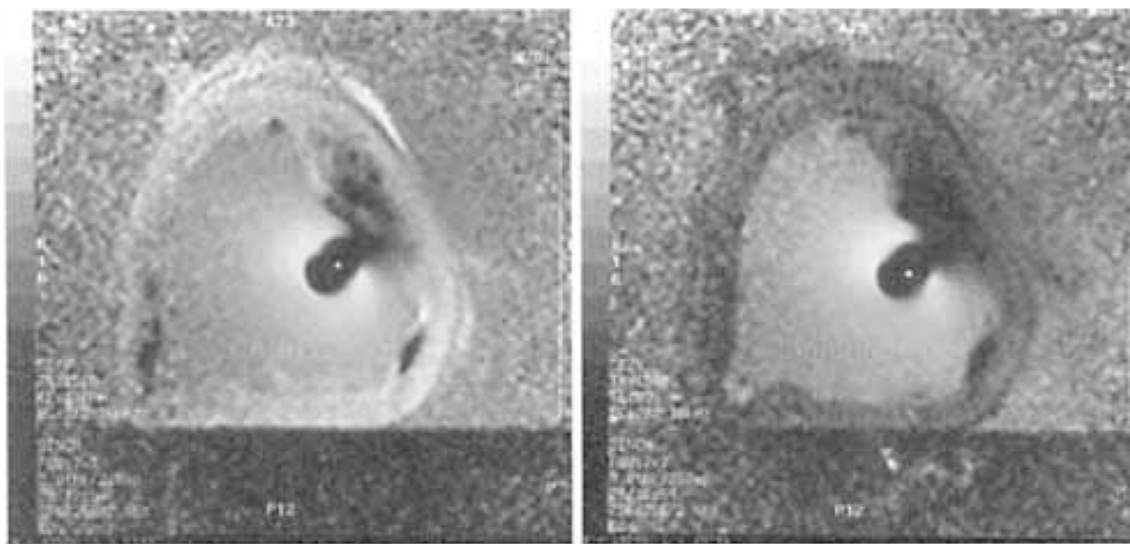


Figure 2.22: Images of post mortem isolated human aorta. The catheter is located towards the middle (signal void) of the images. TR/TE were 1500/17 (left) and 1500/80 ms (right). The voxel size is 0.27 mm by 0.27 mm by 3 mm.

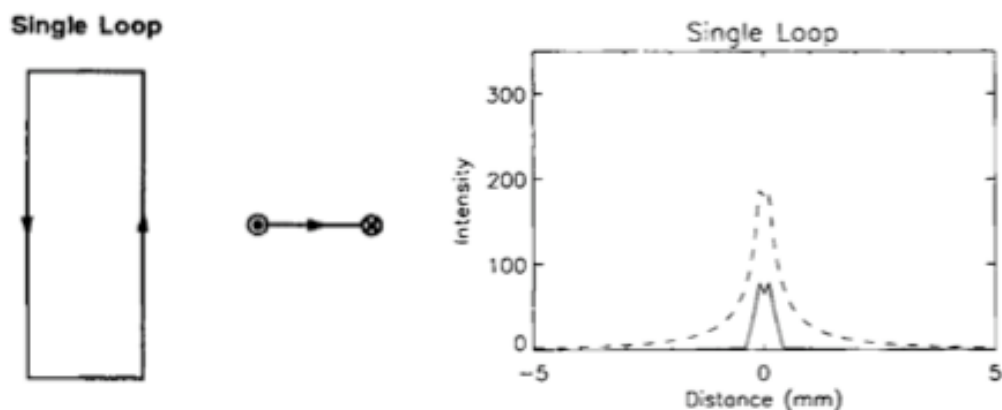


Figure 2.23: Single loop antenna coil (Left) and cross-section profile (Right). MR signal intensity is high near the device and gradually tapers off within 5 mm in either direction. Figure is modified from (89).

was located in the imaging volume. This novel strategy for device detection pushed the focus toward visualization of devices, like endovascular catheters, within the body. This work helped to pave the way for active catheter tracking by showing how different

antenna configurations could be used to create an MR image of the volume directly around an antenna coil. Although this work shows only four coil configurations, the method of analysis could be applied to many other configuration types.

In 1998, Ladd *et al.*,(19) demonstrated active tracking *in vivo* by displaying the high intensity voxels of the device image profile (acquired from the antenna loop) otop of vascular/anatomical roadmap images. This overlay of images is similar to how image overlays are performed in endovascular x-ray fluoroscopy procedures. These experiments were performed using a 5 F catheter, which is a clinically used catheter size in the larger vessels. Pigs were used in this study as an *in vivo* model. These experiments were performed at 1.5 T using sequences found to work in their previous publication.

In 2003, Quick, *et al.*,(21) used fast real-time MR imaging to show how devices could be visualized and tracked *in vivo*. Devices could be navigated up the femoral artery, and into the renal arteries. This work also demonstrated how the device could be pushed up the descending aorta and into the aortic arch and down the ascending aorta.(Fig 2.24) The implementation of a real-time MR imaging system, and a new data acquisition sequence allowed for images to be reconstructed at 3 Hz (3 fps). The catheter image profiles are treated as additional channels when collecting raw MR data. This strategy is advantageous because the anatomical roadmap is acquired simultaneously with the catheter localization image signature. The image profile is then thresholded and fused to the anatomic image (created by the regular coils outside the body). As with the Ladd *et al.*, (19) study, swine were used as the *in vivo* animal model with 1.5 T field strength. One limitation to this study was the low temporal resolution.

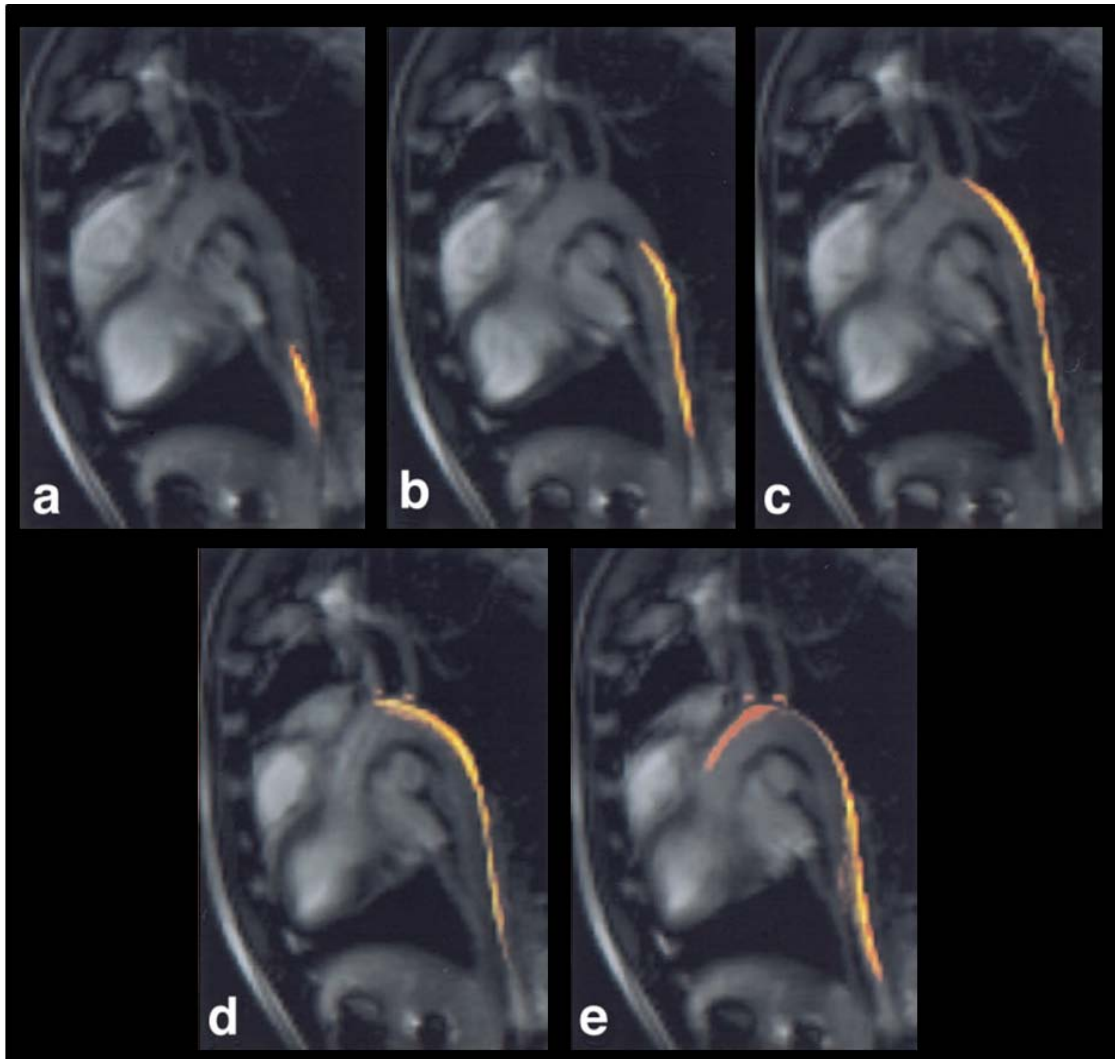


*Figure 2.24: Active catheter tracking in the aortic arch. Still frame images are shown, and were collected at 3 fps using MR imaging. Figure modified from (21).*

In 2003, Omary *et al.*(85) demonstrated catheter and guidewire tracking into the coronary artery of the heart. In these experiments, a guidewire was inserted through the catheter and the susceptibility of the guidewire was used for localization. The active catheter image was overlaid onto an anatomical roadmap. The frame rate in this experiment was much higher than previous experiments,  $>7$  Hz (7 fps). This increase in

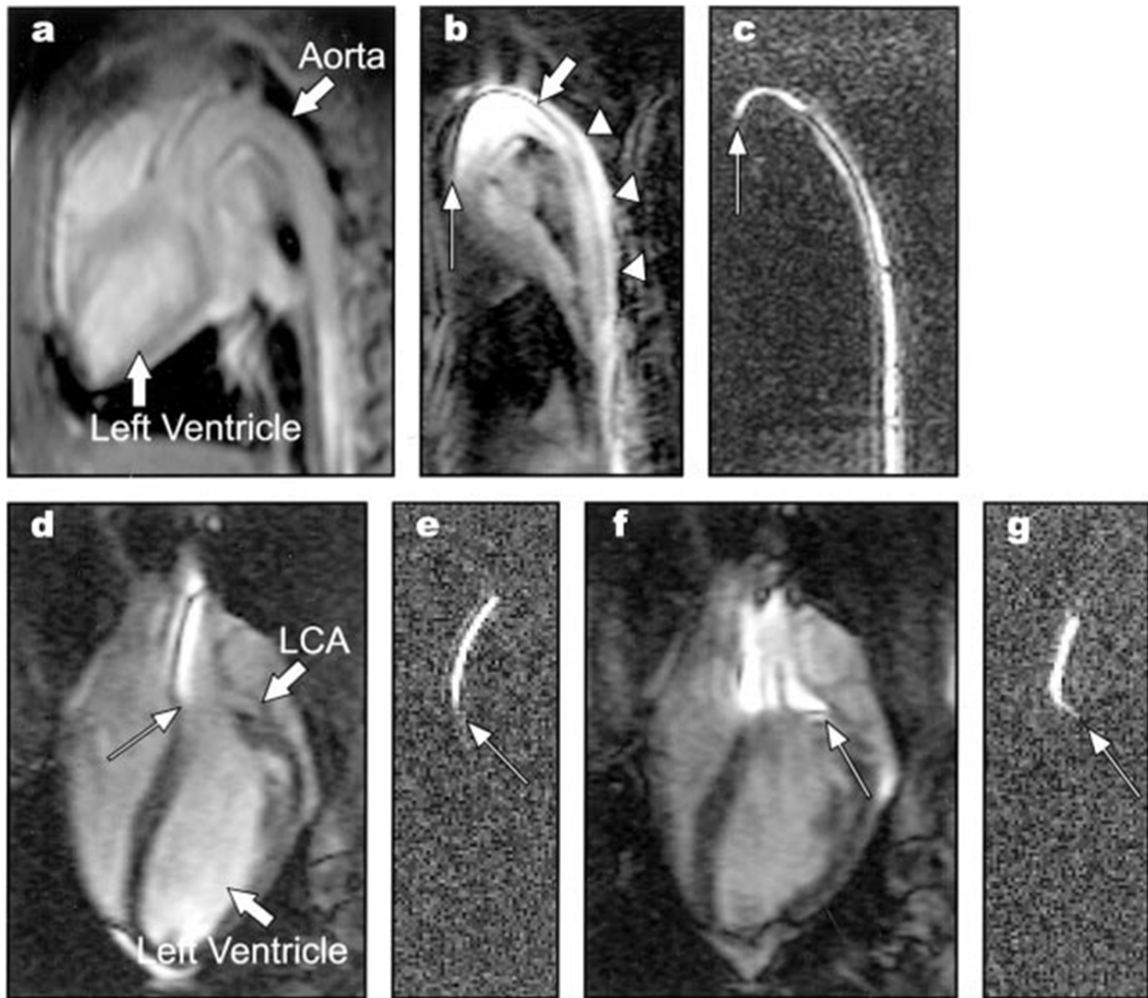


*Figure 2.25: Tracking images using a guidewire to the coronary artery. a-c) coronal images used to guide the catheter into the ascending aorta. d-g) sagittal images to show the catheter going into the coronary artery. f) Contrast agent is injected to verify the position of the catheter tip. This figure was modified from Ref (85).*

imaging rate was achieved at the cost of reducing the matrix acquisition size (70,128).

Tracking images from this experiment are shown in Fig 2.25.

More recently, active tracking has been advanced by improved device metrics and performance. In 2009, Kocaturk *et al.*,(23) performed experiments using a catheter with two active channels. A solenoid tip coil was combined with a second loop coil along the catheter shaft to improve localization of the tip while maintaining conspicuity lengthwise

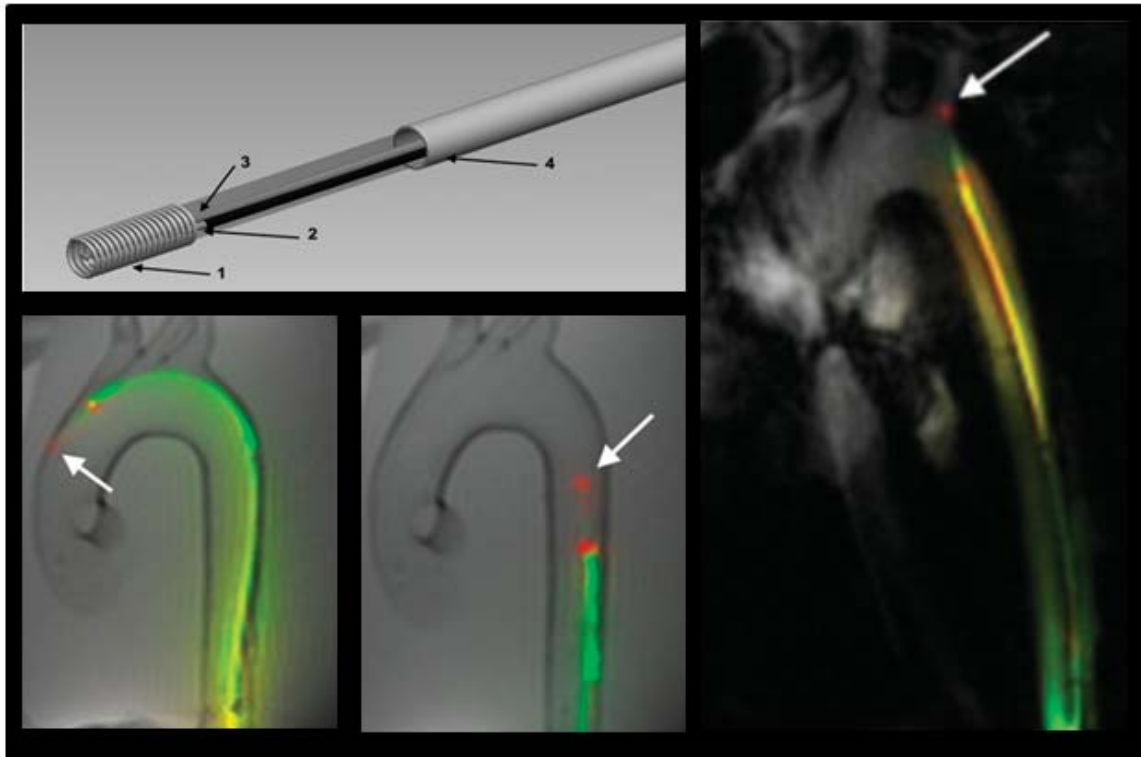


Figure 2.26: Active two channel guidewire. Top left shows solenoid tip configuration and loop antenna. Bottom left two configurations depict the device in an aortic arch phantom. Image on the right shows the device being guided into the brachiocephalic trunk of a swine. Figure taken from Ref (23).

along the catheter. Mechanical tests were performed to insure the device would still behave under standard catheter operating parameters. Magnetic effects such as force on the device and heating were also assessed and deemed within tolerance. These *in vitro* experiments were controlled using robotic manipulators to apply accurate and precise forces during testing. These experiments used a 1.5 T MR scanner for imaging with a balanced steady-state free precession pulse sequence. Animal experiments using a swine model were also performed to assess *in vivo* performance. This research resulted in the first images of a catheter guided to the left subclavian artery using MRI, as shown in Fig 2.26.

Active catheter tracking has been shown as a viable device tracking strategy *in vivo*. However, these proof of concept works have been limited to animal models. The presence of the attached antenna coils may have the consequence that they will not operate like regular catheters or guidewires. Much research and development has gone into the mechanical characteristics of catheters/guidewires used in fluoroscopy and this is set back by attaching coils for MR experiments.

#### ***2.4.2 Passive Tracking***

Passive tracking does not use antenna coils to visualize devices, rather it uses MR contrast materials to localize the catheters and guidewires. Materials that are paramagnetic, ferromagnetic or other strategies that can be used to manipulate the signal in and/or around the catheter and guidewire. Paramagnetic materials such as gadolinium based contrast agents are often used because they create positive contrast.

In 1998, Unal, *et al.*,(40) proposed using a 2D time resolved variable rate  $k$ -space (VARK) sampling trajectory to increase passive catheter tracking frame rates. These experiments also demonstrated how applying a dephaser technique could be used to suppress tissues *in vivo* in order to better visualize a gadolinium filled catheter. In these experiments, catheters were introduced into the femoral artery of a pig, then guided up to the lower descending aorta. When projection dephaser was applied, background signal from the tissues was suppressed, leaving only the device in the image. Roadmap images of the vascular anatomy were collected and fused to the real-time catheter images. Images were collected at 3 Hz (3 fps) for this experiment using a 1.5 T MR scanner.

In 1999, Wacker, *et al.*,(90) demonstrated passive catheter tracking at much lower field strength (0.2 T). This was strictly an application study and did not show significant

technological advancement. They showed reasonably good results given the infrastructure present. Very little was done in the way of technical development, x-ray compatible catheters were inserted into a swine model and visualized at low field.

In 2000, Omary *et al.*,(41) performed passive tracking experiments using an assortment of 5 F catheters that were filled with gadolinium contrast agent. A 4% to 6% concentration of gadolinium was used. The experiments assessed the catheter visibility by looking at tip tracking accuracy, which was measured to be  $\pm 0.41$  mm. Images were displayed at a high frame rate, 3.1 Hz. These experiments were performed *in vitro*.

In 2001, Bakker *et al.*,(88) published results of *in vivo* passive catheter tracking. They compared contrast-enhanced and non-contrast-enhanced devices, concluding that the contrast-enhanced devices were more easily visualized. These experiments were somewhat limited as the temporal resolution was low (0.66 Hz) and digital tissue subtraction was used to reduce background tissue signal. It was stated that a higher temporal resolution would be required for device detection near areas of high motion (*i.e.*, the heart). It was also concluded that digital tissue subtraction would not be an effective technique for catheter localization. It is interesting to note here that the authors did not imply they had successful results.

Also in 2001, Jiang *et al.*,(25) designed methods for coating devices with MR contrast agent. Experiments were performed *in vitro*, and showed how these coatings could be visualized with aid of MR imaging. The coatings were later patented by Frayne *et al.*,(91) in 2002. Amine chains ( $\text{NH}_2$ ) were attached onto polyethylene ( $\text{CH}_2$ ) polymers, and then chelates were added to the amine chains. The chelate could then 'easily' encapsulate gadolinium ions through conventional chelation techniques.(Fig 2.27)

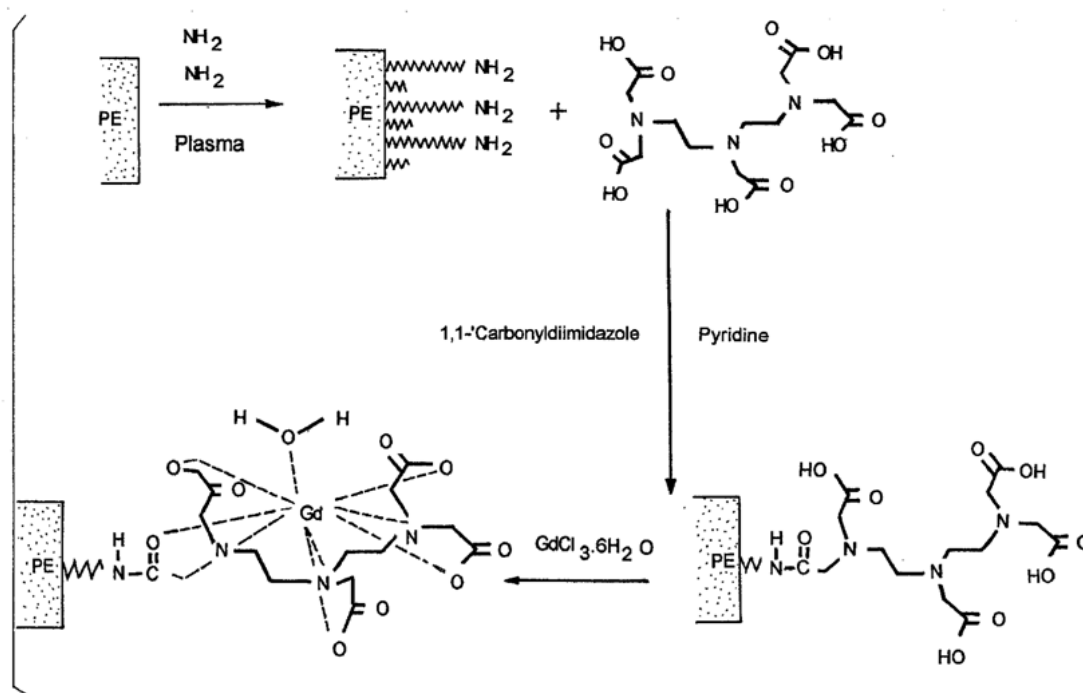
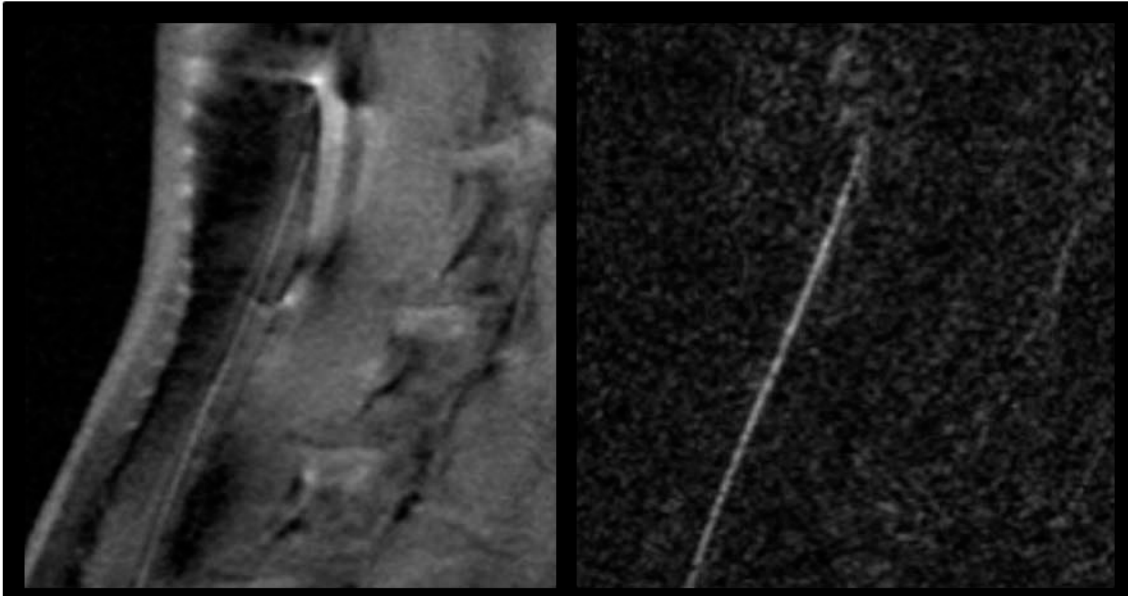


Figure 2.27: Chemical processes for creating gadolinium coating.  $\text{NH}_2$  chains are attached to polyethylene using plasma reaction. Chelates are then attached to the amine chains. Gadolinium can be released from gadolinium chloride by passing an electric current through it, the gadolinium ions are then readily encapsulated when combined in solution. Figure modified from (91).

Polyethylene is a type of plastic used with conventional x-ray fluoroscopy catheters to give desired mechanical characteristics. Polyethylene is the raw outer layer of all catheters before hydrophilic coatings are applied. The chelated coating was intended as a replacement for existing hydrophilic catheter coatings. These coatings have not yet entered commercial production. Manufacturing of such a coating onto catheters takes specific chemical expertise on different sorts of sophisticated reactions and equipment (*i.e.*, plasma reactor, NMR, MR scanner) in order to be produced and validated. In 2006, Unal, *et al.*,(86) proposed a similar method for coating devices in a scientific publication demonstrating *in vivo* application.

In 2002 Green *et al.*,(92) showed how new sequences could be used for device visualization using an *in vivo* canine model. He compared the conventional Fast Low Angle SHot (FLASH) sequence with a magnetization prepared inversion recovery-FLASH (irFLASH) sequence. The irFLASH sequence changed the image T1 weighting and improved the image contrast of gadolinium filled catheters compared to the background signal, making them more conspicuous in images. Although these experiments did show improved image contrast of the catheter there was no strategy for tissue signal suppression. Although the catheters had higher signal intensity *in vitro*, the *in vivo* experiments yielded images in which it was very hard to discern the catheter from the background signal. There was little comment on tracking performance *in vivo* with this sequence, and it was likely poor because of low temporal resolution (1 Hz).

In 2006, Draper *et al.*,(26) published a more refined method for performing projection dephaser imaging when visualizing gadolinium filled catheters *in vivo*. He simulated a 6 F catheter in a homogeneous tissue volume and then applied multiple dephaser lengths showing how the image contrast changed by changing the re-phasing gradient in the z-direction. In this technique, the image volume is modulated with a sinusoid through the image, or according to Eq 2.4, shifting the data in the z-direction of *k*-space. The simulation results were then compared with *in vitro* and *in vivo* data at 3 T. Passive catheter tracking had not yet been performed at this field strength. Images were gathered at a relatively high resolution ( $256 \times 256$ ), shown in Fig 2.28. The experiments concluded that maximum catheter conspicuity was achieved with a dephaser cycle length on the order of twice the diameter of the catheter.(Fig 2.28) For the experiments in the



*Figure 2.28: Catheter visualization using multi-cycle projection dephasing. Left depicts catheter in the vessel of a canine with no dephasing. Right depicts image obtained with optimised dephasing, and the catheter is very conspicuous. Figure modified from (26).*

following chapters of this thesis the optimal dephaser length should be 6 mm for a 6 F catheter.

In 2006, Chen *et al.*, (44) assessed the best roadmapping sequence to use with catheter tracking methods proposed by ref (26). It was concluded that different vascular imaging modes could be used, but that the phase contrast method showed the most promise.

Passive catheter tracking has several desirable characteristics. Passive tracking does not introduce mechanical changes to catheters because the most popular strategy for visualization is to fill the devices with gadolinium contrast agent solution. This bodes well for a passive model reaching clinical application as the devices used in guiding resemble typical fluoroscopy devices. Millions of dollars in research and development have gone into optimizing the mechanical properties for conventional x-ray compatible

devices. This product development is maintained with passive catheter tracking, but not active tracking. Because no metallic devices are required for passive catheter tracking, no heating results in the catheters and guidewires, which has been observed in active tracking experiments.(19,21,22)

### ***2.4.3 Clinical Applications***

To date there have been few interventions performed in humans using passive tracking, which is still considered experimental. In 1997, Bakker, *et al.*,(93) demonstrated passive catheter tracking in the basilic vein of a 47-year old healthy male volunteer using a 3 F catheter. This experiment was the first published application of MR-guided endovascular therapy, and showed visualization of the device.

In 2002, Araki, *et al.*,(20) performed a clinical trial on six patients. Active tracking intervention was used on three patients, while passive tracking methods were used with the other three. It was concluded with this study that both methods would be useful in clinical application. The active tracking procedures in two patients were successful, while all three cases were successful with the passive tracking method. It is possible that the surgeon's familiarity with the passive devices may have biased these results.

In 2005, Paetzel, *et al.*,(94) performed passive angioplasty on the lower limbs of 15 patients having a total of 19 stenoses. Patient outcome was similar to x-ray treatment outcomes and there were no complications observed.

There have been very few reports of clinical MR catheter tracking, likely because the technology is still in the development/pre-clinical test stages. Furthermore, there are few individuals capable of performing these sorts of experiments in humans because

many of the scientists that develop these procedures do not have the medical licensing required to obtain ethics approval.

## 2.5 Acceleration Methods for MR Imaging

The acquisition speed of traditional MR imaging schemes is limited by restrictions placed on maximum slew rate and amplitude of gradient coil strengths by regulatory bodies due to peripheral nerve stimulation.(95) Tradeoffs are regularly performed by the scanner operator by changing acquisition voxel size ( $\Delta x \Delta y \Delta z$ ), acquisition matrix size ( $N_x N_y N_z$ ), and the sampling time ( $\Delta t_s$ , note:  $\Delta t_s = 1 / \text{receiver bandwidth}$ ) since all of which change the stochastic qualities of a single voxel. The relationship of SNR to these acquisition parameters can be expressed as,

$$\frac{SNR}{\text{voxel}} \propto \Delta x \Delta y \Delta z \sqrt{\Delta t_s N_x N_y N_z}, \quad [2.4]$$

Simply by changing parameters to acquire images at a faster rate changes the quality of the image. It should be noted that the relationship expressed in Eq 2.4 assumes a fully sampled 3D volume, the methods described in this section present with noise characteristics that change with many other factors. Fundamentally, increased imaging speed results in reduced image quality.

Increasing imaging frame rates has been a ‘hot topic’ in recent years of MR research. Time-resolved methods, parallel imaging and compressed sensing have been demonstrated and applied to many applications that benefit from increased temporal resolution. This section describes some of the methods that have been proposed by other investigators and are applicable to the later chapters of this thesis.

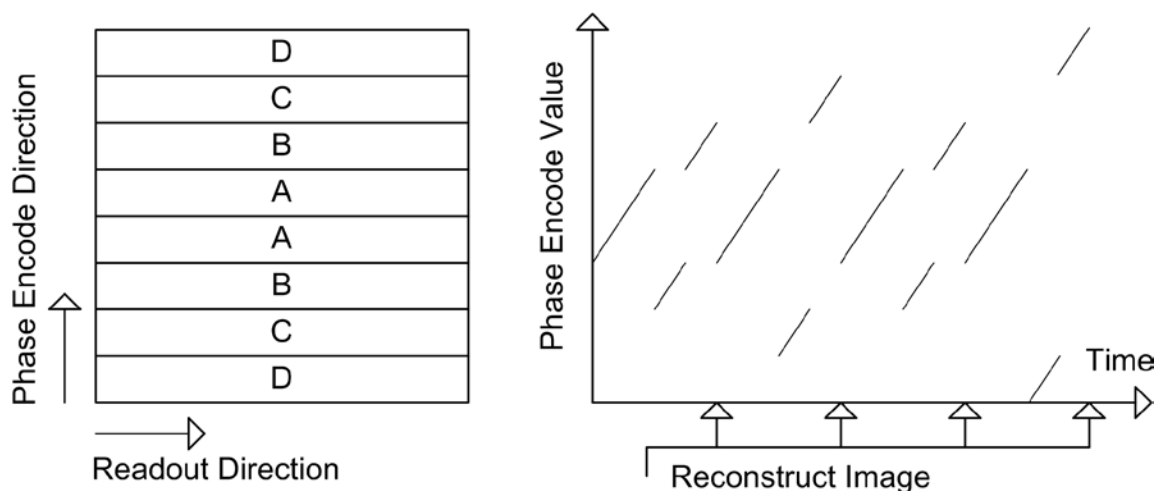
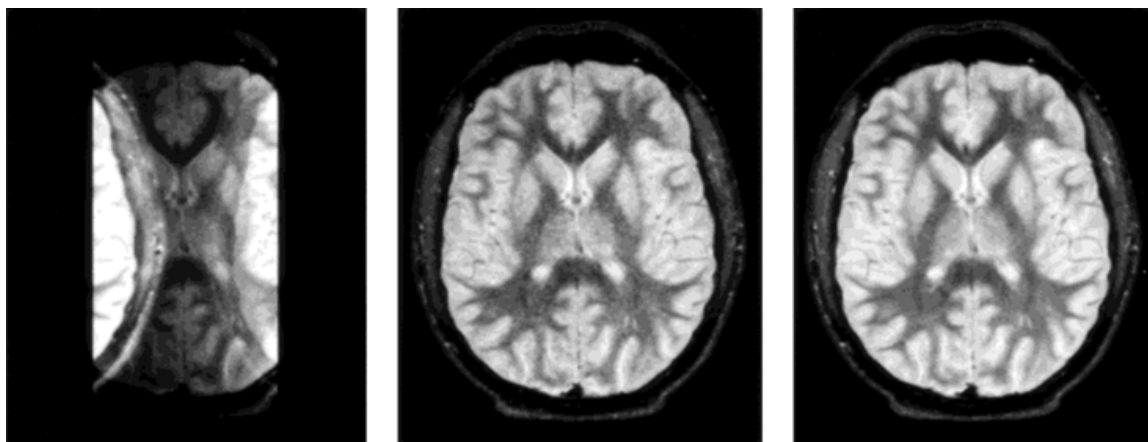


Figure 2.29: Trajectory of the VARK sampling method. The  $k$ -space is divided into 4 different regions and grouped according to the frequency location (left). The regions are then sampled as to acquire the centre regions more frequently than the outside edges. Images can then be reconstructed (updated) at twice the initial rate.

### 2.5.1 Time-Resolved Methods

Non-uniform sampling with buffer holding techniques have been described by several researchers, and have been successful in accelerating the apparent imaging speed in kinetics modeling or contrast passage experiments.(96,97) These methods generally acquire the centre of  $k$ -space more frequently than the outside edges. Measured  $k$ -space values are then held in a buffer until the next values are collected. These trajectories can vary extensively. It should be noted that this method only gives an apparent increase in the imaging rate, whereby images are reconstructed at a faster rate but residual frequency formation is left from the previous image frame. Fig 2.29 is an example used by Unal *et al.*,(40) in 1998 for catheter tracking. This method is described as “VARIABLE Rate K-space,” or VARK sampling for short.



*Figure 2.30: Turbo spin echo images of the brain as an example of SENSE. Left) aliased (folded) image of a single coil. Middle) SENSE reconstructed image from the folded coil images. Acceleration factor of 2. Right) Fully sampled image, which is comparable to the middle SENSE reconstructed image.*

### **2.5.2 Parallel Imaging**

Parallel imaging has been used as a method to improve frame rates by using the sensitivity profiles from multiple receiver coils to allow for a reduction in the number of acquired phase-encode lines. These coils have improved sensitivity when placed closer to the imaging volume, and have been shown to have superior SNR in many experiments.(98,99) Using more advanced algorithms this improvement in coil sensitivity can be used to accelerate imaging frames rates by reducing the total image data acquired.(31-36,40,100)

In 1999, Pruessmann, *et al.*,(34) demonstrated a parallel imaging technique called "SENSE" for "Sensitivity encoding." It was here demonstrated how to combine aliased images that were folded onto themselves by uniform undersampling (only collecting every  $n^{\text{th}}$  phase encode line). Pruessman used the coil sensitivity maps from multiple coils and the aliased image data to solve for a pseudo fully sampled image.(Fig 2.30) The method has been shown to be not overly dependent on coil geometries, though there is a

reported decrease in image SNR with the degree of undersampling, and this decrease is dependent on the coil geometry.

Also in 1999, Sodickson, *et al.*,(31) patented a method known as "SMASH" which stands for "Simulations Acquisition of Spatial Harmonics." In this method, the uncollected frequencies in the phase encode direction are estimated from the undersampled  $k$ -space data. Weights are placed on the undersampled Fourier data of nearest neighbours to estimate the uncollected lines of  $k$ -space data. A composite  $k$ -space is then generated, and converted to image data. Advancements have been suggested upon this method, such as the variable density SMASH (VD-SMASH), where attempts are made to sample more in the  $k$ -space centre than the outer edges.(100) The SMASH-based methods may be preferred for practical implementation as the regularization of coefficients used in the reconstruction is much more robust than SENSE methods due to noise characteristics.

In 2000, Griswold, *et al.*,(33) proposed a method for collecting images at a faster image rate, entitled "PILS" for "Parallel Imaging with Localized Sensitivities". In this method, coil sensitivities were optimized so that each coil used in the reconstruction only collects a portion of the imaging FOV. The image data can be uniformly undersampled, resulting in image data that folds onto itself. Performing a 1D FFT on the each undersampled  $k$ -space line from each coil can allow the images to be combined as pseudo Fourier data, allowing each coil to only collect a small region of the image. This folding is similar to the SENSE method, except that the aliased signal is zero, so the data in essence remains un-aliased.(Fig 2.31) In this manuscript, it is alluded that the images

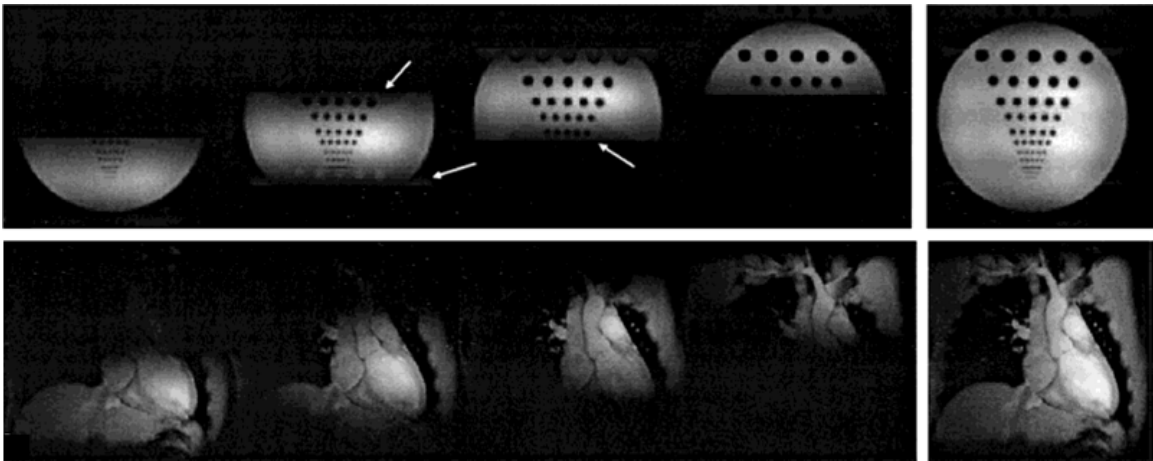


Figure 2.31: Images collected with 2.5 times undersampling and reconstructed with the PILS method. The left eight images show the aliased images from each of the coils. On the right are the PILS combined images. Image modified from (33).

from individual coils can be combined either in the frequency domain or in the image domain, but that combining the image data after the 1D FFT transform is preferred. It is likely that this depends on the coil itself, as this method is very sensitive to coil geometry.

In 2002, Griswold, *et al.*,(32) made further advancements in parallel imaging with a proposal of another method, entitled "GRAPPA: Generalized Autocalibrating Partially Parallel Acquisitions." This method was an improvement on the SMASH technique (31).(Fig 2.32) Rather than combining data with only the neighbour weights to make a single composite  $k$ -space, the weighting range was extended to encompass more points to improve the robustness. This implementation increased the SNR of collected images but at the expense of computational demand. The GRAPPA method is now used with many applications.(83,101-103)

Artefacts that are caused from accelerating too fast with parallel imaging are called geometry factor ( $g$ -factor) artefacts. (Parallel imaging is described further in

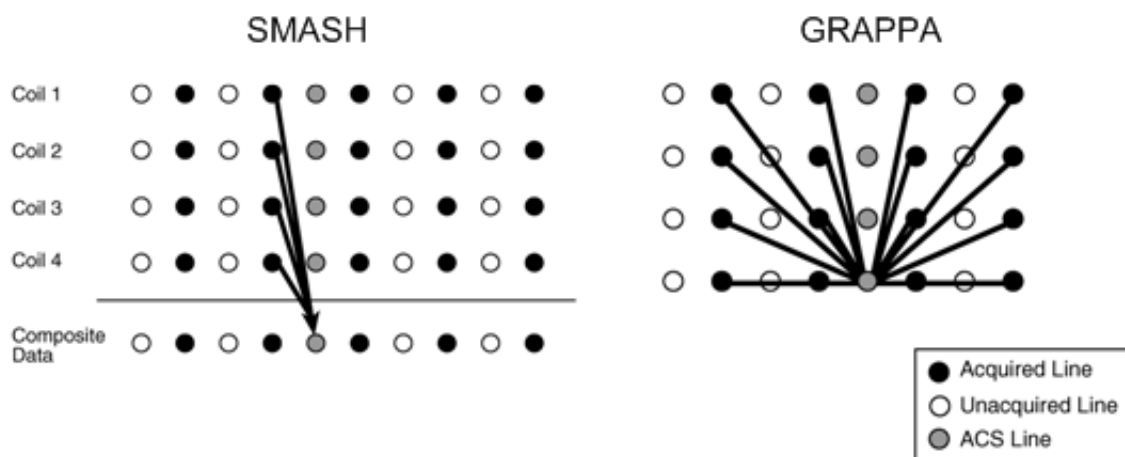


Figure 2.32: How lines of  $k$ -space are solved for with the SMASH (left) and GRAPPA (right) methods. The SMASH method uses the coil image phase encode lines to solve for the missing data line, and with this implementation, a composite  $k$ -space can be found. With the GRAPPA implementation, multiple  $k$ -spaces are solved for with a larger weighting kernel. Each of these  $k$ -spaces is converted to image space and the images are combined via sum of squares. This has shown improvements in SNR over the originally proposed SMASH method. Figure modified from (32).

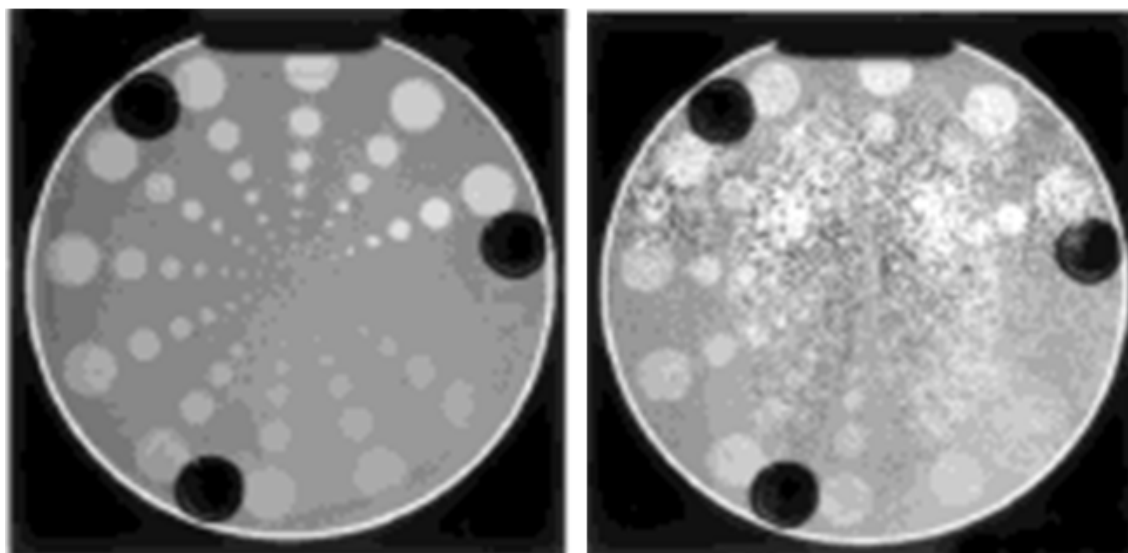


Figure 2.33: Geometry factor artefact. Image on the left is fully sampled. Image on the right is overly accelerated, resulting in distortion in the centre of the image. Image modified from (34).

section 2.5.2) These artefacts were first explained in the SENSE paper,(34) though other forms of parallel imaging have also been shown to have this form of distortion.(33) The

artefact appears in the centre of the image or where the coil sensitivity profiles are coupled to the greatest extent. The signal values at these locations cannot be properly resolved and thus the artefact appears as non-uniform noise. An example of the g-factor artefact is shown in Fig 2.33. This form of artefact can be removed by reducing the parallel imaging acceleration factor or changing the coil configuration.

### ***2.5.3 Compressed Sensing***

Compressed sensing (CS) was developed in the field of pure mathematics for solving underdetermined systems by Tao and colleagues.(104) This theory suggests that a superior solution can be found for underdetermined systems if the solution is known to be sparse, using both the  $L_2$  and  $L_1$  norm instead of the traditional  $L_2$  (least squares) approach only. In 2007, Lustig *et al.*,(35) proposed the application of CS to sparse MR images. Random sampling trajectories are chosen that reduce side lobe height of a point spread function. The zero padded  $k$ -space can then be transformed into image space with use of the inverse Fourier transform. The aliasing artefacts that are present in randomly undersampled image data appear as incoherent noise, and the trajectories are chosen in order to minimize root mean square (RMS) error for the point spread function response. A threshold can then be applied to find the sparse signal. The incoherent aliasing response of this detected signal is then determined and subtracted from the initial signal to reduce the apparent noise in the image. The process is then repeated to determine the remaining signal points that were previously buried in noise. This process is depicted in Fig 2.34. Lustig suggested that use of the wavelet transform could be used to allow CS to be applied to MR images that are not considered sparse. Although an image may not be sparse in the image domain, it may be sparse in the wavelet domain. CS has been

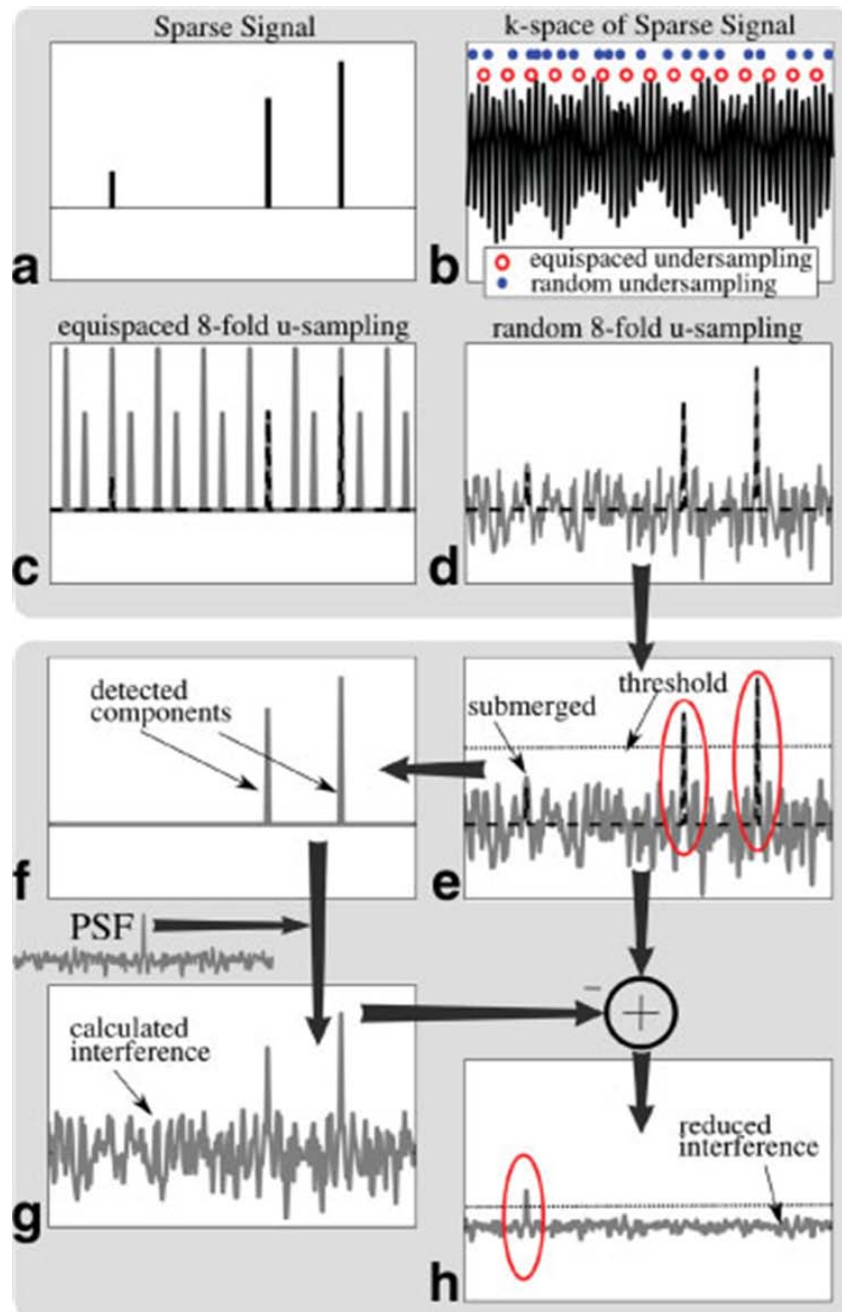


Figure 2.34: Flow chart depicting the compressed sensing process. For a given signal (a) undersampling of the Fourier domain can be performed either uniformly or randomly (b). The uniformly undersampled signal has coherent aliasing, and the location of the undersampled signal is not apparent (c). With random sampling the aliasing is incoherent and presents as noise (d). Signal is determined with detection points above a threshold (e&f). The interference from these points can then be determined (g) and subtracted from the initial signal to detect other points in the data. Figure adapted from (35).

proposed for applications that require fast imaging. Catheter visualization using CS has been simulated (87) and demonstrated (24).

There have been many other methods proposed for accelerating imaging that are not covered in this chapter, as they are not relevant to the discussion in this thesis. The methods described here are used in the coming chapters, and are compared to determine which is most suitable for passive catheter tracking. Comparisons have also been made of parallel imaging and image acceleration techniques (105) but an assessment of which method performs best for the catheter tracking and guiding applications has yet to be undertaken.

This chapter has introduced the reader to the basics of various endovascular therapies, and how medical imaging is used during such procedures. The reader now has the relevant background information about the MR techniques that are used in the passive catheter tracking research presented in this thesis. The next three chapters focus on achieving the key objectives of the project.

## Chapter Three: A Real-Time MR Imaging System

### 3.1 Introduction

Historically, endarterectomy has been the preferred surgical treatment for carotid stenosis. Endarterectomy is an invasive procedure as direct access to the carotid artery is achieved by making a surgical incision in the neck. Angioplasty and/or stenting are more recent and significantly less invasive procedures that treat vascular disease using devices deployed from within the blood vessels themselves.(106) Because angioplasty and stenting are less invasive, these procedures are rapidly being adopted clinically.(2) Once the catheter has reached the stenosis, one of a number of treatments can be used to expand the vessel in an effort to restore blood flow, including angioplasty (the temporary deployment of a balloon to open the blockage) and stenting (permanent placement of a wire mesh to open the blockage).(3)

To conduct endovascular procedures by guiding and visualizing the catheters throughout the vascular system, real-time imaging is needed. Catheters typically incorporate braided metal layers making them highly conspicuous on x-ray images. Other devices have metallic components, including tantalum markers that are added to enhance visibility. For catheter tracking, there are additional imaging requirements, notably, the desire for low latency and high frame rates. X-ray imaging is most commonly used clinically (106) as it is a modality that has many desired characteristics for imaging during angioplasty and stenting – it has high temporal and spatial resolution (up to 60 Hz with  $< 0.5 \text{ mm} \times 0.5 \text{ mm}$  pixels), low latency, and its use is relatively intuitive.

Nonetheless, there are several drawbacks to x-ray image guidance for example, poor soft-tissue image contrast.(64) X-ray imaging, therefore, does not depict key structures that can provide important anatomical context during the procedure. To highlight the vessels it is necessary to inject iodine-based contrast agent from the catheter into the blood. Digital subtraction angiography (subtraction of a mask image collected prior to the contrast agent injection) can be used to form an image of the vessels (64) that can be stored in memory. Subsequent catheter tracking images are then superimposed over top of the stored images. The technique of overlaying tracking images on angiographic images is known as road-mapping.(44,106) In addition, x-ray imaging has poor depiction of non-bony anatomical landmarks, making some tracking applications difficult and making monitoring of therapeutic response impossible in some therapies (*i.e.*, intra-arterial stroke thrombolysis). Aside from the risks associated with the iodinated contrast agents, and the endovascular procedure itself, x-ray imaging procedures expose both patients and staff to ionizing radiation requiring them to use lead shielding and other radiation protection steps.(106)

Several research groups have looked at magnetic resonance (MR) imaging as an alternate imaging modality for catheter guiding applications.(89,90,107-110) MR has several advantages over x-ray imaging, including better soft tissue contrast, the potential for 3D imaging, and no need for iodine contrast agents or protective shielding. These initial MR procedures have been in general limited to *in vitro* phantoms and animal models, and have demonstrated successful catheterization of several vessels, including the hepatic, aortic and renal arteries, in both canine and swine models.(89,90,107-109) These experiments have been proof-of-concept studies, however, and the MR-based

procedures still require further development and refinement.(110) Successful demonstration of viable catheter guidance from the femoral artery, through the iliac and descending aorta, into the aortic arch and then selection of the carotid artery will push the technique towards practical clinical application. The treatment of cerebrovascular diseases (*e.g.*, carotid occlusive disease, cerebral aneurysms, stroke, see §2.1.2) and post intervention monitoring of clinical effect, could benefit greatly from MR-guided endovascular therapy. A large potential demand may exist for such an MR-guided procedure due to the high prevalence of vascular disease, particularly cerebrovascular disease, in the developed world.(111)

MR has drawbacks including lower temporal resolution and gradient field non-linearity. Methods have been proposed for accelerating MR imaging rates.(31,32,34,100,105) Gradient field non-linearity which can result in significant geometric distortion is observed in images collected during real time. Gradient warp correction algorithms are used to correct for this distortion in diagnostic images but it is generally an iterative process that does not work well for real time applications as it increases image frame latency.(112,113) Geometric distortion correction is critical for manipulating devices using imaging, as it is strongly desired to accurately see device positions.

This chapter focuses on the development and testing of a real-time MR imaging system for use in an animal experiment. The overall objective of this research is to successfully guide a catheter from the femoral artery into the carotid artery, demonstrating viability of pre-clinical application. This is a challenging objective when using MR guidance because of the need for coverage of large anatomical region

(pelvis/abdomen/thorax) that have significant motion artefacts (§2.3.4) at the previously described high spatial and temporal resolutions. The first step in achieving this specific objective was to develop a stand-alone system for real-time image reconstruction, and interface it with the existing MR scanner hardware.

## **3.2 Methods**

### ***3.2.1 Real-Time Imaging - Hardware and Software***

Rapid imaging with MR is a developing field; several MR acquisition techniques have been developed to acquire fully sampled images at frame rates of >1 Hz.(26,86,87) A fast gradient recalled echo (FGRE) pulse sequence was chosen for real-time tracking studies because of its speed and image quality, as well as reconstruction simplicity. The FGRE sequence is  $T_2^*$ -weighted, but with application of a crusher gradient in the  $z$ -direction the sequence can also be made more  $T_1$  weighted.

MR data were collected using a 3 T MR scanner (Signa VH/i; General Electric Healthcare, Waukesha, WI) using a modified FGRE pulse sequence. The raw MR data were streamed, in real-time, from the scanner hardware to a real-time computer (Mac Mini, Mac OS 10.5, 2 GHz Core 2 Duo, 4 GB of RAM) using the TCP/IP protocol (Fig 3.1).(114) The raw data were stored in a  $k$ -space buffer space (*i.e.*, a Fourier space array, §2.3.2) and reconstructed on demand. xUnit testing (115) approaches were taken, where individual blocks of code were prototyped in MATLAB (R2010a, The Mathworks, Inc., Natick, MA) then tested to see that they were meeting the necessary requirements. Once confidence in the algorithms was established, they were ported to C/C++ with their respective tests for speed and robustness. C/C++ code was written using

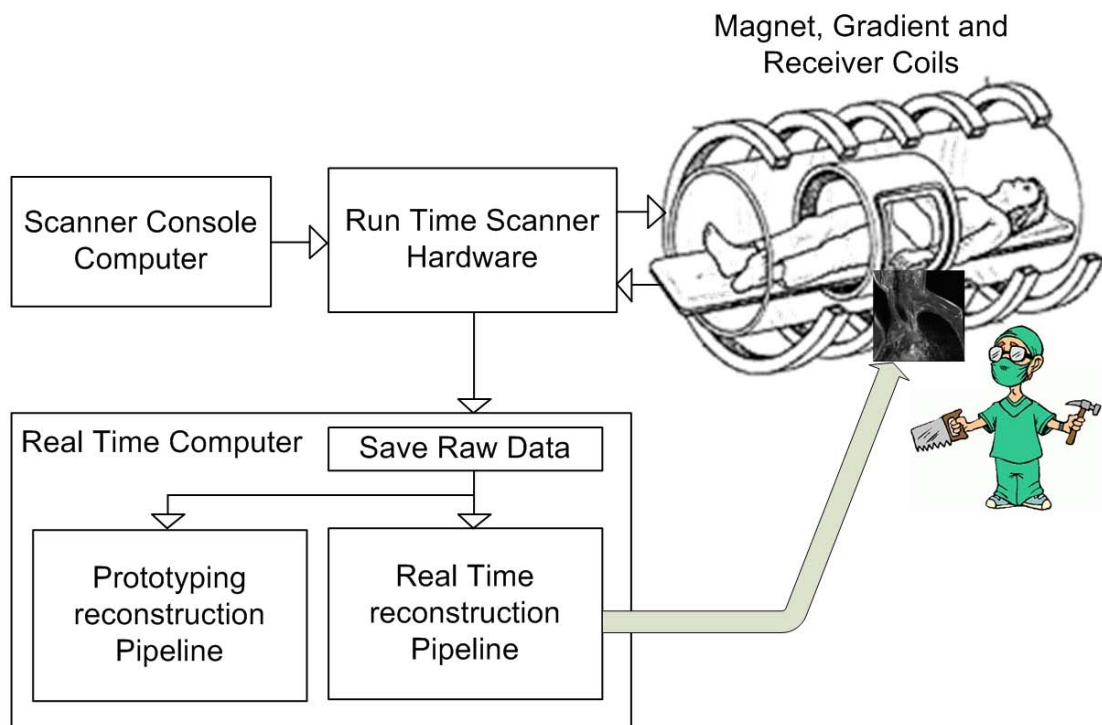


*Figure 3.1: Top) Schematic layout of real time imaging system. The user prescribes the scan parameters on the console computer, these variables are then sent to the run time scanner hardware. The run time hardware performs the sequence, as raw data is collected from the receiver coil, it is ported through the run time hardware and to the Mac mini computer. Data is saved, and if the display is turned on, images are displayed in the scanner room. Bottom, from left to right) console computer, magnet with display, real time computer.*

Qt (Version 4.5.0, Nokia/Trolltech; Oslo, Norway), GCC, and visual studio libraries

(v2008pro, MicroSoft Corp; Redmond, WA) resulting in a cross platform build capable

of execution on Linux, Windows, and Mac OS X operating systems. The FFTw library (116) was used to implement the discrete Fourier transform (DFT) and to reconstruct MR images.

Along with the raw data, the phase encode locations were also transmitted to the real-time computer, so that the incoming data could be properly placed in the  $k$ -space buffer. The software was designed so that it would work with either single or multi channel phased array coils. Phased-array surface coils can improve the overall image quality by increasing the signal-to-noise ratio (SNR) in the images, without increasing the overall imaging time (§2.5).

As necessary, zero padding (ZP) was applied to the  $k$ -space buffer by setting the uncollected high-frequency data to zero. ZP adds no additional information to the images, but improves the visualization of the image by decreasing partial volume averaging with an apparent digital zooming.

### ***3.2.2 Imaging Pulse Sequence***

There are many factors that affect the overall acquisition time and image quality when using a FGRE sequence, including the phase resolution, receiver bandwidth, and repetition time (TR). This unmodified TR was 6.6 ms. The number of phase-encode lines specified at the time of acquisition has a substantial impact on the imaging time, as the two parameters are directly proportional.(117) For example, by reducing the acquisition resolution from  $256 \times 256$  to  $256 \times 128$ , the frame rate was doubled. Furthermore, by increasing the receiver bandwidth, the sample time of the analog-to-digital converter (ADC) is shortened, further increasing the frame rate. An 8-channel phased-array head

coil (General Electric Healthcare) was used for data acquisition and a sum-of-squares algorithm was used to combine images from each coil.

### ***3.2.3 Algorithm Prototyping***

The real time imaging platform was developed using xUnit testing practices. This allows data to be collected but not reconstructed with the real-time computer client. The operations required on the raw MR data to reconstruct images can be first implemented offline in an environment more friendly to development. Offline development also did not require use of the MR scanner. This approach allows for rapid prototyping because the algorithms are then easily implemented in another language. Thus the tests used to validate the algorithm in a higher-level coding language can be re-used in the validation with the subsequent faster, lower-level code implementation. This chapter demonstrates how two separate algorithms can be prototyped and ported for real-time implementation.

Several innovative techniques have been developed for acquisition, including variable rate  $k$ -space collection (VARK sampling, §2.5.1) (40) – an approach that acquires the low-resolution (high contrast)  $k$ -space information at the centre more frequently than the high-frequency (or edge) information at the periphery. A VARK sampling scheme was incorporated into the FGRE pulse sequence. Initially, raw MR data were collected and saved using the real time computer client but images were not reconstructed. The raw data were moved to another computer running MATLAB and the required data processing was implemented to reconstruct the raw data into images. Tests that demonstrated robustness of the code were written to show confidence in the operations. Next, C/C++ functions were written that performed the same operations as the code written in MATLAB. The same tests were run on these blocks of code, and the

same raw data were processed giving the same resulting images. The FGRE sequence was run again with the newly created code and images were reconstructed in real time on the reconstruction computer.

A second algorithm was developed and implemented for correction of gradient-induced image warping. Gradient warping effects are due to non-linear performance of the imaging gradients. Particularly at the periphery of larger fields-of-view, these non-linear effects can result in significant geometric distortion. However, gradient warping correction algorithms can be used to correct for these distortions. Gradient warp correction is performed in one of two ways: 1) analytically, by development of a mathematical model of the gradients and their resulting distortions, or 2) empirically, by measuring the distortion with a grid phantom.(112,113,118) The analytical approach can be complex; thus we have explored a faster empirical approach. An *in vitro* test phantom was constructed from Mega Bloks™ (Mega Brands Inc., Montreal, Canada) to cover the largest FOV, while still fitting into the bore of the magnet (36 cm × 46 cm). The phantom was then submerged in water to provide signal and scanned using a large 48 cm × 48 cm FOV. Raw data was reconstructed into images that were gradient warped, and then geometrically correct image data was generated using the analytic method of the scanner product code. Points were picked on each image to find the spatial shifting relationship between the two images, and a vector field operation was used to correct the warped image data. The algorithm was prototyped in MATLAB, and then ported to C/C++ with the same method as the VARK sampling algorithm.

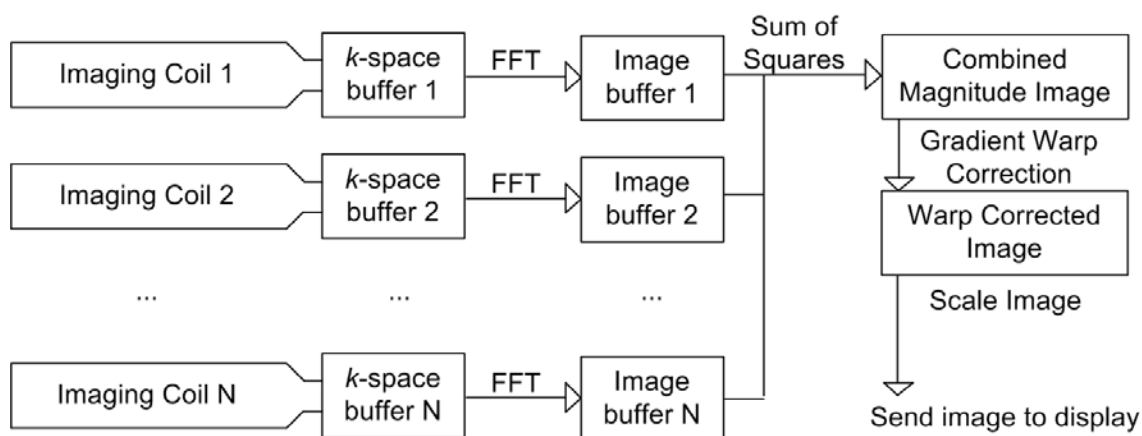


*Figure 3.2: Flow diagram of image reconstruction from multiple channels. Raw  $k$ -space data is acquired from each of the image coils and placed in separate raw  $k$ -space buffers. When enough raw data has been collected to reconstruct an image, the FFT is performed on each of the  $k$ -space buffers to create several image buffers. The image buffers are combined with a sum of squares operation, and the image is gradient warp corrected and scaled for display.*

### **3.2.4 Reconstruction Pipeline**

Image data is collected from multiple coils, each coil has a separate  $k$ -space buffer. When an image is reconstructed, the following pipeline is used: the system is capable of imaging with any number of phase array coils (up to a max of eight as compatible with the scanner). A  $k$ -space buffer holds the data for each imaging channel.

When reconstructing an image a 2D FFT is performed on each of the  $k$ -space buffers to get the complex image data for each channel. The images from each of the separate channels are combined via the sum of squares operation. The sum of squares operation converts individual image data buffers from complex data to magnitude data. Gradient warp correction is then used to correct for geometric distortion. The image is scaled and sent to the display.

All of the C/C++ algorithm code blocks were timed with 1 ms precision and run 1000 times. The timing was performed on a fully sampled 256 x 128 acquisition matrix. The mean and standard deviation were recorded for each block of code.(119)

### ***3.2.5 Image Analysis***

Image quality for the unmodified process was compared with the resulting images from the modified process outlined in §3.2.2, by visual inspection (for distortion or warping artefacts) of the images of a GE phantom and by analysis of SNR. SNR was defined as image intensity of the object over the standard deviation of noise (from the signal in air).(117)

In order to assess the performance of VARK sampling in the presence of motion, a healthy volunteer was scanned while they were talking in the magnet. The volunteer was asked to repeat the vowels 'a-e-i-o-u' and swallow after each vowel spoken. The effect of motion was observed to see if there was significant distortion in the acquired images.

## **3.3 Results**

The vector field was calculated from the grid phantom and is displayed in Fig 3.3. The vector field was able to correct for the large distortion present.

Using the standard FGRE sequence ( $256 \times 256$ , TR = 6.6 ms) , we were able to acquire images at a frame rate of 0.59 Hz. By reducing the number of phase-encode lines from 256 to 128, the TR to 2.9 ms, implementing VARK sampling and reducing the sampling time of the analog to digital converter (ADC), we were able to acquire images at a frame rate of 5.4 Hz with

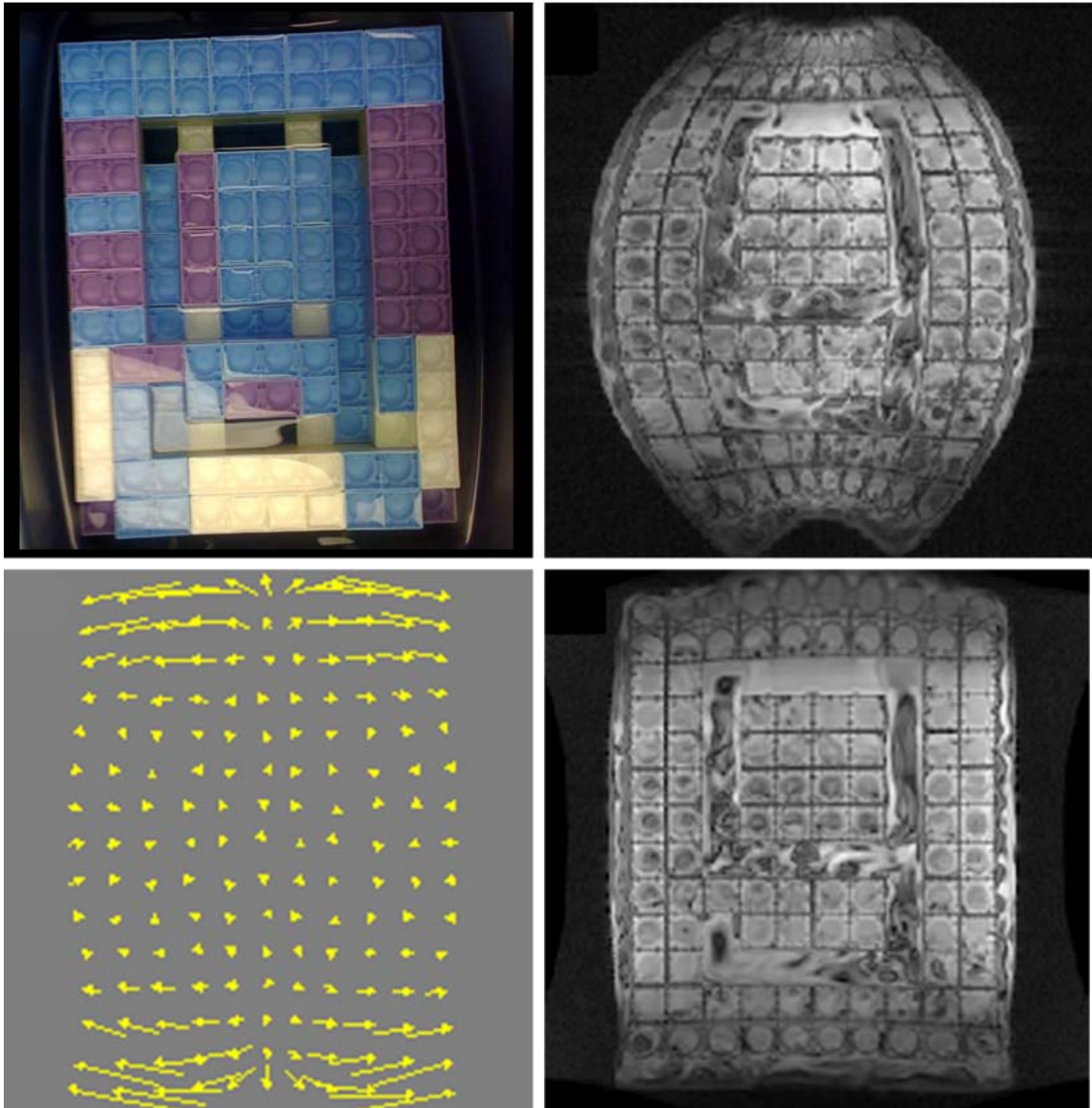


*Figure 3.3: Vector field to correct for gradient warping effects. Top left) picture of the grid phantom constructed from multicoloured blocks while it is submerged in water. Top right) Image acquired with no gradient warp correction. Bottom Left) vector field that can be used to correct the image. Bottom Right) geometrically correct image of grid phantom.*

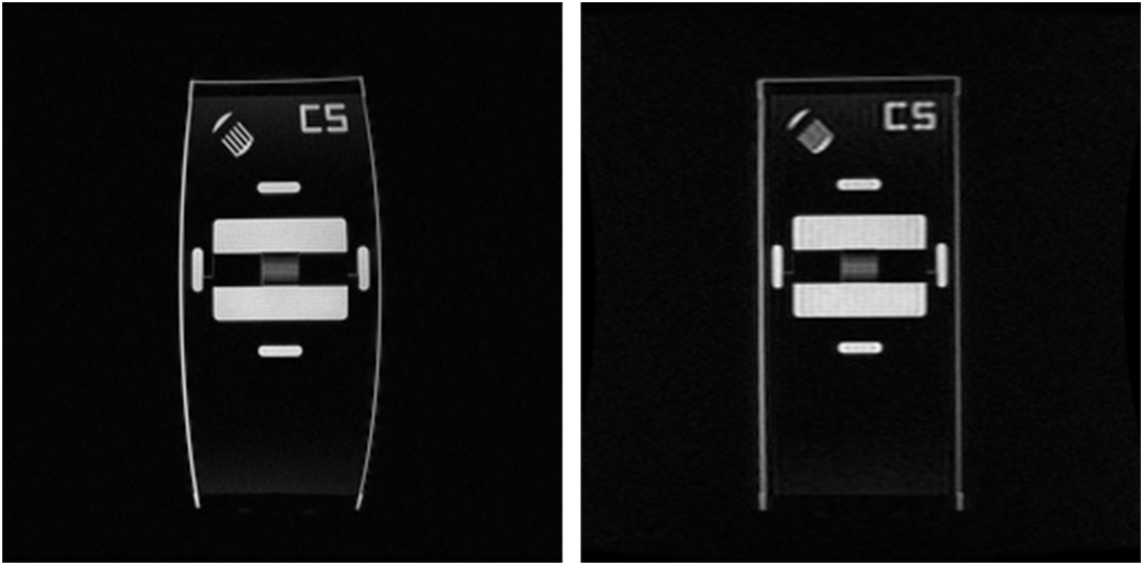


*Figure 3.4: Images obtained using a standard (left) and modified (right) FGRE technique. In the standard image the SNR was measured to be 145. the measured SNR was 133 for the modified sequence.*

little latency. There is little loss in image quality (Fig 3.4). The SNR for the standard sequence was 145, and for the modified technique it was 133.

Images of the healthy volunteer talking in the magnet are shown in Fig 3.5. The volunteer said a full vowel train, but here only the 'a' is said. The vowel is captured in under two seconds, as would be the time to typically say the letter 'a'. At a display rate of 5.4 Hz, there is little noticeable distortion of the images. Some motion artefact exists at the uvula. Furthermore, the uvula moves very quickly and is still visualized with the high frame rate.

The time required to perform each component in the processing algorithm is shown in Table 3.1. From the flow diagram (Fig 3.2), the time required to process an image can be determined. For  $256 \times 128$  fully sampled image, using a single channel images can be reconstructed in 32.85 ms; with a 4-channel coil images can be

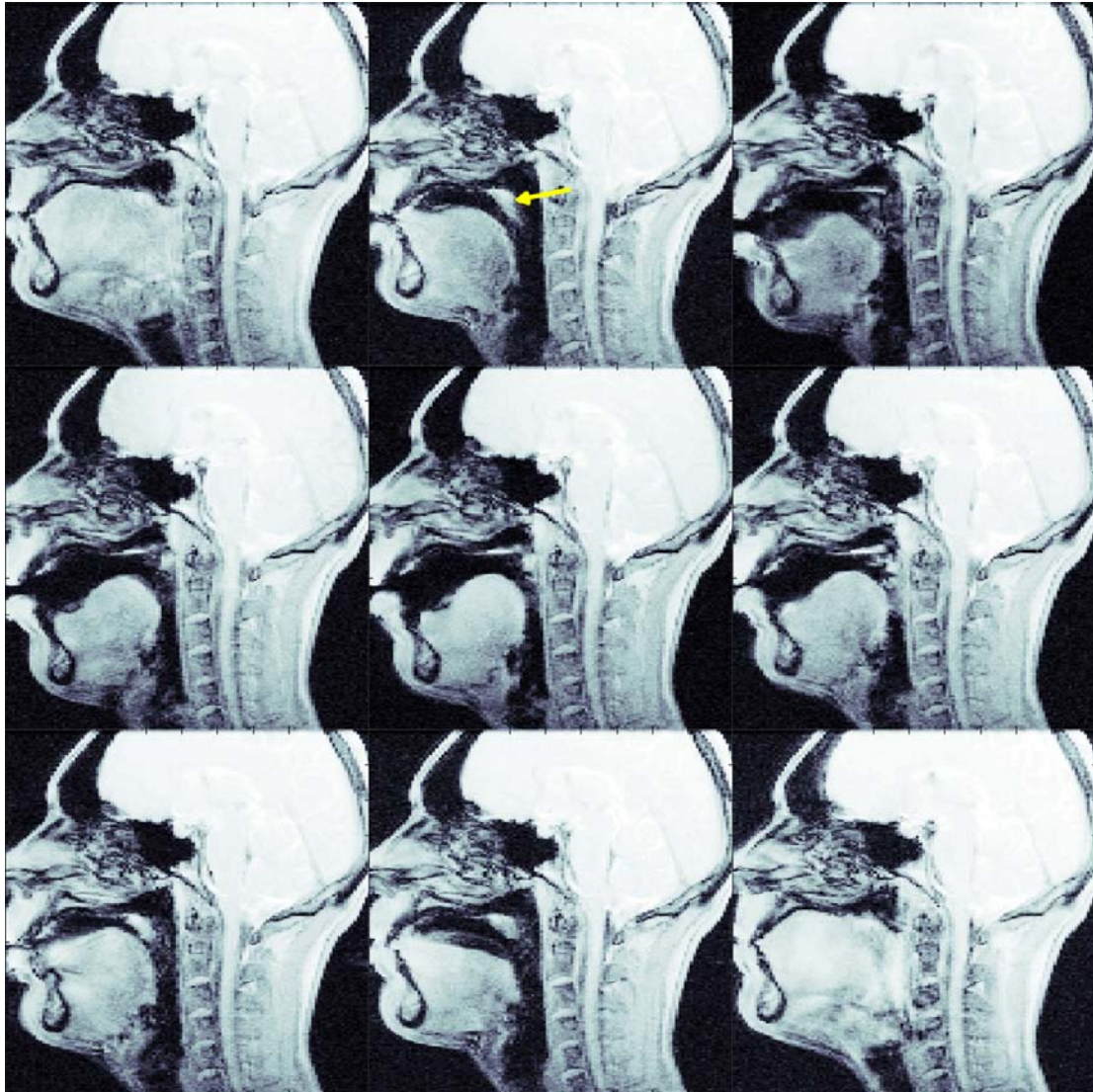


*Figure 3.5: Rapidly acquired MR images of a healthy volunteer speaking. The individual is saying the vowel ‘a’ and then swallowing. Arrow indicates the uvula, which produced motion artefact.*

*Table 3.1 Timing results on algorithms used in real-time image reconstruction pipeline. Image matrix size of  $256 \times 128$ .*

Algorithm	Time
FFT shift	$5.02 \pm 0.08$ ms
2D FFT	$4.17 \pm 0.07$ ms
Sum of Squares	$6.30 \pm 0.10$ ms
Scale Data	$3.85 \pm 0.02$ ms
Gradient Warp Correction	$6.41 \pm 0.21$ ms
OpenGL display	$7.10 \pm 0.83$ ms

reconstructed in 60.42 ms; and when using an 8-channel coil images can be reconstructed in 97.18 ms.

### 3.4 Discussion

To improve the interventional imaging procedure, it is likely a good idea to incorporate roadmap image reconstruction directly into the real-time computer to improve speed and ease-of-use during the procedure. Multi-cycle projection dephasing (mcPD),(26) is an MR imaging technique that has been shown to suppress the signal from background tissues, but highlights small structures (*e.g.*, a contrast enhanced catheter). The mcPD technique changes the rephasing gradient in the slice-encoding direction, to modulate the signal through the imaged volume. Eventually this technique will be used to localize and track the catheter. The mcPD images will be filtered/thresholded to increase catheter conspicuity then overlaid onto roadmap images. Filtering/thresholding will increase the processing time slightly.

MR has historically been plagued with lower temporal resolution than other modalities, and the process of reconstructing images can be on the order of up to 1 s (as images are usually required for diagnostic rather than real time application). Using a single channel imaging coil, data can be reconstructed  $> 30$  Hz, however, with conventional spin warp sequences data cannot be acquired this fast. For example, the image from Table 3.1 was acquired in 371.2 ms for fully sampled data and 185.6 ms for the VARK sampling reconstruction. The image latency was measured in this system to be  $< 100$  ms with an 8-channel coil. In this investigation several previously developed techniques have been combined into a single system, and are able to acquire images  $> 5 \times$

faster than before the strategies were implemented, all while maintaining the general quality of the images.

The future technical direction of this endeavour will be to look at other techniques and algorithms to improve the performance and speed of acquisition. The VARK sampling acceleration method is not a true  $2 \times$  acceleration method because there is residual  $k$ -space data from the previous image used in the reconstruction of the current image. Techniques such as compressive sensing and parallel imaging have shown promise (§2.5).

Development of coils having more than eight channels would be a reasonable goal as well, but multiplexing would need to be implemented to the system which would require substantial hardware modification. For example, other research groups have looked at 128 channel coils for cardiovascular imaging.(120)

There are several other exciting applications for this system, including the ability to image the heart, vocal cords (shown in Fig 2.5), and other areas of monitoring or assessing physiologic motion. Since the images are being acquired faster, they are less sensitive to motion artefacts. This system can be used for reconstructing images and displaying them in real time; the most important future directions will be to find methods for improving the frame rate of catheter tracking images while maintaining image quality, and showing this system as viable by successfully catheterizing a series of canines.

## **Chapter Four: Comparison of Acceleration Methods for Passive Catheter Tracking**

### **4.1 Introduction**

Technological advances have allowed x-ray imaging to acquire images for clinical endovascular interventions with both high spatial and temporal resolution. Modern X-ray systems can acquire images on the order of 15 Hz to 60 Hz (15 fps to 60 frames per second, fps) with spatial resolution (image pixel area) on the order of 0.5 mm × 0.5 mm. Magnetic resonance (MR) imaging has also been demonstrated for catheter tracking applications, however, these experiments have been limited in the most part to preclinical animal applications (§2.4). As described previously, MR has several advantages compared with x-ray imaging as it does not require ionizing radiation, has the potential for 3D imaging, the potential for physiological measurements (such as perfusion and diffusion) and has superior soft tissue contrast. Although there are some clear advantages to using MR in catheter tracking applications, some technical limitations exist (lower temporal and spatial resolution) that have restricted widespread use of this modality in clinical practice.

Catheter localization can be performed either actively, by attaching MR coils to the devices,(19,21,23,24,42,85) or passively, by filling the catheter lumen with contrast materials such as gadolinium.(26,40,86-88,92) Both methods have met with some success in clinical catheter guiding experiments.(20) Active tracking experiments have shown successful tracking to many vessels in animals, including the renal, hepatic, ascending aorta and aortic arch, coronary, and the left subclavian arteries.(21,23,85) Passive tracking experiments have also had success catheterizing many vessels, but has been

restricted near areas of motion (*e.g.*, the heart). Many of the successful active tracking experiments near areas of motion have frame rates on the order of 4 Hz to 13 Hz,(23,85) while passive tracking experiments have been limited temporally, to be on the order of 1 Hz.(26,86,92) Part of the difference between active and passive approaches is due to spatial resolution of the acquired images with passive images being typically acquired but at higher resolutions (acquisition matrices up to  $256 \times 256$  as opposed to  $128 \times 70$  for some active approaches).

With MR imaging, well recognized trade-offs exist between spatial and temporal resolution. For example, MR pulse sequences can be designed for faster frame rates, but often at the expense of producing images with poorer signal to noise ratio (SNR) and/or reducing the acquired matrix size. As images are collected at faster rates, the image quality deteriorates and localization of the catheters can deteriorate. This is a critical observation as localization of devices during endovascular procedures is fundamental to success.

In recent years many methods have been proposed to accelerate MR imaging by using some form of incomplete sampling of the acquisition matrix. Unlike simply reducing the number of acquisitions (and degrading spatial resolution), these methods sample only part of the acquired k-space data and use additional information or non-linear algorithms to reconstruct the image. These new methods include parallel imaging methods (Simultaneous Acquisition of Spatial Harmonics (SMASH), Sensitivity encoding (SENSE) and Generalized Autocalibrating Partially Parallel Acquisitions (GRAPPA)) and compressed sensing (CS).(24,31,32,34,35,87) The parallel imaging techniques typically involve using multiple receiver coils for data acquisition. By using the coil

sensitivity information (§2.3.3), it is possible to decrease the number of acquired data points. CS uses non-linear reconstruction of an image that have sparsity to achieve acceptable image resolution and quality. A more detailed experimental comparison of these acceleration methods is required to determine which method increases the frame rate of the catheter tracking images while maintaining acceptable image quality to ensure correct localization of the devices. In particular, the performance of these approaches in regions of heterogeneous and moving background anatomy, such as in the thorax, must be assessed.

The multi-cycle projection dephaser (mcPD, §2.4.2) method suppresses the signal from background tissues and has been shown to work well *in vivo*.(26,40,86,87) The level of background tissue suppression quality can change between different tissues types particularly if they are not homogeneous. Furthermore, methods such as SENSE can result in non-uniform noise characteristics (noise characteristics based on the coil sensitivity),(34) while CS has been shown to reduce the standard deviation of the noise floor by forcing signal into a few sparse structures.(35,102,103) When comparing multiple reconstruction methods it is also desired to determine the quality of suppression in different regions of heterogeneity.

In this chapter, several commonly used acquisition acceleration methods are compared for passive catheter tracking. With an *in vitro* anthropomorphic phantom, the accuracy of these approaches was assessed in a static model system where the true position of catheter was known. Receiver operator characteristic (ROC) curve analysis was used to determine the performance of detecting the catheter in the accelerated images compared with the known true position. Accelerated images were then acquired *in vivo* in

areas of background motion and the image frames were assessed qualitatively. It is expected that the more computationally intensive acceleration methods will provide better catheter localization, even at higher frame rates. We expect that implementation of these acceleration methods will eventually allow image acquisition/reconstruction at  $>10$  Hz while maintaining sufficient in-plane image resolution ( $< 2 \text{ mm} \times 2 \text{ mm}$ ) for tracking using passive endovascular catheter visualization techniques.

## **4.2 Methods**

### ***4.2.1 In Vitro Model***

An anthropomorphic flow phantom of the aortic arch was assembled by submerging a commercially-available vascular model (Elastrat Sàrl, Geneva, Switzerland) into a container of saline. A variable flow rate pump (Fisher Scientific, Ottawa, Ontario, Canada) was attached to the phantom and set to pumped 3 L / min into the ascending aorta during imaging. A straight tipped 5 F catheter (Cordis, Markham, ON, Canada) containing 0.02 M (4% by volume) gadolinium contrast agent (Magnevist; Berlex Canada Inc, Pointe-Claire, ON, Canada) was inserted into the aortic arch of the phantom and fixed in place.

### ***4.2.2 In Vivo Model***

A canine model was used for these experiments because it has a robust cardiovascular system, similar cardiac and respiratory dynamics as well as vessel calibre to humans, thereby making it a widely accepted animal model for evaluating human endovascular procedures. Ethics approval was obtained from the local Animal Care Committee. The canines were anesthetised with isoflurane (Halocarbon Corp, Beech Island, SC, USA) during interventions. Incisions were made to expose the left femoral artery, the vessel

was punctured and the catheter was introduced. The catheter was guided up into the descending aorta, aortic arch and into the ascending aorta. The catheter lumen was filled with 0.02 M (4%) contrast agent (Magnevist). During imaging, the heart rate and blood oxygenation levels of the canine were monitored. The average heart rate of the animal remained at ~100 beats per minute (bpm) during the majority of imaging, and always remained within a range of 80 bpm to 120 bpm during the experiment. Normal respiration was maintained with a dual phase control respirator (Harvard Apparatus, Holliston, MA) at a rate of 17 breaths per minute, a stroke volume of 300 mL and inspiration/expiration percentage ratio of 50%/50%.

#### ***4.2.3 Imaging***

A computer client (Mac Mini, Mac OS 10.5, 2 GHz Core 2 Duo, 4 GB of RAM; Apple Inc, USA; described in §3) was interfaced via TCP/IP to a 3 T MR scanner (GE Signa VH/i, GE Healthcare, Waukesha, WI, USA). Data were collected with a 4-channel torso phased array coil (GE Healthcare, Waukesha, WI, USA).

Roadmap images were collected of the anthropomorphic phantom using a balanced steady state free precession (bSSFP) sequence for the roadmap image. bSSFP imaging was selected because it provides good signal and has low motion sensitivity due to its fast acquisition time. The bSSFP acquisition matrix was  $128 \times 128$  over a FOV of 22 cm. The TE/TR/flip were 1.4 ms/3.0 ms/25°. The image slice thickness was 3.5 mm and placed through the aortic arch and the descending aorta.

The catheter was visualized with a spoiled gradient recalled echo (SPGR) sequence using mcPD (26) with a cycle length of 6 mm. In order to improve SNR, five fully sampled images were averaged together to determine the true position of the

catheter. The acquisition matrix size, slice thickness and orientation were set to match that of the roadmap; the slice thickness was set to 35 mm and the TE/TR/flip were 1.6 ms/3.0 ms/90°. The mcPD images were superimposed onto the fully sampled roadmap images to show the position of the catheter with respect to the vasculature.

The mcPD catheter tracking technique was used with the four methods of image acquisition acceleration: 1) SENSE,(26) 2) SMASH,(31) 3) GRAPPA,(32) and 4) CS.(35,87) The mcPD sequence was modified to perform these undersampling strategies to allow for both two and four -fold acceleration. The coil sensitivity was measured with a low-resolution FGRE sequence for the SENSE method. SPGR calibration scans were used for SMASH and GRAPPA to match noise characteristics in  $k$ -space. Tikhonov regularization was used for the matrix inversion of SENSE, SMASH and GRAPPA coefficients with an  $\alpha$ -factor of one.(121) The SMASH method used a kernel size of  $2 \times 5$ , whereas the GRAPPA kernel was  $4 \times 7$ . When reconstructing the CS images, the conjugate gradient method was used for convergence (35,87) with sparsity in both the wavelet and image domain as constraints.(87) This method places penalties on the sparseness of the wavelet domain (WT) and the image domain (ID). A penalty is also placed on the total variation (TV) as described in ref (35). Images were reconstructed over a range of TV/WT/ID weighting parameters, and it was found through visual inspection that parameters of 0.04 / 0.001 / 0.1 were effective. Images were reconstructed, interpolated, thresholded, and then overlaid onto the roadmap images.

Roadmaps of the canine's aortic arch and descending aorta were reconstructed using the same parameters used *in vitro*, except with a larger FOV (24 cm). The catheter tracking image data was then collected but with a thicker image slice, 50 mm.

Undersampled data were then collected and reconstructed in a fashion similar to the procedures employed with the anthropomorphic phantom experiment.

#### ***4.2.4 Assessment of Acceleration Methods***

Using the known position of the catheter in the images of the anthropomorphic phantom, classic detection analysis was applied. The true catheter image was thresholded at 50% of the maximum signal intensity value; all spatial locations above the threshold were considered to depict the catheter. It is particularly important that the tracking images minimize both type I errors (*i.e.*, high sensitivity, accurately detect the pixels containing catheter) and type II errors (*i.e.*, high specificity, do not label pixels as catheter where it is not present). For the accelerated phantom images a set of receiver operator characteristic (ROC) curves were calculated to determine the sensitivity and specificity of locating the catheter *in vitro*. Sensitivity and specificity are equally weighted in the ROC analysis, however, it could be argued that type I errors are more detrimental to tracking than type II errors; as such, sensitivity is more important. Image pixel data from a train of 5 consecutive images was used when calculating the ROC curve.

The acceleration methods were scored based on qualitative image characteristics: 1) visibility of catheter, 2) consistency of the catheter signal along the shaft, and 3) tip conspicuity. Each of these criteria were scored with a rating from 0 to 5, with 0 being very poor and 5 being excellent.

Region of interest (ROI) analysis, with regions in the heart, liver, lungs, bowels and peripheral tissues, was used to quantitatively assess the accelerated mcPD images. The mean and standard deviation of the pixels at each of these points were calculated and compared with the catheter signal to determine the catheter enhancement ratio.

#### ***4.2.5 Simulation of Computational Requirements***

For real-time applications, the computational intensity of each data acceleration strategy must be considered when implementing with minimal reconstruction latency. While the data were collected and pre-processed on the real-time MR imaging system, the complexity of the accelerated images prevented real-time image reconstruction. It was therefore necessary to perform reconstruction of the accelerated acquisition data offline. Additional simulations were thus undertaken to determine the required computations per unit time. These simulations did not include any regularization of calibration scans that can be performed before the fast real-time image acquisition is undertaken. Rather, only the computations required during real-time were simulated. The calibration and regularization processes are often the more computationally intensive portions of the PI process; these steps can, however, be done prior to real-time imaging. For the SENSE, SMASH and GRAPPA methods the computations include complex additions and multiplications, a series of complex fast Fourier transforms (FFT) and image magnitude calculations. The CS method is an iterative process that requires complex additions and multiplications, a series of complex FFTs and discrete wavelet transforms (DWT), total variation, and image magnitude calculations. The simulation assumes that the image acquisition parameters were used in the experimental portion of the study.

## 4.3 Results

### 4.3.1 Imaging

The fully sampled catheter image is shown in Fig 4.1 where the catheter is located in the aortic arch of the anthropomorphic phantom. This high-SNR image was used to determine the physical position of the device in subsequent accuracy assessments.

Catheter tracking images from each of the acceleration techniques are shown in Fig 4.2. The SENSE methods performs well at 2 $\times$ -acceleration, but the image quality deteriorates at 4 $\times$ -acceleration due to the geometry factor quality of the coil. The SMASH method also depicts the catheter reasonably well at 2 $\times$ -acceleration; however, the catheter tip becomes indiscernible towards the top of the aortic arch. The 4 $\times$ -accelerated SMASH images performed poorly and the catheter was heavily thresholded along with the noise. The GRAPPA method was successful for both 2 $\times$ - and 4 $\times$ -acceleration, however some ghosting/aliasing artefacts become apparent in the 4 $\times$ -accelerated case (the ghosting artefact fell below the image threshold). GRAPPA is often used in MR angiography experiments (102,103) and these favourable results would be expected to work in similarly sparse catheter images. CS worked well at suppressing the noise in images. Where the catheter was perpendicular to the phase encode direction, the signal behaved as though it were not a sparse signal suggesting that CS requires the image to be sparse perpendicular to the phase encode direction.

The *in vivo* accelerated images (Fig 4.3) show the catheter located in the lower descending aorta for all accelerated methods. The descending aorta is a relatively straight section of vessel and has been the site of many of the catheter tracking experiments in the past.(20,26,40,86,87) The lack of motion (from the lungs and heart) in the abdominal



*Figure 4.1: Fully sampled image of the catheter overlaid onto an anatomical roadmap. This image accurately represents the position of the catheter and was used as a benchmark to assess the other images.*

region allows the imaging protocols to have slow frame rates while achieving high quality images. The catheter becomes less conspicuous in the upper descending aorta (thorax) in all images reconstructed with the PI methods, and it becomes too difficult to determine catheter signal from background noise. The 2 $\times$ -undersampling performed better than the 4 $\times$ -undersampling as expected for all of the methods (scanning faster

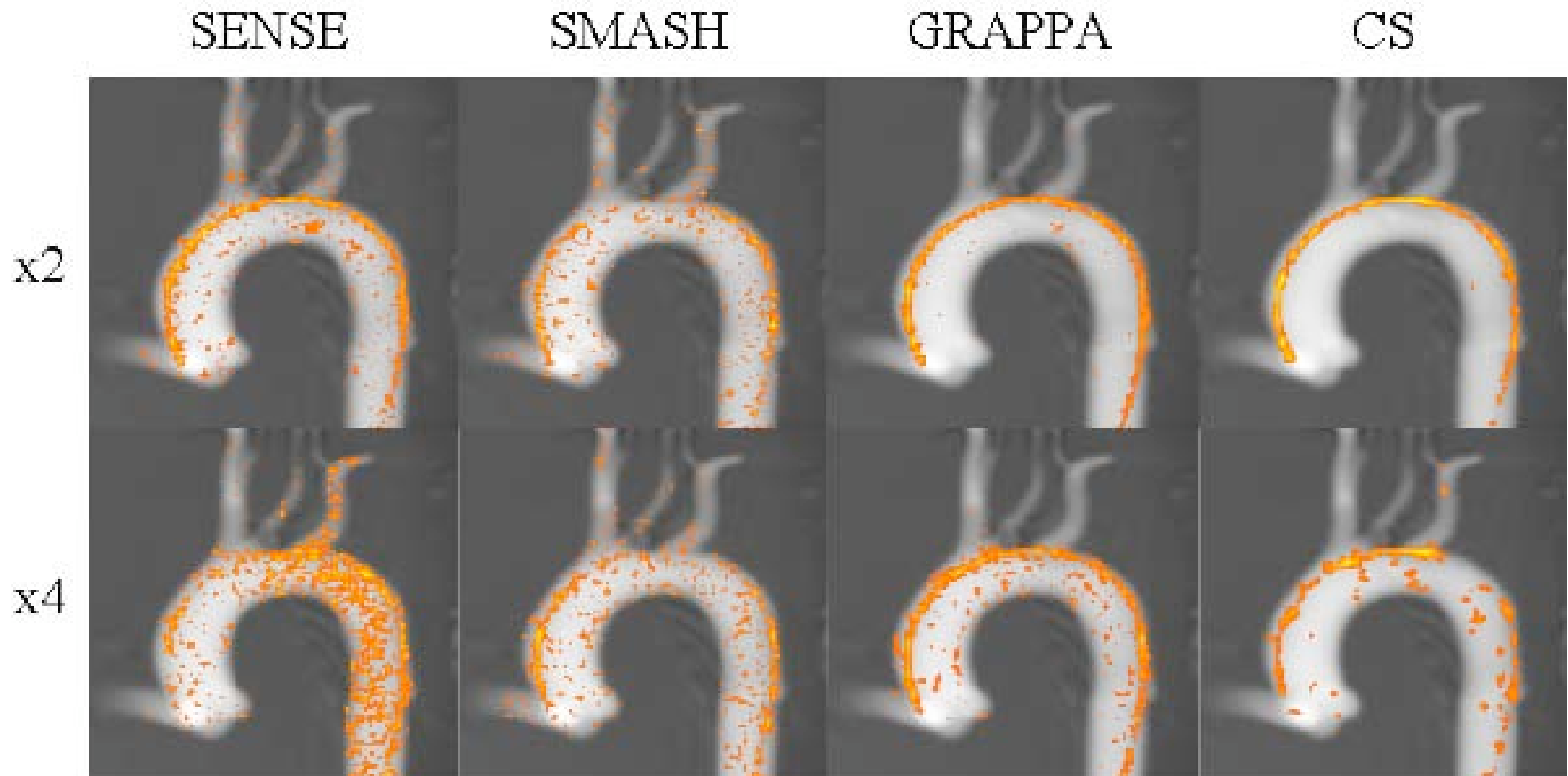
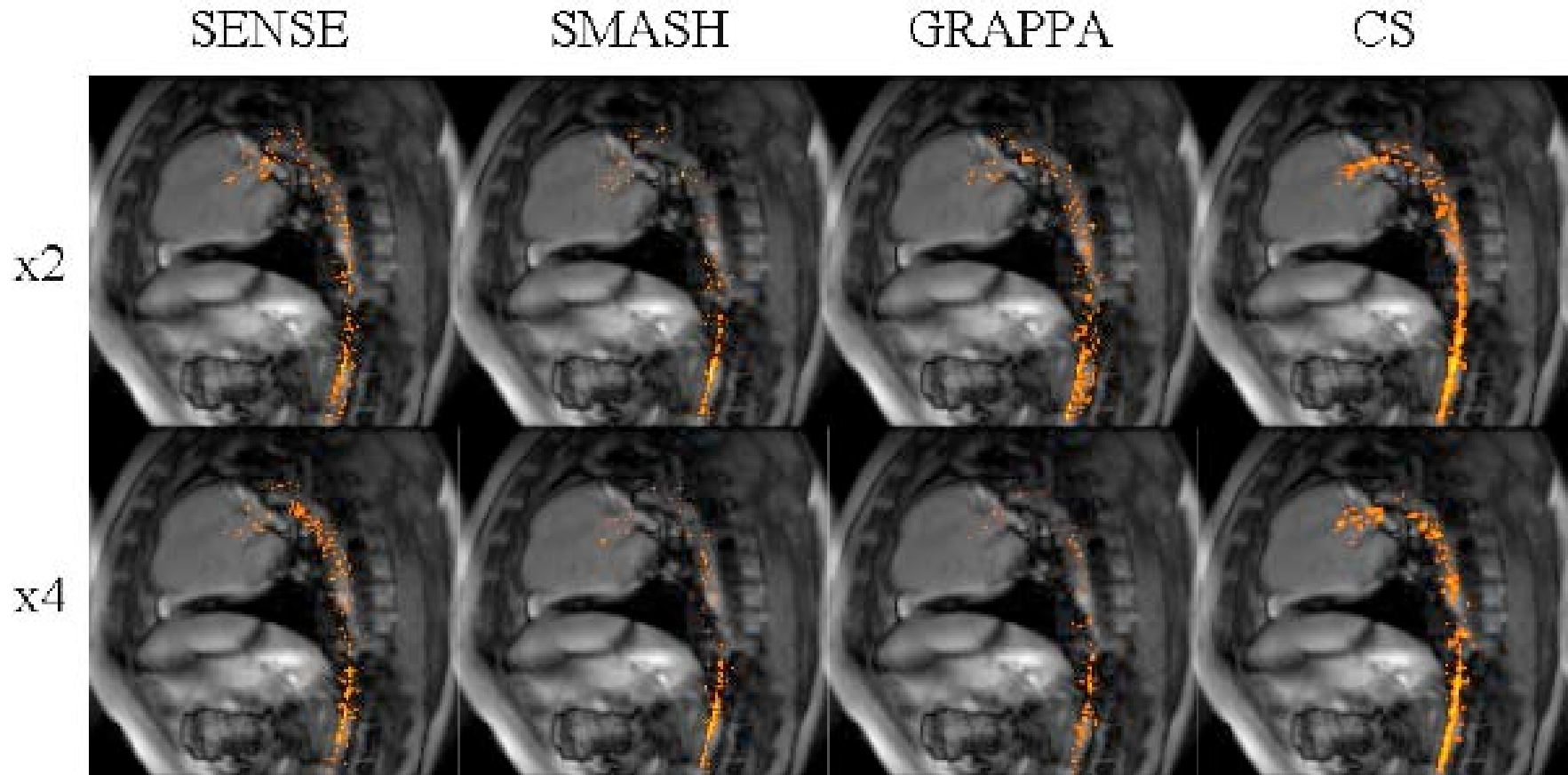


Figure 4.2: In vitro comparison of SENSE, SMASH, GRAPPA and CS for imaging a catheter at  $2\times$  and  $4\times$  acceleration factors. The SENSE, GRAPPA and CS methods perform better than SMASH for both  $2\times$  and  $4\times$  acceleration. The GRAPPA and CS methods show the catheter at  $4x$  acceleration. GRAPPA has poor specificity (type II errors) at  $4x$ . The signal varies along the catheter shaft in the CS images.



*Figure 4.3: In vivo comparison of SENSE, SMASH, GRAPPA and CS for imaging a catheter at  $2\times$  and  $4\times$  multiple acceleration factors. All of the methods visualize the catheter well in the descending aorta, which is an area of less motion. Although signal is present in the aortic arch the signal is significantly corrupted. The CS method performs the best at detecting the catheter.*

generally results in poorer image quality). 5 Hz is likely sufficient to limit motion artefacts, > 5 Hz results in a reduction in image quality.

CS was the most likely technique to reach the desired 10 Hz frame rate and provide acceptable tracking images. However, even with the CS method, the visualization of the catheter tip became unacceptable in the aortic arch. In contrast, the catheter was quite visible in the 2 $\times$ -accelerated CS imaging case, which achieved a frame rate of 5.2 Hz.

#### ***4.3.2 Assessment of Acceleration Methods***

The ROC curves (Fig 4.4.) confirmed that the CS method performed best for the detecting the catheter for both the 2 $\times$ - and 4 $\times$ -undersampling cases. Visual inspection of Fig 4.2 would seem to contradict this finding, particularly the GRAPPA results.

However, the GRAPPA method has poorer specificity than CS because of type II errors in the image. It is likely that CS performs well in the ROC analysis because of the ability of CS to remove the type II errors caused by the noise floor. SENSE and GRAPPA also performed well at catheter detection. SMASH consistently performed the worst in the ROC analysis, which supported the qualitative observations (Fig 4.2).

Although ROC characteristics determine the statistical performance of the methods, it neglects some of the desirable, but more qualitative characteristics of each of the methods. Qualitative scores for each of the acceleration techniques are shown in Table 4.1. From this scoring process the preferred method of acceleration is the CS technique.

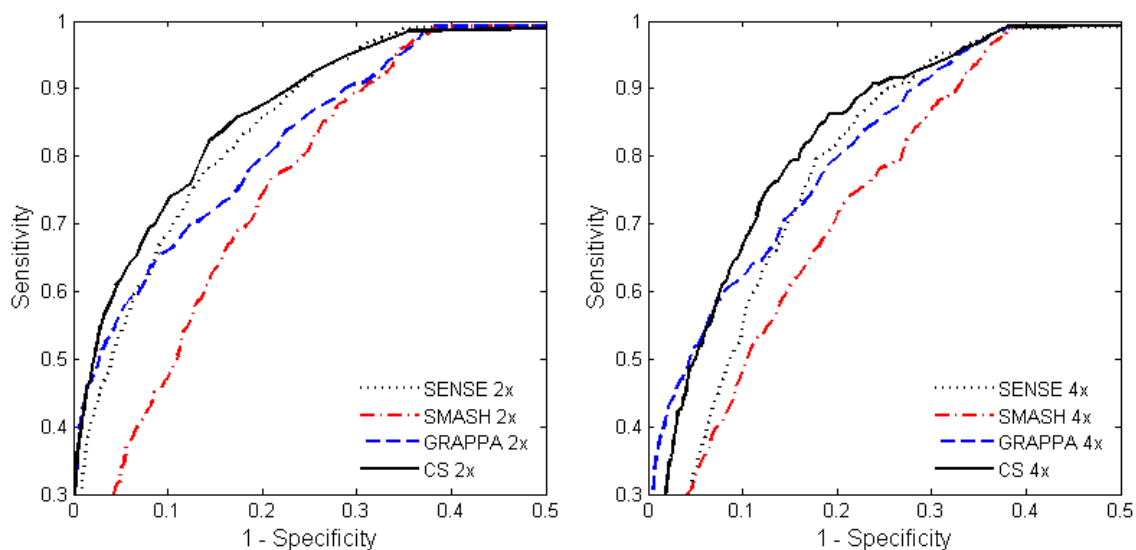


Figure 4.4: The receiver operator characteristic curves of SENSE, SMASH, GRAPPA, and CS for 2 $\times$ - and 4 $\times$ -acceleration. Images from Fig 4.1 and Fig 4.2 were used in calculating the curves. The CS method is most desired based on ROC analysis as it produces the fastest frame rate while maintaining detection of the catheter.

Table 4.1 Scoring of the qualitative factors of each acceleration method. The preferred method based on this assessment is the CS technique with 2 $\times$  undersampling.

Method	Undersampling Factor	Visibility of Catheter	Consistency of signal along shaft	Tip Conspicuity
SENSE	2 $\times$	2	2	3
	4 $\times$	1	1	1
SMASH	2 $\times$	1	1	1
	4 $\times$	1	1	2
GRAPPA	2 $\times$	3	3	3
	4 $\times$	2	3	2
CS	2 $\times$	4	3	4
	4 $\times$	3	2	2

The catheter enhancement ratio for each of the acceleration methods in different tissue regions is shown in Table 4.2. These results show uniform background suppression across the image. CS yields the most superior catheter enhancement ratio.

#### ***4.3.3 Simulation of Computational Requirements***

A plot of computer computations per unit time versus the acceleration for each of the methods is shown in Fig 4.5. Although CS performed well in the ROC analysis, the computational requirements used for CS reconstruction are demanding. The SENSE and SMASH methods, surprisingly, require the least computations during run time. This reduction is due to reduced FFT calculation demand for these methods. As the acceleration factor increases in the SENSE method, the FFT demand is reduced proportionally. Although there is a matrix multiplication required afterwards, these computations are marginal compared to the FFT calculation. The SMASH method combines the data from multiple coils in  $k$ -space, and requires only a single FFT, rather than one for each imaging channel. GRAPPA creates several composite  $k$ -spaces and thus requires an equal number of FFT calculations as the fully sampled approach, plus additional matrix calculations required to solve for the missing  $k$ -space lines. The computational demand of GRAPPA can vary depending on the kernel size chosen to solve for this missing data. CS is an iterative method requiring orders of magnitude ( $> 30\times$ ) calculations than the fully sampled approach. Realization of CS for real-time application will require some form of parallel array processing or a new form of implementation that is transform-based rather than convergence-based to reach practical implementation.

*Table 4.2 Catheter enhancement ratio for different regions of the image. Each of the methods show similar background suppression across the images, but CS has the best ratio.*

ROI location	Undersampling	SENSE		SMASH		GRAPPA		CS	
	Factor	mean	standard dev.	mean	standard dev.	mean	standard dev.	mean	standard dev.
Heart	2x	12.20%	6.25%	10.16%	5.12%	7.63%	4.58%	3.31%	2.76%
	4x	9.69%	7.50%	7.29%	3.83%	5.56%	3.11%	2.77%	2.66%
Liver	2x	10.40%	5.88%	9.40%	4.79%	6.97%	4.07%	2.49%	1.96%
	4x	8.45%	6.03%	7.22%	3.86%	5.21%	2.93%	2.05%	2.66%
Lung	2x	10.76%	7.41%	9.25%	4.87%	6.78%	3.54%	2.97%	2.68%
	4x	10.30%	8.39%	7.15%	4.87%	5.15%	2.83%	2.05%	2.63%
Bowel	2x	14.22%	7.35%	10.19%	5.61%	8.22%	5.50%	3.83%	3.68%
	4x	9.66%	7.50%	7.76%	5.61%	6.29%	3.74%	2.05%	2.81%
Perifferal	2x	7.80%	5.51%	9.67%	5.06%	7.14%	4.22%	2.71%	2.12%
	4x	8.56%	6.58%	7.20%	3.90%	5.22%	3.06%	2.05%	2.14%

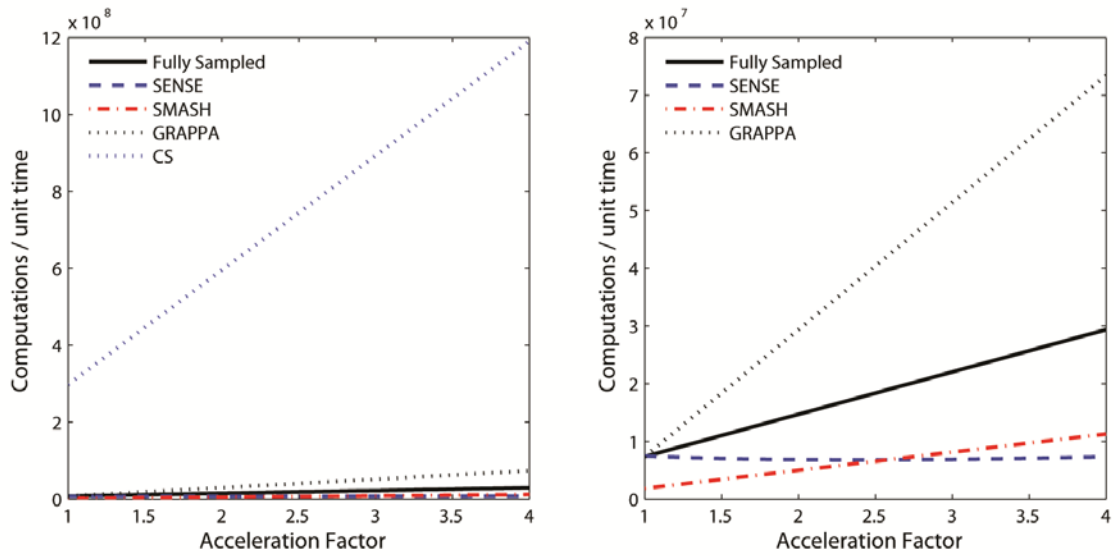


Figure 4.5: Run-time computational requirements of acceleration factors. CS is an iterative approach, and with the conservative approximations used in the calculations here the method still requires an order of magnitude more processing power (left). SMASH and SENSE require less calculations than full sampling because of a reduction in the size/number of FFT calculations required, while the GRAPPA method requires the same number of FFT calculations plus additional coefficient multiplications (right).

#### 4.4 Discussion

As per the hypothesis, more computationally intensive reconstruction methods did indeed perform better. The CS approach performed best based on ROC analysis, and was the most demanding computationally while the GRAPPA method was second. An accelerated frame rate of 5.2 Hz was achieved while maintaining visualization of the catheter.

Resolution of  $< 2 \text{ mm} \times 2 \text{ mm}$  was maintained for both the *in vitro* and *in vivo* portions of the experiment. This image resolution is on the order of the catheter diameter and is required for imaging such devices. Higher resolution can be achieved but at the expense of reduced SNR and reduced frame rate.

In these CS experiments, 64 and 32 phase-encode lines were collected (accelerations of 2× and 4×). Other experiments have used higher CS acceleration factors (>8 times).(24,35,87) It should be noted that these acceleration factors were achieved in simulation, in 3D, and are associated with long TRs, but maintained acceptable image quality. Those experiments were 3D acquisitions and involved collecting many more phase-encoded lines (>2048 for a 3D volume, frame rate = phase encode number × TR) in two phase-encoding directions. The experiment described in this chapter uses CS in the 2D case, which as described by Lustig *et al.*,(35) is the least favourable method. The 2D case still results in the highest frame rate available making it least susceptible to motion. CS also results in non-uniform catheter signal along the shaft. This may be of particular concern if the signal loss is near the tip of the catheter. One potential advantage of CS is that it is independent of coil position while PI methods can be sensitive to a coil shift during the intervention.

This study has compared acceleration methods for passive catheter tracking in the presence of cardiac motion and found the CS method to perform best given experimental parameters both qualitatively (*via* ROC analysis) and quantitatively (*via* characteristic scoring). The CS method was however the most computationally intensive reconstruction method.

## **Chapter Five: Passive MR Catheter Tracking from the Femoral to the Carotid Artery in Canines.**

### **5.1 Introduction**

Magnetic resonance (MR)-based catheter tracking applications have seen significant technical developments in recent years. Many pre-clinical experiments have been performed with animal models to visualize endovascular devices.(21,23,24,26,86,87) Emerging MR-based technologies are desired for such procedures as they do not expose patients and staff to harmful ionizing radiation. Conventionally, x-ray fluoroscopy imaging (§2.2) is used for imaging in clinical endovascular procedures. However, as a modality, MR imaging is preferred to x-ray imaging because of the ability to better image soft tissues and to acquire additional image contrasts. X-ray imaging has much better spatial and temporal resolution - although recent advances in the methods used to acquire and reconstruct MR images (including Chapter Four) have moved endovascular MR closer to technical feasibility and clinical applicability.(24,31-35,87,100,105)

Catheters can be visualized in MR imaging using either 1) active tracking, where antenna coils are mounted on the devices,(19,21,23) or 2) passively, with materials such as gadolinium-containing contrast agents or metal.(26,86,93) Active tracking has been demonstrated in more *in vivo* experiments and has been associated with the more successful results. This observation, however, may simply be due to the fact that more research groups are investigating and assessing active tracking strategies. Active tracking has been used to guide catheters into the renal, aortic arch, subclavian and coronary arteries.(21,23,85) In comparison, fewer research groups are developing and evaluating

passive tracking techniques, though the *in vivo* application has been demonstrated in the descending aorta and renal arteries.(41,86,88) Experiments using passive tracking techniques have tended to have lower image frame rates (0.5 Hz to 1 Hz) than active tracking experiments (4 Hz to 9 Hz). In Chapter Four, an ensemble of advanced methods for MR image acceleration are demonstrated to solve the problem of low temporal resolution in passive tracking experiments. In many ways, passive catheter tracking represents a more natural progression from currently used x-ray based approaches and thus would be preferred for such MR-guided interventions as this would allow the use of many existing endovascular devices. This re-use of devices is important given the considerable research and development that has already occurred. The methods developed for passive tracking could also be implemented with active tracking techniques depending on local infrastructure, staff preference, or specific procedural circumstances.

MR based endovascular experiments to date have generally focussed on cardiovascular applications. Electrophysiological (EP) ablation has been demonstrated and will likely become an important key clinical tool.(122) Using MR imaging, the clinical effect of these therapies, ablated tissue, can be visualized, something that cannot be done with x-ray. Other MR-guided endovascular therapies would similarly benefit from an improved ability to monitor therapeutic effects including, for example, intra-arterial stroke thrombolysis.

X-ray-based neurovascular treatments have become very popular for the treatment of stenosis, aneurysm and stroke,(2,3) however there has been little research effort into MR based neurovascular procedures. Unlike other targets for MR-therapy, the brain is

relatively stationary and MR imaging is the preferred method for detecting and assessing many neurological disorders.

Conventional devices used in x-ray imaging often use metal as a material in manufacturing. Metal provides both desirable mechanical properties and enhanced x-ray attenuation coefficient so that the devices perform effectively and are conspicuous with x-ray imaging, respectively. Metal is less than desirable for MR imaging applications as it can cause heating and imaging artefacts. Worst case, the metal component may be ferromagnetic and lead to strong attractive forces. Nonetheless, when selecting devices for passive tracking it is critical to make sure that they do not suffer significantly from these effects.

While a number of vessels have been catheterized with MR guidance, primarily in experimental animals, these experiments have focused on peripheral and cardiovascular applications. One reason that neurovascular applications have not yet been realized is because of the inability to reliably and time-efficiently guide the catheter from the femoral artery through the vessel of the thorax and into the carotid artery and then to the brain. Another reason is that catheters for neurovascular applications are smaller than those used in the peripheral circulation or heart. It is my expectation that navigation into the carotid artery can be achieved in experimental animals using passive catheter tracking if image frame rates can be increased to above 5.2 Hz. This postulate is demonstrated first with an MR compatible flow phantom and then in a series of canines using commercially available x-ray and MR compatible endovascular devices.

## **5.2 Methods**

### ***5.2.1 In Vitro Model***

A flow phantom (described in §4.2.1) of the aortic arch and supra-aortic branch vessels was constructed by submerging a mold (Elastrat Sàrl, Geneva, Switzerland) into a large plastic container containing saline. A variable flow chemical pump (Fisher Scientific, Ottawa, ON) was attached to the phantom and set to pump water at 3 L / min into the ascending aorta during imaging. A vascular introducer catheter was inserted into the side of the flow phantom so that a catheter could be inserted and navigated during imaging.

### ***5.2.2 In Vivo Model***

Ethics approval for the *in vivo* experiments was obtained from the institutional Animal Care Committee. Four canines<sup>1</sup> were used to evaluate the performance of passive MR catheter guidance in the aortic arch during normal physiological motion. The canines were all under 2 years of age and ranged in size from 17 kg to 26 kg. An incision was made to expose the left femoral artery, the vessel was punctured and a catheter introducer was inserted to allow subsequent vascular access for catheters.

The canines were anesthetised with isoflurane (Halocarbon Corp, Beech Island, SC) during the imaging portions of the experiment through a ventilator (Harvard Apparatus, Holliston, MA) at rate of 17 breaths per minute, a stroke volume of 300 cc and inspiration/expiration percent of 50/50. The animal heart rate generally remained at about 100 beats per minute (bpm) during the experiment, and stayed within a range of 80 bpm to 120 bpm.

---

<sup>1</sup> One of these animals was used for the evaluation described in Chapter 4.

### ***5.2.3 Endovascular Devices***

Two devices were selected for use in this study, a 6 F balloon catheter (Centurion, Covington, GA) and a straight tipped 5 F catheter (Cordis, Markham, ON, Canada). These devices were selected from a range of surplus devices as they did not suffer from the heating, magnetic attraction, or imaging artefacts; and they still were visible on x-ray fluoroscopy images. These devices were filled with 0.02 M (4%) gadolinium contrast agent (Magnevist, Berlex Canada Inc, Pointe-Claire, ON, Canada) to give them positive image contrast on  $T_1$ -weighted images.

### ***5.2.4 Magnetic Resonance Catheter Tracking***

Imaging was performed with a 3 T MR scanner (GE Signa VH/i, GE Healthcare, Waukesha, WI). A real time imaging application (described more fully in Chapter Three) was written in C/C++ and executed on a real-time computer (Mac Mini, Mac OS 10.5, 2 GHz Core 2 Duo, 4 GB of RAM). The computer was interfaced using the TCP/IP protocol to the 3 T scanner hardware and data was pushed to the workstation to enable real-time imaging for tracking on the in-room display (Fig 3.1). Image data was collected with a single channel body coil and with a four-channel torso-phased array coil to improve signal to noise ratio (SNR).

When imaging the flow phantom a roadmap scan was collected of the arch. A balanced steady state free precession (bSSFP) sequence was used for the roadmap images as it has a good signal to acquisition time ratio, and can be acquired very quickly (< 0.2 s). The roadmap acquisition matrix size was  $128 \times 128$ , over a field of view (FOV) of 22 cm and a slice thickness of 3.5 mm thick. TE/TR/flip were 1.4 ms/3.0 ms/20°. The

catheter was visualized with a spoiled gradient-recalled echo sequence (SPGR) using a multi-cycle projection dephaser (mcPD) length of 6 mm.(26) The SPGR sequence is inherently  $T_1$ -weighted allowing the catheters to be visualized because of the dilute contrast agent in the catheter lumen. Furthermore, the mcPD sequence suppresses signal from the background tissues/structures, in principal, leaving only signal from the catheter lumen in the image. The SPGR image was positioned and oriented as the roadmap image, but used a 40-mm thick slice to ensure that the entire catheter was imaged in large or tortuous vessels. The mcPD matrix acquisition size was 128 x 128, and the TE/TR/flip were 1.6 ms /3.0 ms/90<sup>0</sup>. Based on the finding of Chapter Four, catheter tracking images were accelerated two-fold using compressed sensing.(24,35,87) This provided a frame rate of 5.2 Hz.

Positioning the roadmap scan on the aortic arch is challenging, particularly when also attempting to image the supra-aortic vessels. The carotid and brachiocephalic trunk of a canine are thinner than that of a human (1-2 cm vs 2-3 cm), making this task more difficult For this reason an axial time of flight (TOF) scan was performed to visualize these vessels for positioning of the tracking and roadmap scans. The time of flight image acquisition had a matrix size of 256 ×256, TE/TR/flip of 1.9 ms/7 ms/20<sup>0</sup>, the slices were 7 mm thick with 3 mm overlap. The same roadmap and tracking protocol used for the *in vitro* portion of the experiment was used for the *in vivo*, however, the FOV was reduced as much as possible to improve the spatial resolution. The FOV ranged between 20 cm and 24 cm, depending on the size of the animal.

### ***5.2.5 Catheter Navigation***

The catheters were guided in both the phantom and canines using the real-time image feedback displayed on the in-room screen. In the *in vitro* model the catheter was moved in and out of the ascending aorta and the branching vessels of the aortic arch. In the canines, the catheter was guided up the descending aorta and into the aortic arch and ascending aorta. The catheter was also guided into the supra-aortic vessels. It is important to note that the canine vasculature is subtly different than human vasculature, as it has only two branching vessels off the aortic arch: the brachiocephalic and the right subclavian arteries. Each of these supra-aortic vessels were targeted for catheterization.

### ***5.2.6 Confirmation of Catheter Placement***

A black blood MR angiography and/or x-ray imaging were used to visualize the placement of the catheters. Black blood imaging was performed with a fast spin echo sequence. TE/TR/flip of 31.7 ms/120 ms/45<sup>0</sup>; the matrix acquisition size was 256 × 256 and the slice thickness was 20 mm. The scan plane was matched with the catheter tracking plane to ensure that the catheter was visualized. In three canines, the animals were then moved into an adjacent room equipped with an x-ray fluoroscopic c-arm. The catheters were filled with iodine contrast agent (Optiray™ 320, Covidien, Hazelwood, MO, USA) and imaged to ensure that the catheters were placed in the targeted vessel.

## **5.3 Results**

### ***5.3.1 In Vitro Imaging***

Six frames used to track the 5 F catheter into brachiocephalic trunk of the anthropomorphic phantom are shown in Fig 5.1. The catheter was reliably navigated into

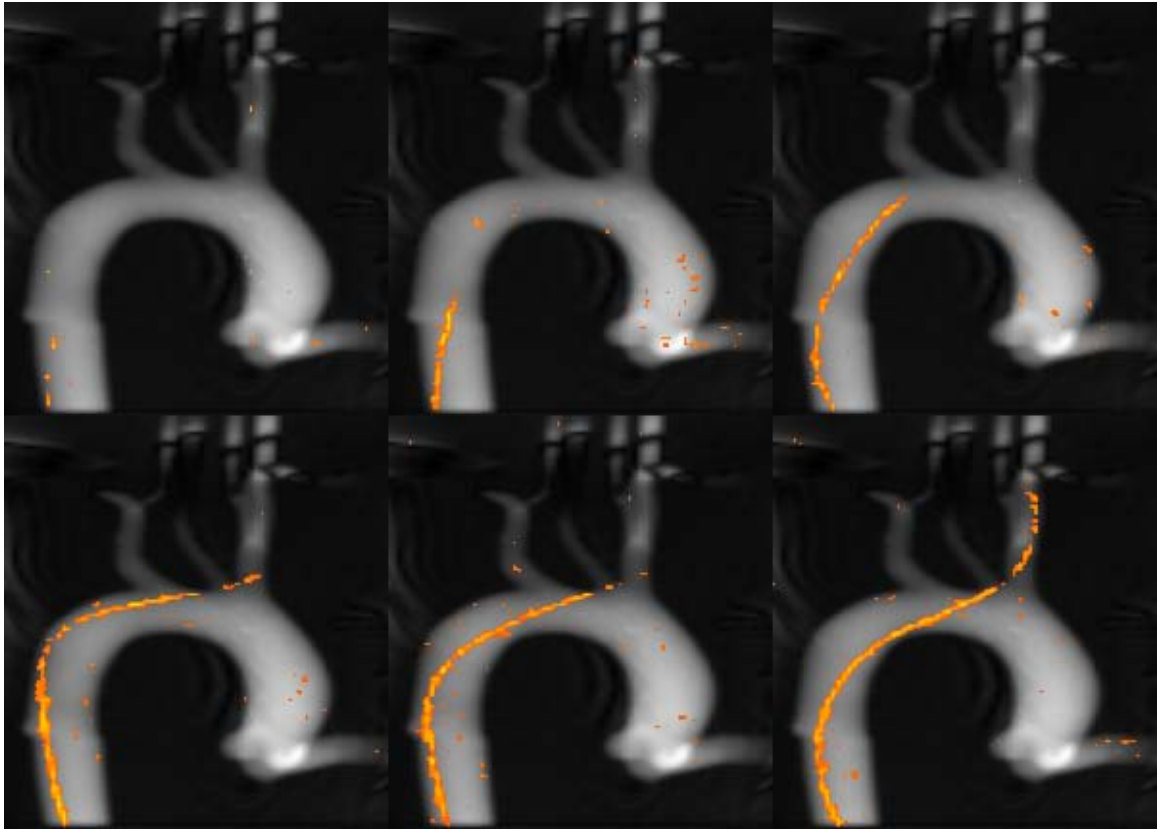


*Figure 5.1: Catheter is being guided into the brachiocephalic trunk. Image frames are acquired at 5.2 Hz.*

the branching vessels. During imaging the catheter could be inserted into the selected vessels within 30 s, however, the time required to reach a target vessel varied significantly depending on the ability of the individual guiding the device.

### ***5.3.2 In Vivo Imaging***

TOF images show moving blood with higher image contrast. This allows placement of the catheter tracking image plane with high reliability. The initial roadmap image is only 3.5 mm thick, and the potential for the image plane to be misaligned with the small (1.5 cm) vessels branching off the aortic arch is high. Examples of the TOF images used for positioning the roadmap image are shown in Fig 5.2. The tracking image plane was

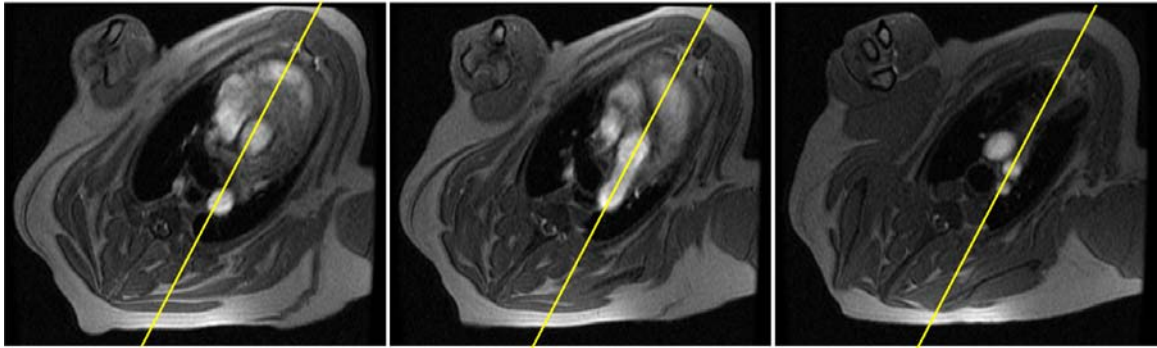


*Figure 5.2: Axial TOF images used for positioning the 2D catheter tracking slice. The yellow line indicates the position of the tracking slice.*

placed correctly in all of the animals. Proper selection of the imaging plane on the TOF localizer images can maximize the spatial difference of the subclavian artery and brachiocephalic trunk. The further the vessels are apart in the tracking image the easier it is to confirm catheter placement with the tracking images.

In all four canines the catheters were successfully navigated into the branching vessels of the aorta. The catheters were guided up the descending aorta and into the ascending aorta and aortic arch. The catheter was also guided into the branching vessels of the aortic arch. An example of the catheter being steered into the ascending aorta is shown in Fig 5.3. The catheter could also be visualized being navigated into the subclavian and brachiocephalic trunk of the canines. Fig 5.4 shows the catheter being guided into both of these vessels.

The catheters were conspicuous in both of the images. Fig 5.3 had a slightly smaller FOV (22 cm) than Fig 5.4 (24 cm), due to the size difference of the two animals. The catheter is less conspicuous in the larger FOV image because the image voxel size is

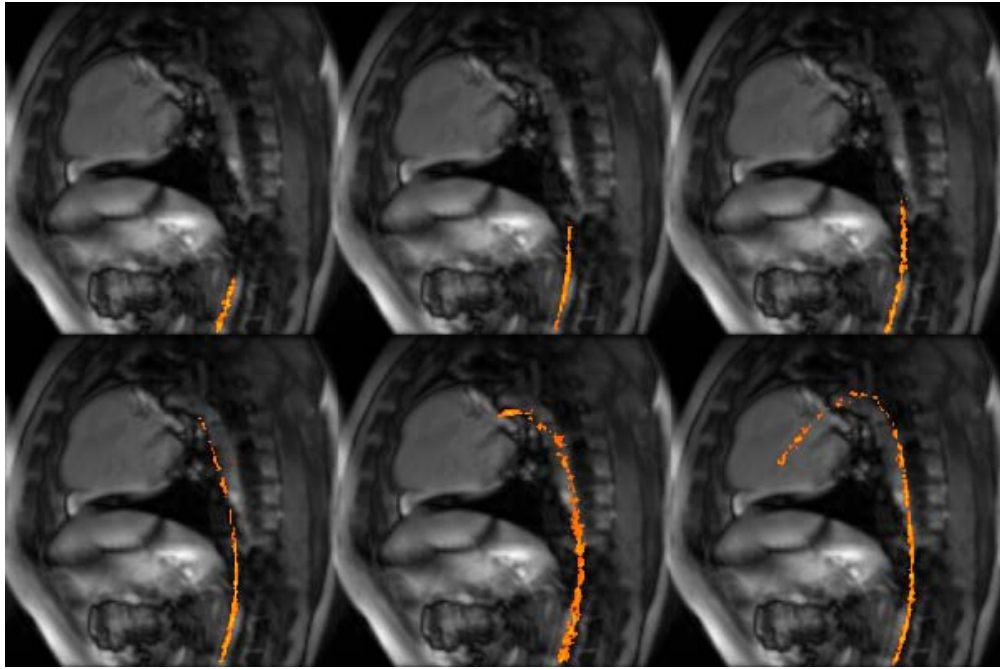


*Figure 5.3:5 F Catheter is being visualized as it is guided into the ascending aorta.*

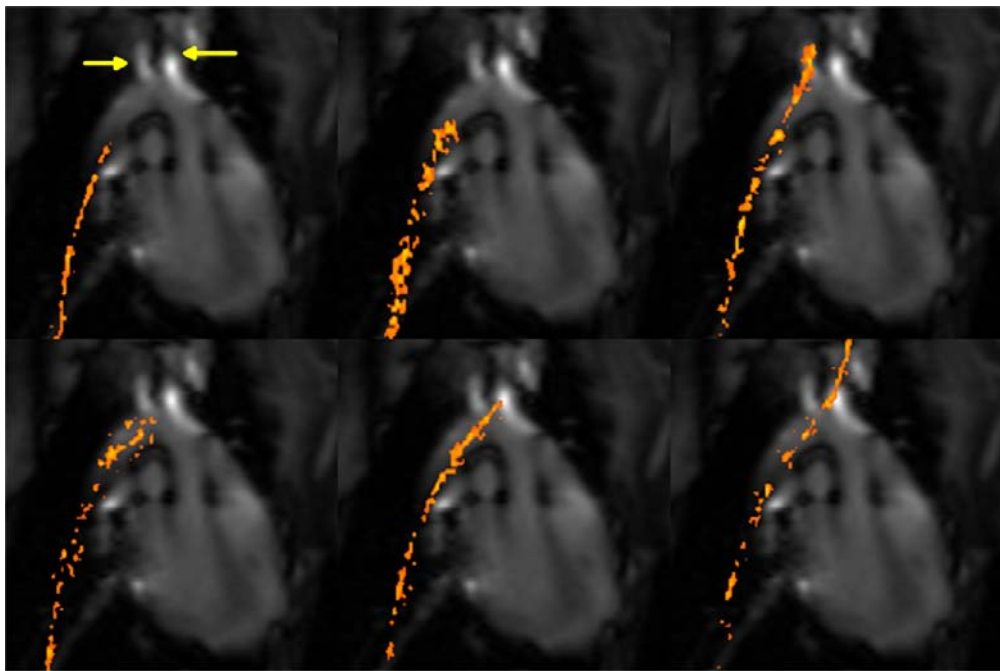


*Figure 5.4: 6 F catheter being guided to the branching vessels of the aortic arch. The left arrow points to the subclavian artery and the right arrow points to the brachiocephalic trunk artery. From the brachiocephalic trunk, the second branching vessel would be the carotid artery in a human.*

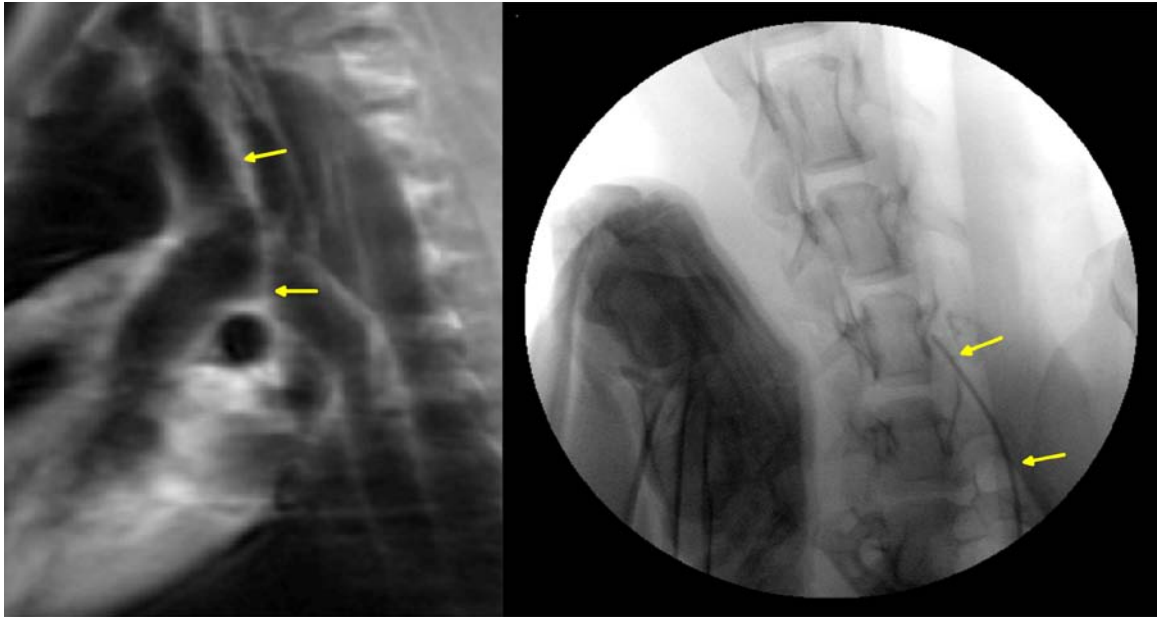


*Figure 5.5: Confirmation of the catheter placement in the brachiocephalic trunk. Left) Black blood image of the aortic arch. Arrows indicates that the catheter is in the brachiocephalic trunk. Right) Catheter is filled with iodine contrast agent and is advanced well beyond the position of the aortic arch.*

smaller. It may be desired in some cases to sacrifice some of the high temporal resolution (5.2 fps) for higher spatial resolution when a large FOV is required.

To confirm placement of the catheter *in vivo*, black blood imaging and x-ray imaging were used. Example confirmation images of the catheter being placed in the brachiocephalic trunk from the navigation in Fig 5.4 is shown in Fig 5.5.

#### **5.4 Discussion**

Active tracking has been demonstrated with frame rates higher than 5.2 Hz, but these experiments have lower spatial resolution and lower TR values, because of the sequences used for device tracking. Passive imaging in this experiment used a modified SPGR sequence to image during tracking. From an SNR perspective, the SPGR sequence is less

temporally efficient than bSSFP or fast gradient recalled echo (FGRE) sequences because of crusher gradients required at the end of each readout line. It is inherently hard to image fast with the mcPD approach.

This chapter demonstrated catheter placement with passive tracking methods to several vessels that are regions of intense physiological motion. Canines have a higher heart rate than humans (§2.1.1) further underscoring this achievement. Previous passive catheter tracking experiments have been limited temporally ( $<1$  Hz), however, acceleration with CS and reducing the spatial resolution and TR, the image frame rate in this experiment was 5.2 Hz. Due to the higher frame rate, the effects of motion that hindered previous experiments was reduced. The catheters were reliably visualized in all of the animals, with in-plane resolution never greater than  $2 \text{ mm} \times 2 \text{ mm}$ . Higher temporal resolutions could be achieved at the expense of spatial resolution, but this in turn makes the image resolution on the order of twice the diameter of the catheter and leads to poor detection and conspicuity.

CS is the desired image acceleration method (§4) for catheter tracking because it does not require coil sensitivity profiles like parallel imaging. During interventions, coils must not move during the procedure (this happened several times with the four-channel torso phased array coil in these experiments). With CS the coil was intentionally and accidentally moved several times during imaging with no reduction in image quality.

The catheter selected had lumens that could be filled with contrast agent to visualize them. While catheters have lumens, not all endovascular devices have hollow lumens, methods for contrast agent coating could make a large number of previously

developed devices compatible with this method of tracking. Guidewires contain metal and special effort is needed to make these MR compatible and MR visible.

For future studies, a comparison of tracking with these parameters and x-ray imaging should be performed with several operators to determine which modality is most effective, or if MR imaging could be considered clinically when an option exists for use with x-ray imaging. Based on the time required to track the devices in this study, MR catheterization can be performed in comparable times to x-ray.

In this chapter we have demonstrated the proof-of-concept of passive catheter tracking near and past the aortic arch. This is an essential step in moving towards MR-guided endovascular therapies in the head and neck. To my knowledge this achievement has yet to be reported in literature. Catheters were also guided selectively into different supra-aortic vessels, and this has yet to be reported with either active or passive catheter tracking strategies. The ability to reliably navigate devices into the carotid arteries is significant, as it provides an avenue for neurovascular interventions with MR imaging that were not previously possible or attempted. MR will likely be an effective tool for neurovascular interventions given the wealth of possibilities for patient monitoring during procedures.

## **Chapter Six: Summary**

This chapter reviews the key successes, failures and limitations of this research project.

The experiments described in Chapters Three to Five have confirmed the general validity of the overall hypothesis of this project. The work has shown that with appropriate accelerated imaging approaches, it is possible for a catheter to be guided from the femoral artery to the carotid artery in a large animal model. The specific objectives of this project were (described in §1.3):

1. Development of a new real-time imaging platform that is capable of displaying images in the scanner bore.
2. Assessment of multiple image acceleration methods to find a method that is desirable for passive catheter tracking by overcoming motion in the thoracic cavity.
3. Demonstrate tracking under MR guidance from the femoral artery to the carotid artery.

The following sections describe the main conclusion and summarize the discussion points resulting from this work, as well as listing recommendations for future work.

### **6.1 Conclusions and Discussion**

In Chapter Three a real time imaging system was successfully developed and integrated with the current MR scanner hardware. The system was tested and shown to be able to reconstruct images in real time (>10 Hz with eight channel phased-array coils) with minimal latency (<100 ms). This achieved the first specific objective of this project.

Chapter Four investigated different methods for accelerating passive catheter tracking images. Compressed sensing (CS) (24,35,87) was found to be the most effective method and should be used for future studies. In Chapter Five, an MR-compatible catheter was successfully guided from the femoral artery to the carotid artery using the imaging system developed in Chapter Three and the CS method was suggested as being the most appropriate acceleration method from Chapter Four. The work in Chapter Five demonstrated proof-of-principle only, since real-time guidance was not possible with CS reconstructed images as the computational capacity of the reconstruction workstation was greatly exceeded. Instead, these data were obtained in real time by using a more conventional zero-padded (ZP) reconstruction (typical latency of <100 ms, image frame rate of 5.4 Hz, 3.3) for the real-time tracking. While not acceptable for human work, the image quality of the real-time reconstructed ZP data still enabled coarse positioning of the catheter under MR guidance. The CS images evaluated were obtained by a subsequent off-line reconstruction; clearly a faster real-time computer would allow integration of CS and real-time imaging.

### ***6.1.1 Specific Objective 1: Real Time MR Imaging***

The real-time system that was developed for Chapter Three met the criterion of the first objective. Catheter tracking images were successfully reconstructed and superimposed onto a previously collected road-map images at 5.4 Hz with <100 ms latency and displayed in the scanner room. This temporal performance is likely adequate for MR-guided endovascular applications, however, the acceleration method used, VARK sampling, did not truly accelerate the image acquisition  $2\times$ .

Some drawbacks and limitations were noted with the implemented system. User friendliness is a clearly a desirable aspect to computer programs and infrastructure. While the current program includes a graphical user interface, one drawback is the difficulty for a novice operator in running the system. Part of this problem is inherent to interconnecting with a commercial, clinical MR scanner. For example, two computers were required to prescribe (MR scanner console computer) and to reconstruct, fuse and display images (real-time computer). The console computer was provided by the equipment vendor and does not easily allow custom programs to be executed locally. It is a Linux operating system tailored for performing the tasks required by the scanner and not for custom image reconstruction. This real-time computer interacted with the run-time scanner hardware and initiated synchronization of the real-time imaging functionality. Raw data that was collected by the scanner run-time hardware was immediately pushed to the real-time computer for display. It was not sent to the scanner console computer and as a result real-time images were not stored in the scanner image database for subsequent analysis or archival.

Only imaging pulse sequences that had been modified to transmit (*i.e.*, push) raw data to the reconstruction workstation could be used. If a new innovative image protocol such as perfusion imaging (for evaluation of stroke thrombolysis) was desired for a real-time procedure, then the pulse sequences would need to be modified in order to be able to transmit raw data. Code specific to the reconstruction would need to be developed and this code would need to be validated for the specific sequence reconstruction.

The system interaction is one way, once images were reconstruction on the real time computer they could not be using on the scanner console computer. Key acquisition parameters (FOV, orientation, acquired frame rate) could not be modified from the reconstruction workstation. From a user standpoint, it is most desirable to avoid using additional real-time computing infrastructure and instead use the vendor supplied infrastructure. This less than optimal approach was taken during the course of the project, however, resulted in demonstration of the concept, albeit with a somewhat limited and not fully interactive real-time system implementation.

Given that the real-time system had limitations, there were indeed advantages to using it. For conventional acquisitions, the reconstruction workstation can be any consumer-based computer. A Mac mini™ computer running with Mac OS X 10.5 was chosen because of the existence of a large number of software development platforms that were both available and free. Source code was also available for this system. The platform had a friendly development environment. Algorithms and unit tests could be written on one of several workstations and then implemented on the real time workstation, which created a better environment for multiple developers.

Appropriate testing was key to developing and advancing the experiments performed after Chapter Three. Since dual pipelines for image reconstruction, one in Matlab and one in C/C++, were available, algorithms were rapidly implemented compared to my previous experiences. Errors and code defects were easily found because they almost always happen in only one processing pipeline. If the images from each pipeline were not the same, the location in the code where the defect originated could be

easily and quickly pinpointed and then corrected. It may seem that maintaining two processing pipelines in different coding languages would be redundant, but like in the Circle of Willis (described in §2.1.1), redundancy can be beneficial (and at times, prevents a programmer from having a severe “stroke”!)

Specifics of the software program implementation can easily be criticized, and the real-time computer and software is no exception. The developed and validated infrastructure, however, met the requirements of the specific objective and is thus justified in terms of progressing to specific objective two. The developed real-time system formed the basis of testing in Chapters Four and Five.

### ***6.1.2 Specific Objective 2: Fast Imaging methods***

In Chapter Four a comparison was performed between several MR imaging acceleration techniques to see which one was the most effective at accelerating the catheter tracking multi-cycle projection dephaser (mcPD) (26) images. Three parallel imaging algorithms: Simultaneous Acquisition of Spatial Harmonics (SMASH), Sensitivity Encoding (SENSE) and Generalized Autocalibrating Partially Parallel Acquisitions (GRAPPA) and compressed sensing (CS) were compared in this portion of the study. Both quantitative and qualitative aspects were assessed and it was found that CS was the most desirable catheter technique. The major drawback, however, with CS is that it is an iterative technique. The resulting significant increase in computational requirements, which was  $>30\times$  longer than the equivalent ZP image reconstruction, prevented true real-time image acquisition, reconstruction and display.

Other methods for accelerating MR images exist, such as the (Partially Parallel Imaging with Localized Sensitivities) (PILS) method (33) discussed in §2.5.2. The PILS reconstruction method is highly sensitive to imaging coil profiles and typically requires rigid imaging coils. In Chapter Four a flexible phase-array coil was used, thus, the PILS technique was not compared. The specific coil spatial configuration used, for parallel imaging (PI) is an important parameter. Increasing the number and arrangement of coil elements has been shown to greatly change the performance of each of the PI methods. The four-channel torso phase-array coil (General Electric Healthcare, Waukesha, WI) used in this experiment is compatible with parallel imaging. Nonetheless, it is a fair argument that a different coil configuration could enhance one of the PI methods.

There are several variations on the SENSE, SMASH and GRAPPA techniques as these represent relatively mature algorithms. They were developed <10 years ago and are now all commercial available from various vendors. In contrast, CS is still in its infancy. While there are already variations of CS, it remains to be seen which are the best alternatives and if CS will become a widely accepted commercial product. Nonetheless, three of the most popular and widely used PI methods and an emerging non-linear method were assessed in Chapter Four. All were found to increase the image frame rate and met specific objective 2. CS was found to have the best image quality for tracking and was evaluated in Chapter Five.

### ***6.1.3 Specific Objective 3: MR Catheter Tracking***

The work in Chapter Five succeeded in demonstrating key aspects of specific objective 3; reliable guidance of the catheter from the femoral artery into the carotid artery, through

areas of cardiac and respiratory motion, was achieved in canines. The imaging system, described in Chapter Three, and the best method for tracking image acceleration, determined in Chapter Four, were used for this portion of the experiment.

While a moderately successful demonstration of specific objective 3, some limitations existed in these experiments. Ideally, the overall time required from when the animal was anesthetised to the time the catheter reached the target vessels should have been collected and reported. These times are a crucial performance metric required in acute treatments and would provide a point of comparison to x-ray-based approaches. Currently, and as was already described in §6.1.1, the infrastructure required to perform MR-based interventions is exploratory, and not designed for rapid procedures, (*i.e.*, the animal is first stabilized in an adjacent room, and then moved into the scanner room, stabilized again, and then imaging is undertaken.) If the rooms were dedicated for this type of intervention then proper MR-compatible instruments could be used for the intervention. It should be expected that optimizing the environment for this type of procedure would make it faster. This study was intended to demonstrate that it could be done, not show how fast it could be done.

The essential portion of specific objective 3 was completed in spite of the current reconstruction workstation hardware and software not allowing for a real-time implementation of CS acceleration methods. This topic and other recommendations for future work in MR-based endovascular interventions are discussed next.

## **6.2 Suggestions for Future MR-Based Endovascular Investigations**

Throughout the course of this project I have given thought to future tasks. Due to a number of factors, including time constraints, financial concerns, ethical issues, and unavailability of appropriate technologies, these ideas were not realized during this phase of the project. They, however, form a useful discussion for future experiments.

### ***6.2.1 Scanner Hardware Infrastructure***

An obvious suggestion is for the MR scanner to have better access for interventional procedures. Other research groups have used newer, wider ( $\geq 60$  cm) and shorter (70 cm from the front cover to the imaging centre) bore MR scanners. These scanners facilitate MR imaging and are nearly half as long as the current long-bore scanner (55 cm wide bore and 110 cm from front cover to the imaging centre) used for these studies.<sup>2</sup> The current long-bore scanner requires the interventionalist to climb into the bore and view a display screen located on the other side of the subject. This orientation is not acceptable for clinical evaluation. With a shorter MR scanner, the interventionalist would be able to stand and view a screen on the other side of the scanner table during procedures. For routine procedures this would be greatly desired.

Increasing the number of imaging channels has been shown to increase the performance of several acceleration techniques and improve the SNR of imaging. Experiments with 128-channel receiver coils have been demonstrated to improve imaging of areas of motion.<sup>(120)</sup> These experiments were limited to eight-channel coils

---

<sup>2</sup> Of relevance, the Seaman Family Centre is in the process of replacing the current 3 T scanner with a short bore scanner. The new scanner will be installed in late 2010 and have a  $\geq 60$  cm bore diameter and be  $< 70$  cm from front cover to iso-centre. It will also have 32 receive channels.

(maximum number of channels on our current system), but were usually conducted with a four-channel coil. The ability to configure coils for customized interventional imaging would be greatly desired so that the coils could be optimized for different imaging circumstances. Coils that were compatible with PILS might also be beneficial.

The ability to configure the imaging coils would open other possibilities as well, such as the ability to perform active tracking. Reports of active tracking application exceed those of passive tracking. Although there are some desirable characteristics of passive tracking, active tracking will most likely be incorporated into vendor supplied endovascular imaging suites of the future. Exploring methods for incorporating passive and active tracking may be an interesting avenue for future investigation.

The potential for an all-in-one imaging platform would indeed be useful for improving the work flow of MR-based endovascular procedures. This could be done in one of two ways: 1) the vendors could supply an interface that allowed for programming of real time applications (supply a complete system), or 2) the console computer could be replaced with a consumer computer if it could execute the required functions to operate the scanner. Either approach is challenging and would require direct interaction with the scanner manufacturer.

Robotics could be an interesting advancement for MR-based endovascular applications. Remote catheter manipulators have been developed for x-ray applications and could be redesigned for MR procedures. This would require using pneumatics or piezoelectric motors. Using robots would be desirable because the interventionalist would

not have to be in/near the magnet, precise manipulation of the devices could be performed and feedback could be incorporated.

Intervention MR imaging is a growing field and the methods being used are constantly changing. It is likely that suggestions in this section will reach maturity in the future as they are intuitive directions for the field.

### ***6.2.2 Motion Phantoms***

The phantoms used in this study were static, and although they did simulate flow, they did not simulate the physiological motion of the heart and lungs. There are few motion phantoms reported in the MR literature and all are tailored to a specific application other than cardiovascular interventions. One promising anthropomorphic phantom was commercialized this year by Philips, it is a heart phantom driven by pneumatics. This phantom is solely a heart and can not however be used for training in and validating MR catheter guiding. A closed-loop whole body circulation phantom would be strongly desired for future experiments as it would help to limit the number of animals used. It is surprising that an anthropomorphic motion/circulation phantom is not commercially available. A thoracic motion phantom, suitable for replacing animals in some initial endovascular MR evaluation experiments, is currently under development at the MR Centre.

### ***6.2.3 Animal Experiments***

Canines were used in the experiments of this thesis as they are a robust model. Lines are easily inserted into canines. There are however several disadvantages to using canines with respect to these interventions. Canines vascular system differs from that of humans,



*Figure 6.1: Composite braids that are used in the manufacturing of catheters. These devices were made in a research lab and are not yet commercially available. Figure taken from ref (123).*

particularly near the heart. There are only two branching vessels off the top of the aortic arch, and these vessels lie in a separate plane from the arch and descending aorta, hence the imaging plane can not easily be placed such that these vessels are in the same plane as the ‘candy cane’ of the aorta arch and descending aorta. I would suggest that swine would be a more appropriate model, and closer to the human vasculature.

#### ***6.2.4 Composite Braided Endovascular Devices***

Another avenue for investigation will be composite braided devices. Many of the devices used with x-ray imaging are braided with metal, as this provides the desired mechanical properties and attenuation coefficient required. Metal braided devices can cause distortion of MR images and heating, and therefore is undesired. Composite braids such as the ones show in Fig 6.1 would be suitable for MR application.

## References

1. Schermerhorn M, O'Malley A, Jhaveri A, Cotterill P, Pomposelli F, Landon B. Endovascular vs. Open Repair of Abdominal Aortic Aneurysms in the Medicare Population. *The New England Journal of Medicine* 2008(358):464-474.
2. Mas J, Trinquart L, Leys D, Albucher J, Rousseau H, Viguier A, Bossavy J, Denis B, Piquet P, Garnier P, Viader F, Touzé E, Julia P, Giroud M, Krause D, Hosseini H, Becquemin J, Hinzelin G, Houdart E, Hénon H, Neau J, Bracard S, Onnient Y, Padovani R, Chatellier G. Endarterectomy Versus Angioplasty in Patients with Symptomatic Severe Carotid Stenosis (EVA-3S) Trial: results up to 4 years from a randomised, multicentre trial. *Lancet Neurology* 2008;7:885-892.
3. Kastrup A, Groschel K, Krapf H, Brehm B, Dichgans J, Schulz J. Early Outcome of Carotid Angioplasty and Stenting With and Without Cerebral Protection Devices. *Stroke* 2003;34:813-819.
4. Nair G, Nery P, Diwakaramenon S, Healey J, Connolly S, Morillo C. A Systematic Review of Randomized Trials Comparing Radiofrequency Ablation with Antiarrhythmic Medications in Patients with Atrial Fibrillation. *Journal of Cardiovascular Electrophysiology* 2009;20(2):138-144.
5. O'Neill MD, Jais P, Hocini M, Sacher F, Klein GJ, Clementy J, Haissaguerre M. Catheter Ablation for Atrial Fibrillation. *Circulation* 2007;116(13):1515-1523.
6. Stern A, Tunick PA, Culliford AT, Lachmann J, Baumann FG, Kanchuger MS, Marschall K, Shah A, Grossi E, Kronzon I. Protruding Aortic Arch Atheromas:

- Risk of Stroke During Heart Surgery With and Without Aortic Arch  
Endarterectomy. *American Heart Journal* 1999;138(4):746-752.
7. Pierre Gobin Y, Starkman S, Duckwiler GR, Grobelny T, Kidwell CS, Jahan R, Pile-Spellman J, Segal A, Vinuela F, Saver JL. MERCI 1: A Phase 1 Study of Mechanical Embolus Removal in Cerebral Ischemia. *Stroke* 2004;35(12):2848-2854.
  8. Bose A, Henkes H, Alfke K, Reith W, Mayer TE, Berlis A, Branca V, Sit SP. The Penumbra System: A Mechanical Device for the Treatment of Acute Stroke due to Thromboembolism. *AJNR Am J Neuroradiol* 2008;29(7):1409-1413.
  9. Fahlbusch R, Nimsky C, Huk W. Open Surgery of Giant Paraclinoid Aneurysms Improved by Intraoperative Angiography and Endovascular Retrograde Suction Decompression. *Acta Neurochirurgica* 1997;139(11):1026-1032.
  10. Pile-Spellman J, Lei F; Endovascular Brush. United States. 2006.
  11. Heuser R, Biamino C, Krajcer Z, Dougherty K. Endovascular Equipment and Interventional Tools. *Peripheral Vascular Stenting: Taylor and Francis; 2005.*
  12. Carpenter JP, Fairman RM, Barker CF, Golden MA, C. Velazquez O, Mitchell ME, Baum RA. Endovascular AAA Repair in Patients with Renal Insufficiency: Strategies for Reducing Adverse Renal Events. *Cardiovascular Surgery* 2001;9(6):559-564.
  13. Klein LW, Miller DL, Balter S, Laskey W, Haines D, Norbash A, Mauro MA, Goldstein JA. Occupational Health Hazards in the Interventional Laboratory: Time for a Safer Environment. *Radiology* 2009;250(2):538-544.

14. den Boer A, de Feyter P, Hummel W, Keane D, Roelandt J. Reduction of Radiation Exposure While Maintaining High-Quality Fluoroscopic Images During Interventional Cardiology using Novel X-ray Tube Technology with Extra Beam Filtering. *Circulation* 1994;89(6):2710-2714.
15. Nissen S, Gurley J, Grines C, Booth D, McClure R, Berk M, Fischer C, DeMaria A. Intravascular Ultrasound Assessment of Lumen Size and Wall Morphology in Normal Subjects and Patients with Coronary Artery Disease. *Circulation* 1991;84(3):1087-1099.
16. Tobis J, Mallery J, Mahon D, Lehmann K, Zalesky P, Griffith J, Gessert J, Moriuchi M, McRae M, Dwyer M. Intravascular Ultrasound Imaging of Human Coronary Arteries In Vivo. Analysis of Tissue Characterizations with Comparison to In Vitro Histological Specimens. *Circulation* 1991;83(3):913-926.
17. Sousa JE, Costa MA, Abizaid A, Abizaid AS, Feres F, Pinto IMF, Seixas AC, Staico R, Mattos LA, Sousa AGMR, Falotico R, Jaeger J, Popma JJ, Serruys PW. Lack of Neointimal Proliferation After Implantation of Sirolimus-Coated Stents in Human Coronary Arteries: A Quantitative Coronary Angiography and Three-Dimensional Intravascular Ultrasound Study. *Circulation* 2000.
18. Glowinski A, Adam G, Bucker A, Neuerburg J, Vaals Jv, Gunther R. Catheter Visualization Using Locally Induced, Actively Controlled Field Inhomogeneities. *Magnetic Resonance in Medicine* 1997;38:253-258.

19. Ladd M, Zirnnermann G, Quick H, Debatin J, Boesiger P, Schulthess Gv, McKinnon G. Active MR Visualization of a Vascular Guidewire In Vivo. *Journal of Magnetic Resonance Imaging* 1998;8:220-225.
20. Araki T, Aoki S, Ishigame K, Kumagai H, Nanbu A, Hori M, Ueki J, Komiyama T, Araki T. MR-guided Intravascular Catheter Manipulation: Feasibility of Both Active and Passive Tracking in Experimental Study and Initial Clinical Applications. *Radiation Medicine* 2002;20(1):1-8.
21. Quick H, Kuehl H, Kaiser G, Hornscheidt D, Mikolajczyk K, Aker S, Debatin J, Ladd M. Interventional MRA Using Actively Visualized Catheters, TrueFISP, and Real-Time Image Fusion. *Magnetic Resonance in Medicine* 2003;49:129-137.
22. Quick H, Zenge M, Kuehl H, Kaiser G, Aker S, Massing S, Bosk S, Ladd M. Interventional Magnetic Resonance Angiography with No Strings Attached: Wireless Active Catheter Visualization. *Magnetic Resonance in Medicine* 2005;53:446-455.
23. Kocaturk O, Kim AH, Saikus CE, Guttman MA, Faranesh AZ, Ozturk C, Lederman RJ. Active Two-Channel 0.035' Guidewire for Interventional Cardiovascular MRI. *Journal of Magnetic Resonance Imaging* 2009;30(2):461-465.
24. Schirra CO, Weiss S, Krueger S, Pedersen SF, Razavi R, Schaeffter T, Kozerke S. Toward True 3D visualization of Active Catheters using Compressed Sensing. *Magnetic Resonance in Medicine* 2009;62(2):341-347.

25. Jiang X, Yu H, Frayne R, Unal O, Strother CM. Novel Magnetic Resonance Signal Enhancing Coating Material. *Advanced Materials* 2001;13(7):490-493.
26. Draper J, Lauzon M, Frayne R. Passive Catheter Visualization in Magnetic Resonance–Guided Endovascular Therapy Using Multicycle Projection Dephasers. *Journal of Magnetic Resonance Imaging* 2006;24:160–167.
27. Susil RC, Camphausen K, Choyke P, McVeigh ER, Gustafson GS, Ning H, Miller RW, Atalar E, Coleman CN, Ménard C. System for Prostate Brachytherapy and Biopsy in a Standard 1.5 T MRI Scanner. *Magnetic Resonance in Medicine* 2004;52(3):683-687.
28. Saeed M, Saloner D, Weber O, Martin A, Henk C, Higgins C. MRI in Guiding and Assessing Intramyocardial Therapy. *European Radiology* 2005;15(5):851-863.
29. Chen X, Lehman CD, Dee KE. MRI-Guided Breast Biopsy: Clinical Experience with 14-Gauge Stainless Steel Core Biopsy Needle. *Am J Roentgenol* 2004;182(4):1075-1080.
30. Alterovitz R, Branicky M, Goldberg K. Motion Planning Under Uncertainty for Image-Guided Medical Needle Steering. *The International Journal of Robotics Research* 2008;27(11-12):1361-1374.
31. Sodickson D; Simultaneous Acquisition of Spatial Harmonics (SMASH): Ultra-Fast Imaging with Radiofrequency Coil Arrays. 1999.

32. Griswold MA, Jakob PM, Heidemann RM, Nittka M, Jellus V, Wang J, Kiefer B, Haase A. Generalized Autocalibrating Partially Parallel Acquisitions (GRAPPA). *Magnetic Resonance in Medicine* 2002;47(6):1202-1210.
33. Griswold MA, Jakob PM, Nittka M, Goldfarb JW, Haase A. Partially Parallel Imaging with Localized Sensitivities (PILS). *Magnetic Resonance in Medicine* 2000;44(4):602-609.
34. Pruessmann K, Weiger M, Scheidegger M, Boesiger P. SENSE: Sensitivity Encoding for Fast MRI. *Magnetic Resonance in Medicine* 1999;42:952-962.
35. Lustig M, Donoho D, Pauly JM. Sparse MRI: The Application of Compressed Sensing for Rapid MR Imaging. *Magnetic Resonance in Medicine* 2007;58(6):1182-1195.
36. Kyriakos W, Panych L, Kacher D, Westin C, Bao S, Mulkern R, Jolesz F. Sensitivity Profiles From an Array of Coils for Encoding and Reconstruction in Parallel (SPACE RIP). *Magnetic Resonance in Medicine* 2000;44:301-308.
37. Earls J, Ho V, Foo T, Castillo E, Flamm S. Cardiac MRI: Recent Progress and Continued Challenges. *Journal of Magnetic Resonance Imaging* 2002;16:111-127.
38. Ramos-Cabrer P, van Duynhoven JPM, Van der Toorn A, Nicolay K. MRI of Hip Prostheses using Single-Point Methods: in vitro studies towards the artifact-free imaging of individuals with metal implants. *Magnetic Resonance Imaging* 2004;22(8):1097-1103.

39. Frayne R, Goodyear BG, Dickhoff P, Lauzon ML, Sevick RJ. Magnetic Resonance Imaging at 3.0 Tesla: Challenges and Advantages in Clinical Neurological Imaging. *Investigative Radiology* 2003;38(7):385-402.
40. Unal O, Korosec F, Frayne R, Strother C, Mistretta C. A Rapid 2D Time-Resolved Variable-Rate k-space Sampling MR Technique for Passive Catheter Tracking During Endovascular Procedures. *Magnetic Resonance in Medicine* 1998;40:356-362.
41. Omary RA, Frayne R, Unal O, Warner T, Korosec FR, Mistretta CA, Strother CM, Grist TM. MR-guided Angioplasty of Renal Artery Stenosis in a Pig Model: A Feasibility Study. *Journal of Vascular and Interventional Radiology* 2000;11(3):373-381.
42. Peters DC, Lederman RJ, Dick AJ, Raman VK, Guttman MA, Derbyshire JA, McVeigh ER. Undersampled Projection Reconstruction for Active Catheter Imaging with Adaptable Temporal Resolution and Catheter-Only Views. *Magnetic Resonance in Medicine* 2003;49(2):216-222.
43. Köchli VD, McKinnon GC, Hofmann E, Schulthess GKv. Vascular Interventions Guided by Ultrafast MR Imaging: evaluation of different materials. *Magnetic Resonance in Medicine* 1994;31(3):309-314.
44. Chen H. Roadmapping for Endovascular Interventions: University of Calgary; 2009.
45. MacDonald ME, Stafford RB, Frayne R. Real Time Magnetic Resonance Imaging for Angioplasty 2009; Victoria, BC, Canada. p 84-88.

46. MacDonald ME, Stafford RB, Lauzon ML, Frayne R,. One Step Real-Time Image Correction with GUSTO (Gradient-warp and UnderSampling Transform Operator). 2010; Stockholm, Sweden, 1-7 May 2010.
47. Goyen M, Quick HH, Debatin JrF, Ladd ME, Barkhausen Jr, Herborn CU, Bosk S, Kuehl H, Schleptz M, Ruehm SG. Whole-Body Three-dimensional MR Angiography with a Rolling Table Platform: initial clinical experience. *Radiology* 2002;224(1):270-277.
48. Access Excellence Classic Collection, <http://www.accessexcellence.org>.
49. Marshall I, Papathanasopoulou P, Wartolowska K. Carotid Flow Rates and Flow Division at the Bifurcation in Healthy Volunteers. *Physiological Measurement* 2004;25:691-697.
50. Wolpert S. The Circle of Willis. *AJNR Am J Neuroradiol* 1997;18(6):1033-1034.
51. Ishihara K, Zile MR, Tomita M, Tanaka R, Kanazawa S, Carabello BA. Left Ventricular Hypertrophy in a Canine Model of Reversible Pressure Overload. *Cardiovascular Research* 1992;26(6):580-585.
52. Miller M. *Guide to the Dissection of the Dog*. New York: Ithaca; 1947.
53. Ghalichi F, Deng X, Champlain AD, Douville Y, King M, Guidoin R. Low Reynolds Number Turbulence Modeling of Blood Flow in Arterial Stenoses. *Biorheology*;35(4-5):281-294.
54. Ku D, Giddens D. Pulsatile flow in a model carotid bifurcation. *Arteriosclerosis, Thrombosis, and Vascular Biology*; 1983;3(1):31-39.

55. Stein P, Sabbah H. Turbulent Blood Flow in the Ascending Aorta of Humans with Normal and Diseased Aortic Valves. *Circ Res* 1976;39(1):58-65.
56. Stein P, Sabbah H. Measured Turbulence and Its Effect on Thrombus Formation. *Circ Res* 1974;35(4):608-614.
57. Swieten JC, Hout J, Ketel B, Hijdra A, Wokke JHJ, Gijn JV. Periventricular Lesions in the White Matter on Magnetic Resonance Imaging in the Elderly: A Morphometric Correlation with Arteriolosclerosis and Dilated Perivascular Spaces. *Brain* 1991;114(2):761-774.
58. Sacco RL AR, Albers G, Alberts MJ, Benavente O, Furie K, Goldstein LB, Gorelick P, Halperin J, Harbaugh R, Johnston SC, Katzan I, Kelly-Hayes M, Kenton EJ, Marks M, Schwamm LH, Tomsic T. Guidelines for Prevention of Stroke in Patients with Ischemic Stroke or Transient Ischemic Attack. *Stroke* 2006;37:577-617.
59. Ferguson GG, Eliasziw M, Barr HWK, Clagett GP, Barnes RW, Wallace MC, Taylor DW, Haynes RB, Finan JW, Hachinski VC, Barnett HJM. The North American Symptomatic Carotid Endarterectomy Trial : surgical results in 1415 patients. *Stroke* 1999;30(9):1751-1758.
60. Barnett H, Taylor W, Eliasziw M, Fox A, Ferguson G, Haynes R, Rankin R, Clagett G, Hachinski V, Sackett D, Thorpe K, Meldrum H. Benefit of Carotid Endarterectomy in Patients with Symptomatic Moderate or Severe Stenosis. *New England Journal of Medicine* 1998;339:1415-1425.

61. Vascular and Interventional Radiology: Peripheral Vascular Disease  
<http://www.virchicago.com/peripheral-artery-disease.htm>.
62. British Broadcasting Corp. (BBC):Coil can cut aneurysm death risk  
<http://news.bbc.co.uk/2/hi/health/4205924.stm>.
63. Brilstra EH, Rinkel GJE, van der Graaf Y, van Rooij WJJ, Algra A. Treatment of Intracranial Aneurysms by Embolization with Coils : A Systematic Review. *Stroke* 1999;30(2):470-476.
64. Dowsett D, Kenny P, Johnston R. *The Physics of Diagnostic Imaging (Second Edition)*: Hodder Arnold; 2006.
65. Geise R. Fluoroscopy: Recording of Fluoroscopic Images and Automatic Exposure Control. *RadioGraphics* 2001;21:227-236.
66. Anxionnat R, Bracard S, Ducrocq X, Troussset Y, Launay L, Kerrien E, Braun M, Vaillant R, Scomazzoni F, Lebedinsky A, Picard L. Intracranial Aneurysms: Clinical Value of 3D Digital Subtraction Angiography in the Therapeutic Decision and Endovascular Treatment. *Radiology* 2001;218(3):799-808.
67. Fahrig R, Fox A, Lownie S, Holdsworth D. Use of a C-arm System to Generate True Three-Dimensional Computed Rotational Angiograms: preliminary in vitro and in vivo results. *AJNR Am J Neuroradiol* 1997;18(8):1507-1514.
68. Narra VR, Howell RW, Harapanhalli RS, Sastry KSR, Rao DV. Radiotoxicity of Some Iodine-123, Iodine-125 and Iodine-131-Labeled Compounds in Mouse Testes: Implications for Radiopharmaceutical Design. *Journal of Nuclear Medicine* 1992;33(12):2196-2201.

69. Nyman U, Elmstal B, Leander P, Nilsson M, Golman K, Alman T. Are Gadolinium-Based Contrast Media Really Safer than Iodinated Media for Digital Subtraction Angiography in Patients with Azotemia. *Radiology* 2002;223(2):311-318.
70. de González AB, Darby S. Risk of Cancer from Diagnostic X-rays: estimates for the UK and 14 other countries. *The Lancet* 2004;363(9406):345-351.
71. Cerutti PA. Effects of Ionizing Radiation on Mammalian Cells. *Naturwissenschaften* 1974;61(2):51-59.
72. Calkins H, Niklason L, Sousa J, el-Atassi R, Langberg J, Morady F. Radiation Exposure During Radiofrequency Catheter Ablation of Accessory atrioventricular connections. *Circulation* 1991;84(6):2376-2382.
73. Wagner L, Eifel P, Geise R. Effects of Ionizing Radiation. *Journal of Vascular and Interventional Radiology* 1995;6(6):988-989.
74. Niklason LT, Marx MV, Chan HP. Interventional Radiologists: occupational radiation doses and risks. *Radiology* 1993;187(3):729-733.
75. Vano E, Gonzalez L, Guibelalde E, Fernandez J, Ten J. Radiation Exposure to Medical Staff in Interventional and Cardiac Radiology. *The British Journal of Radiology* 1998;71(849):954-960.
76. Thakur Y, Bax JS, Holdsworth DW, Drangova M. Design and Performance Evaluation of a Remote Catheter Navigation System. *Biomedical Engineering, IEEE Transactions on* 2009;56(7):1901-1908.

77. Ellis KJ. Human Body Composition: In Vivo Methods. *Physiological Reviews* 2000;80(2):649-680.
78. University C. EMRIC - MRI Basics  
<http://www.cardiff.ac.uk/biosi/researchsites/emric/basics.html>.
79. Stafford RB, Lauzon ML, Sabati M, Frayne R, Thompson RI. A Tutorial on the Precessional Behaviour of Hydrogen Nuclei in External Magnetic Fields. *Canadian Journal of Physics* 2010;7(88):465-477.
80. Beta K. A unit of knowledge. <http://knol.google.com/k/functional-magnetic-resonance-imaging#>.
81. Harris F. On the Use of Windows for Harmonic Analysis with the Discrete Fourier Transform. *Proceedings of the IEEE* 1978;66(1):51-83.
82. Atalar E, Bottomley PA, Ocali O, Correia LCL, Kelemen MD, Lima JAC, Zerhouni EA. High Resolution Intravascular MRI and MRS by using a Catheter Receiver Coil. *Magnetic Resonance in Medicine* 1996;36(4):596-605.
83. Bock M, Müller S, Zuehlsdorff S, Speier P, Fink C, Hallscheidt P, Umathum R, Semmler W. Active Catheter Tracking using Parallel MRI and real-time image reconstruction. *Magnetic Resonance in Medicine* 2006;55(6):1454-1459.
84. Fink C, Bock M, Umathum R, Volz S, Zuehlsdorff S, Grobholz R, Kauczor H, Hallscheidt P. Renal Embolization: Feasibility of Magnetic Resonance-Guidance Using Active Catheter Tracking and Intraarterial Magnetic Resonance Angiography. *Investigative Radiology* 2004;39:111-119.

85. Omary RA, Green JD, Schirf BE, Li Y, Finn JP, Li D. Real-Time Magnetic Resonance Imaging-Guided Coronary Catheterization in Swine. *Circulation* 2003;107(21):2656-2659.
86. Unal O, Li J, Cheng W, Yu H, Strother CM. MR-Visible Coatings for Endovascular Device Visualization. *Journal of Magnetic Resonance Imaging* 2006;23(5):763-769.
87. Yerly J, Lauzon ML, Chen HS, Frayne R. A Simulation-Based Analysis of the Potential of Compressed Sensing for Accelerating Passive MR Catheter Visualization in Endovascular Therapy. *Magnetic Resonance in Medicine* 2010;63(2):473-483.
88. Bakker C, Bos C, Weinmann H. Passive Tracking of Catheters and Guidewires by Contrast-Enhanced MR Fluoroscopy. *Magnetic Resonance in Medicine* 2001;45:17-23.
89. Ladd M, Erhart P, Debatin J, Hofmann E, Boesiger P, Schulthess Gv, McKinnon G. Guidewire Antennas for MR Fluoroscopy. *Magnetic Resonance in Medicine* 1997;37:891-897.
90. Wacker F, Reither K, Branding G, Wendt M, Wolf K. Magnetic Resonance-Guided Vascular Catheterization: feasibility using a passive tracking technique at 0.2 T in a pig model. *Journal of Magnetic Resonance Imaging* 1999;10:841-844.
91. Frayne R, Strother C, Unal O, Yang Z, Wehelie A, Yu H; MR-Signal-Emitting Coatings. United States. 2002 Nov. 28, 2002.

92. Green J, Omary R, Finn J, Tang R, Li Y, Carr J, Li D. Passive Catheter Tracking Using MRI: Comparison of Conventional and Magnetization-Prepared FLASH. *Journal of Magnetic Resonance Imaging* 2002;16:104-109.
93. Bakker CJ, Hoogeveen RM, Hurtak WF, van Vaals JJ, Viergever MA, Mali WP. MR-Guided Endovascular Interventions: susceptibility-based catheter and near-real-time imaging technique. *Radiology* 1997;202(1):273-276.
94. Paetzel C, Zorger N, Bachthaler M, Hamer OW, Stehr A, Feuerbach S, Lenhart M, VÁ¶lk M, Herold T, Kasprzak P, Nitz WR. Magnetic Resonance-Guided Percutaneous Angioplasty of Femoral and Popliteal Artery Stenoses Using Real-Time Imaging and Intra-arterial Contrast-Enhanced Magnetic Resonance Angiography. *Investigative Radiology* 2005;40(5):257-262.
95. US Department of Health and Human Services FaDA. Guidance for the Submission of Premarket Notifications for Magnetic Resonance Diagnostic Devices; 1998.
96. Korosec FR, Frayne R, Grist TM, Mistretta CA. Time-resolved contrast-enhanced 3D MR angiography. *Magnetic Resonance in Medicine* 1996;36(3):345-351.
97. Kahana A, Lucarelli MJ, Grayev AM, Van Buren JJ, Burkat CN, Gentry LR. Noninvasive Dynamic Magnetic Resonance Angiography With Time-Resolved Imaging of Contrast KineticS (TRICKS) in the Evaluation of Orbital Vascular Lesions. *Arch Ophthalmol* 2007;125(12):1635-1642.

98. Constantinides CD, Atalar E, McVeigh ER. Signal-to-Noise Measurements in Magnitude Images from NMR Phased Arrays. *Magnetic Resonance in Medicine* 1997;38(5):852-857.
99. Roemer PB, Edelstein WA, Hayes CE, Souza SP, Mueller OM. The NMR Phased Array. *Magnetic Resonance in Medicine* 1990;16(2):192-225.
100. Heidemann RM, Griswold MA, Haase A, Jakob PM. VD-AUTO-SMASH Imaging. *Magnetic Resonance in Medicine* 2001;45(6):1066-1074.
101. Deng J, Virmani S, Yang G-Y, Tang R, Woloschak G, Omary RA, Larson AC. Intraprocedural Diffusion-Weighted PROPELLER MRI to Guide Percutaneous Biopsy Needle Placement within Rabbit VX2 Liver Tumors. *Journal of Magnetic Resonance Imaging* 2009;30(2):366-373.
102. Meckel S, Mекle R, Taschner C, Haller S, Scheffler K, Radue E-W, Wetzel S. Time-Resolved 3D Contrast-Enhanced MRA with GRAPPA on a 1.5-T System for Imaging of Craniocervical Vascular Disease: initial experience. *Neuroradiology* 2006;48(5):291-299.
103. Zenge MO, Vogt FM, Brauck K, Jökel M, Barkhausen J, Kannengiesser S, Ladd ME, Quick HH. High-Resolution Continuously Acquired Peripheral MR Angiography Featuring Partial Parallel Imaging GRAPPA. *Magnetic Resonance in Medicine* 2006;56(4):859-865.
104. Candès EJ, Romberg JK, Tao T. Stable Signal Recovery from Incomplete and Inaccurate Measurements. *Communications on Pure and Applied Mathematics* 2006;59(8):1207-1223.

105. Blaimer M, Breuer F, Mueller M, Heidemann RM, Griswold MA, Jakob PM. SMASH, SENSE, PILS, GRAPPA: How to Choose the Optimal Method. *Topics in Magnetic Resonance Imaging* 2004;15(4):223-236.
106. Schueler B. General Overview of Fluoroscopic Imaging. *RadioGraphics* 2000;20:1115–1126.
107. HH Quick HK, G Kaiser, D Hornscheidt, KP Mikolajczyk, S Aker, JF Debatin, ME Ladd. Interventional MRA Using Actively Visualized Catheters, TrueFISP, and Real-Time Image Fusion. *Magnetic Resonance in Medicine* 2003;49:129-137.
108. Feng L, Dumoulin C, Dashnaw S, Darrow R, Guhde R, DeLaPaz R, Bishop P, Pile-Spellman J. Feasibility of Stent Placement in Carotid Arteries with Real-time MR Imaging Guidance in Pigs. *Radiology* 2005;234:558–562.
109. ME Miquel SH, V Muthurangu, BJ Corcoran, SF Keevil, DLG Hill, RS Razavi. Visualization and Tracking of an Inflatable Balloon Catheter Using SSFP in a Flow Phantom and in the Heart and Great Vessels of Patients. *Magnetic Resonance in Medicine* 2004;51:988–995.
110. Guttman M, Raval A, Lederman R, McVeigh E. Real-Time Catheter-Directed MRA With Effective Background Suppression and Persistent Rendering. *Journal of Magnetic Resonance Imaging* 2008;28:538–542.
111. Diethrich E, Ndiaye M, Reid D. Stenting in the Carotid Artery: Initial Experience in 110 patients. *Journal of Endovascular Surgery* 1996;3:42-62.

112. Janke A, Zhao H, Cowin GJ, Galloway GJ, Doddrell DM. Use of Spherical Harmonic Deconvolution Methods to Compensate for Nonlinear Gradient Effects on MRI Images. *Magnetic Resonance in Medicine* 2004;52(1):115-122.
113. Doran S, Charles-Edwards L, Reinsberg S, Leach M. A Complete Distortion Correction for MR Images: gradient warp correction. *Physics in Medicine and Biology* 2005;50(7):1343.
114. Sabati M, Lauzon M, Mahallati H, Frayne R. Interactive Continuously Moving Table (iCMT) Large Field of View Real-Time MRI. *Magnetic Resonance in Medicine* 2006;55:1202-1209.
115. Eddins S. Automated Software Testing for MATLAB. *Computing in Science & Engineering*;PP(99):1-1.
116. Frigo M, Johnson S. FFTw: An Adaptive Software Architecture for the FFT. 1998.
117. Haacke E, Brown R, Thompson M, Venkatesan R. *Magnetic Resonance Imaging: Physical Principles and Sequence Design*: Wiley-Liss; 1999.
118. Glover G, Pelc J; General Electric Company, assignee. Method for Correction Image Distortion due to Gradient Nonuniformity United States. 1986.
119. EM Haacke RB, MR Thompson, R Venkatesan,. *Magnetic Resonance Imaging: Physical Principles and Sequence Design*: Wiley-Liss; 1999.
120. Schmitt M, Potthast A, Sosnovik D, Polimeni J, Wiggins G, Triantafyllou C, Wald L. A 128-Channel Receive-Only Cardiac Coil for Highly Accelerated Cardiac MRI at 3 Tesla. *Magnetic Resonance in Medicine* 2008;59:1431–1439.

121. Hansen C. Rank-Deficient and Discrete Ill-Posed Problems: numerical aspects of linear inversion. Philadelphia: Society of Industrial and Applied Mathematics; 1997.
122. Susil R, Yeung C, Halperin H, Lardo A, Atalar E. Multifunctional Interventional Devices for MRI: A Combined Electrophysiology/MRI Catheter. *Magnetic Resonance in Medicine* 2002;47:594-600.
123. Ayranci C, Carey J. 2D braided composites: A Review for Stiffness Critical Applications. *Composite Structures* 2008(85):43–58.